CELL BIOLOGY

Strength Under Tension

Mechanical tension on a cell from its environment alters the expression of a protein that changes the physical properties of the nucleus.

Russell Bainer[1,2] and Valerie Weaver[1,2,3,4,5,6]

Mechanics control gene expression to modulate tissue-specific differentiation, but the molecular mechanisms that underlie these effects remain unclear. On page 975 of this issue, Swift *et al*. (*1*) link tissue specificity and extracellular matrix stiffness to the relative abundance of the nuclear envelope protein lamin A. The findings support the idea that mechanical links exist between the nucleus and the extracellular microenvironment that direct cell fate, and imply that force mediates these effects by altering the biophysical properties of the nucleus.

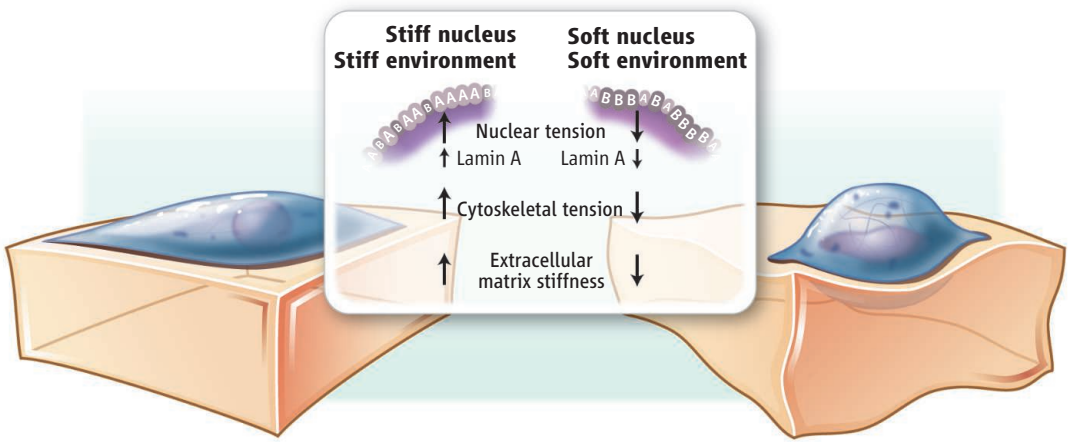

Mechano-response. Tension from the extracellular matrix affects cytoskeletal tension on the nucleus. This affects the turnover of lamin A in the nuclear envelope, expression of *LMNA,* and stiffness of the nucleus.

Mechanical forces are generated at the cell and tissue level through cell-cell and cell–extracellular matrix interactions. Cells sense, translate, and transmit mechanical cues from their periphery to the nucleus and induce changes in gene expression (*2*). This is accomplished in part by receptor-mediated tuning of biochemical and transcriptional circuits. Alternatively, mechanical cues can transmit forces through physical links between the nuclear membrane and the extracellular space. These connections distort the nuclear envelope and evoke transcriptional changes by locally altering the spatial accessibility of chromatin to transcriptional regulators (*3*, *4*). Such changes occur rapidly and proportionately to the extent of the deformation (*5*), but histone deacetylase activity eventually increases after prolonged stress. This modification of histones condenses chromatin, thereby modifying transcription. Swift *et al*. show that the force environment can change transcription of the gene *LMNA* and stability of the encoded protein, lamin A/C, to alter nuclear rheology. This indicates that mechanically driven cell differentiation involves interdependent changes in nuclear composition and transcriptional state.

Cells not only regulate their cytoskeletal organization, cell shape, polarity, and molecular state but also modify the extracellular matrix composition and topology to achieve tensional homeostasis. In this manner, cells can both sense and dictate the physical properties of their microenvironment while preserving the structural continuity within the surrounding tissue. Consequently, tissues

[1]Department of Surgery and Center for Bioengineering and Tissue Regeneration, University of California, San Francisco (UCSF), San Francisco, CA 94143, USA. [2]Stanford University Physical Sciences–Oncology Center, Palo Alto, CA, USA. [3]Department of Anatomy, UCSF, San Francisco, CA 94143, USA. [4]Department of Bioengineering and Therapeutic Sciences, UCSF, San Francisco, CA 94143, USA. [5]Eli and Edythe Broad Center of Regeneration Medicine and Stem Cell Research, UCSF, San Francisco, CA 94143, USA. [6]Helen Diller Family Comprehensive Cancer Center, UCSF, San Francisco, CA 94143, USA. E-mail: valerie.weaver@ucsfmedctr.org

Published by AAAS

acquire stiffness optima as an emergent property of the physical and biochemical interactions between their constituent cells. This tensional equilibrium confers macroscopic compliance properties that are critical for processes such as stem cell differentiation, embryonic development, and tissue homeostasis.

The specific mechanisms by which individual cells physically remodel themselves to functionally drive macroscopic changes in tissue compliance are not well understood, however. In addition to responding dynamically to immediate physical cues, cells must integrate mechanical signals to alter their long-term molecular state and cellular phenotype. Accordingly, such mechanisms must operate on long time scales to promote phenotypic stabilization, likely by directing transcriptional and epigenetic changes.

Swift *et al*. show that the relative abundance of lamin A is a key component of mechanoreciprocal responses and a major determinant of cell and tissue stiffness (see the figure). The authors observed that increased cell tension reduces the turnover of lamin A in the nuclear lamina. This causes accumulation of the mechanosensitive Yes-associated protein (YAP), a master transcriptional regulator. An increase in lamin A also triggers the serum response factor (SRF) signaling pathway, whose gene targets control the actin cytoskeleton. The accumulation of lamin A also drives translocation of the retinoic acid receptor into the nucleus to stimulate transcription of *LMNA* and the production of more lamin A. The findings suggest a mechanism that could explain the strong correlation between relative abundance of lamin A in diverse cell types with macroscopic tissue stiffness. Interestingly, as the relative abundance of lamin A increases, the viscosity of the nucleus also increases. It is possible that in addition to activating mechanosignaling pathways, an increase in lamin A may play a role in physically stiffening the nucleus as part of the cellular response to increased tension.

The model presented by Swift *et al*. proposes how cells that are otherwise acutely sensitive to mechanical signals can structurally acclimate to tissue environments that are pervasively subject to a sizable mechanical load. In such circumstances, lamin A could physically reinforce the nuclear envelope, which would stabilize interactions between chromatin and the nuclear lamina and inure the cell to subsequent nuclear distortions that might otherwise occur in a high-tension tissue environment. Indeed, such an observation could explain why many tumors, which are typically stiffer than the surrounding tissue and are characterized by increased interstitial pressure, also often have greater amounts of lamin A compared to normal cells (*6*, *7*). Moreover, the model hints at a deeper interplay between mechanosensitive signaling pathways, which are apparently affected by both external stress and elevated lamin A abundance, and transcriptional changes that are induced by direct tension on the nucleus from cytoskeletal contacts, which are likely to be modified in cells with lamin A–rich nuclear envelopes. Alternatively, increased tissue-level stiffness might compensate for lamin A–induced changes in nuclear compliance, such that the cytoskeleton simply transmits a greater mechanical load to enable cytoskeletal contact points on the nucleus to remain mechanically sensitive.

The provocative feed-forward mechanism governing lamin A concentration in the model of Swift *et al*. is critically dependent on retinoic acid receptor activity and provides another potential layer of mechanosensitive regulation. For instance, in the absence of ligand, the retinoic acid receptor will heterodimerize with one of the nuclear receptor co-repressor repressor proteins which, together with their associated histone deacetylases, inhibits transcription from specific promoters to maintain heterochromatin. Given the importance of the nuclear lamina in stabilizing heterochromatin, the data presented by Swift *et al*. implicate epigenetic silencing of lamina-associated chromatin as a key component of tension-mediated transcriptional regulation.

Additional studies are required to explicitly link mechano-reciprocal nuclear stiffening to gene-regulatory mechanisms. Elucidating the phenomena that collectively define cellular mechanosensation will also require studies to more completely unify the functionality of direct and indirect force-mediated transcriptional mechanisms. For cells, it seems that tension can become a source of considerable strength.

References

1. J. Swift *et al*., *Science* **341**, 1240104 (2013); 10.1126/science.1240104.
2. C. C. DuFort, M. J. Paszek, V. M. Weaver, *Nat. Rev. Mol. Cell Biol.* **12**, 308 (2011).
3. D. E. Ingber, *J. Cell Sci.* **104**, 613 (1993).
4. A. Mazumder, G. V. Shivashankar, *J. R. Soc. Interface* **7** (suppl. 3), S321 (2010).
5. J. H. -C. Wang, B. P. Thampatty, J. S. Lin, H. J. Im,. *Gene* **391**, 1 (2007).
6. L. Kong *et al*., *Carcinogenesis* **33**, 751 (2012).
7. C. R. Foster *et al*., *Nucleus* **2**, 434 (2011).

10.1126/science.1243643

Published by AAAS

Nuclear Lamin-A Scales with Tissue Stiffness and Enhances Matrix-Directed Differentiation

Joe Swift, Irena L. Ivanovska, Amnon Buxboim, Takamasa Harada, P. C. Dave P. Dingal, Joel Pinter, J. David Pajerowski, Kyle R. Spinler, Jae-Won Shin, Manorama Tewari, Florian Rehfeldt, David W. Speicher, Dennis E. Discher*

READ THE FULL ARTICLE ONLINE
http://dx.doi.org/10.1126/science.1240104

Cite this article as J. Swift *et al.*, *Science* **341**, 1240104 (2013).
DOI: 10.1126/science.1240104

Introduction: Tissues can be soft like brain, bone marrow, and fat, which bear little mechanical stress, or stiff like muscle, cartilage, and bone, which sustain high levels of stress. Systematic relationships between tissue stiffness, protein abundance, and differential gene expression are unclear. Recent studies of stem cells cultured on matrices of different elasticity, *E*, have suggested that differentiation is mechanosensitive, but the molecular mechanisms involved in particular tissues remain elusive.

Methods: We developed quantitative mass spectrometry algorithms to measure protein abundance, stoichiometry, conformation, and interactions within tissues and cells in relation to stiffness of tissues and extracellular matrix. Manipulations of lamin-A levels with small interfering RNA, overexpression, and retinoic acid or antagonist were applied to stem cells cultured on different matrices to assess lamin-A's role in mechanosensitive differentiation. To characterize molecular mechanisms, promoter analyses, transcriptional profiling, and localization of transcription factors were complemented by measurements of nuclear mechanics and by modeling of the core gene circuit.

Results: Proteomic profiling of multiple adult solid tissues showed that widely varied levels of collagens in extracellular matrix and of lamin-A in nuclei followed power-law scaling versus *E*. Scaling for mechanoresponsive lamin-A conformed to predictions from polymer physics, whereas lamin-B's varied weakly. Tumor xenograft studies further demonstrated that matrix determined tissue *E*, whereas lamin-A levels responded to changes in *E*. In tissue culture cells, both lamin-A conformation and expression were mechanosensitive, with phosphorylation and turnover of lamin-A correlating inversely with matrix *E*. Lamin-A knockdown enhanced mesenchymal stem cell differentiation on soft matrix that favored a low-stress, fat phenotype. Lamin-A overexpression or transcriptional induction with a retinoic acid (RA) antagonist enhanced differentiation on stiff matrix toward a high-stress, bone phenotype. Downstream of matrix stiffness, the RA pathway regulated lamin-A transcription, but feedback by lamin-A regulated RA receptor (RARG) translocation into nuclei. High lamin-A levels physically impeded nuclear remodeling under stress but also coregulated other key factors. These factors included both serum response factor (SRF), which promoted expression of stress fiber–associated proteins involved in differentiation, and a Hippo pathway factor (YAP1) involved in growth.

Discussion: The characteristic stress in normal tissue favors collagen accumulation and a characteristic stiffness that cells transduce through nuclear lamin-A to enhance tissue-specific differentiation. Tension-inhibited turnover of rope-like filaments of lamin-A provides sufficient mechanochemical control of a core gene circuit to explain the steady-state scaling of lamin-A with *E*. High lamin-A physically stabilizes the nucleus against stress and thereby stabilizes the nuclear lamina and chromatin, with implications for epigenetic stabilization and limiting of DNA breaks. Moreover, lamin-A levels directly or indirectly regulate many proteins involved in tissue-specific gene expression, and, because lamin-A levels can vary by a factor of 10 or more downstream of tissue mechanics, an important fraction of tissue-specific gene expression depends on tissue mechanics, which changes in development, injury, and many diseases.

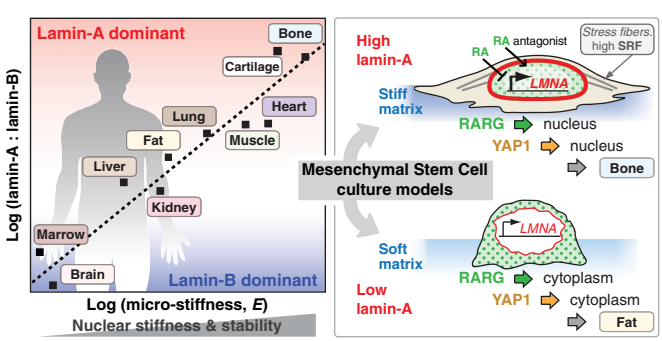

FIGURES IN THE FULL ARTICLE

SUPPLEMENTARY MATERIALS

Materials and Methods
Figs. S1 to S16
Tables S1 to S3
References

RELATED ITEMS IN *SCIENCE*

R. Bainer, V. Weaver, Strength under tension. *Science* **341**, 965–966 (2013). doi:10.1126/science.1243643

Tissue micromechanics correlate with abundance of collagens and nuclear lamins, which influence cell differentiation. (Left) Collagen and lamin-A levels scale with *E*, consistent with matching tissue stress to nuclear mechanics. **(Right)** Matrix stiffness in tissue culture increases cell tension and stabilizes lamin-A, regulating its own transcription and that of stress fiber genes, enhancing differentiation. RA, retinoic acid, i.e., vitamin A; RARG, YAP1, and SRF, transcription factors.

The list of author affiliations is available in the full article online.
*Corresponding author. E-mail: discher@seas.upenn.edu

Nuclear Lamin-A Scales with Tissue Stiffness and Enhances Matrix-Directed Differentiation

Joe Swift,[1]* Irena L. Ivanovska,[1]* Amnon Buxboim,[1] Takamasa Harada,[1] P. C. Dave P. Dingal,[1] Joel Pinter,[1] J. David Pajerowski,[1] Kyle R. Spinler,[1] Jae-Won Shin,[1] Manorama Tewari,[1] Florian Rehfeldt,[1] David W. Speicher,[2] Dennis E. Discher[1,2]†

Tissues can be soft like fat, which bears little stress, or stiff like bone, which sustains high stress, but whether there is a systematic relationship between tissue mechanics and differentiation is unknown. Here, proteomics analyses revealed that levels of the nucleoskeletal protein lamin-A scaled with tissue elasticity, *E*, as did levels of collagens in the extracellular matrix that determine *E*. Stem cell differentiation into fat on soft matrix was enhanced by low lamin-A levels, whereas differentiation into bone on stiff matrix was enhanced by high lamin-A levels. Matrix stiffness directly influenced lamin-A protein levels, and, although lamin-A transcription was regulated by the vitamin A/retinoic acid (RA) pathway with broad roles in development, nuclear entry of RA receptors was modulated by lamin-A protein. Tissue stiffness and stress thus increase lamin-A levels, which stabilize the nucleus while also contributing to lineage determination.

Stiffness and strength of a tissue should in principle relate to the physical stress in that tissue. Low stresses in brain and fat may explain why these tissues are soft. High stresses on adult bone, in contrast, are thought to promote its growth and stiffening through a "mechanostat" that functions to match the stress (*1*). At a microscale, physical stress deforms cells (*2*) and can alter gene expression profiles (*3*), but cells in vivo might also directly sense the local tissue stiffness or microelasticity *E* (in kilopascals, kPa) (table S1), which should relate to the typical stress in that tissue (also in kPa). It is unclear, however, whether any specific proteins function across diverse tissues to not only match stiffness with stress but also impact differentiation processes.

When animal cells are cultured on various gels or elastomeric substrates, cell-generated stress or tension increases as cells spread on matrices with increasing elasticity, *E* (*4*, *5*). Surprising effects on differentiation (*5*), as well as cell shape and motility (*6*), have also been observed. Although some studies have suggested a lack of response to matrix elasticity in two-dimensional (2D) (*7*) or 3D cultures (*8*), several other studies have found that gels that mimic the compliance of brain or fat, respectively, maximize neurogenesis or adipogenesis (*9*–*11*). Gels that are moderately stiff like muscle are best for myogenesis (*12*–*14*), and gels that are firm like precalcified bone optimize osteogenesis in 2D and 3D (*5*, *15*, *16*). A 3D hierarchy of soft/stiff/rigid tissue might exist, but the presence of any molecular mechanostats that relate to tissue stiffness and that systematically affect lineage remain unknown. Widely expressed transcriptional regulators that include YAP1 of the Hippo pathway, which promotes growth and regeneration (*17*), as well as components of the serum response factor (SRF) pathway, which promote cytoskeletal gene expression in differentiation (*18*), exhibit low nuclear activity in cells on substrates designed to limit cell spreading and cytoskeleton tensions (*11*, *19*). How such factors or completely distinct pathways might relate to matrix elasticity and the stiffness of 3D tissues has yet to be addressed.

Forces on a tissue, as well as those generated by cells within a tissue (Fig. 1A), are sustained in rough proportion to microelasticity *E* by collagens and lineage-specific cytoskeletal proteins (*4*, *5*). Some forces might also propagate into the nucleus and be resisted by the nuclear lamina. Lamins are intermediate filament proteins found in nearly all cell nuclei and contribute to nuclear stiffness (*20*, *21*) and nuclear stability (*22*). Although lamins might be viewed as similar in mechanical function to keratin intermediate filament proteins that determine nail and skin structure (*23*), lamins are also believed to modulate transcription (*24*) and have been speculated to mechanoregulate the genome (*25*, *26*). Here, initial analyses of proteomes from soft and stiff tissues motivated us to examine, both in vivo and in cultures on soft and stiff gels, whether the nuclear lamina is involved in sensing tissue elasticity in differentiation.

Results

Lamin-A and Collagen Levels Scale with Tissue Microelasticity

Allometric scaling laws for stress response would be understandable for polymer-based molecular mechanostats, so we examined proteomes for such trends across tissues from brain to bone (Fig. 1A). Nearly 100 of the most abundant structural and nuclear proteins were quantified relative to invariant proteins using label-free mass spectrometry (MS) (Fig. 1B and figs. S1 and S2). Lamin-A was found to increase systematically 30-fold from soft to stiff tissue (Fig. 1D and fig. S3). Lamin-B1 differed by less than threefold, and lamin-B2 varied even less (Fig. 1F), consistent with B-type lamins being constitutively expressed (*27*). An absolute stoichiometry of the lamin isoforms (lamin-A:B) was directly determined by MS quantitation of a peptide common to all lamins (see Materials and Methods) (fig. S4, A and B) as validated with recombinant protein (fig. S4C), and a power law fit versus tissue microelasticity gave Lamin-A:B ~ $E^{0.6}$ (R^2 = 0.88). Combined with findings that B-type lamins were roughly similar in abundance (fig. S4D), the weak scaling of both B-type lamins is consistent with the key result for Lamin-A versus *E* as a metric of tissue stress: Lamin-A ~ $E^{0.7}$.

Primary and immortalized cell types derived from a range of human and mouse tissues follow this scaling in terms of *E* of the tissue of origin, which helps to generalize the result across species and perhaps ameliorate concerns over tissue heterogeneity. Immunoblotting also validated the A:B scaling and further suggested that the A and C splice-form products of the *LMNA* gene follow respective scaling exponents of 1.0 and 0.5, so that the 0.7 exponent for total lamin-A is a geometric mean (Fig. 1E and fig. S5). A power law between concentration of a polymer and its stiffness is typical in the physics of biopolymers (*28*–*30*). We had previously knocked down lamin-A in human lung–derived A549 cells without affecting lamin-B, and micropipette aspiration showed that knockdown nuclei are softer (*20*), suggesting that nuclear stiffness increases with A:B stoichiometry. Although the tissue *E* here provides a metric of the typical stress on a tissue, the power law exponent for lamin-A is midway between the linear response of a simple polymer network (*31*) and that of a nonlinear, semiflexible meshwork typified by stiffness versus concentration of actin [with exponent 0.4 (*29*)].

The A:B stoichiometry in Fig. 1D (*y* axis) indicates that lamin-A dominates over a range of stiff tissues, consistent with *LMNA* mutations causing lipodystrophies, muscular dystrophies, and premature aging (progeria) that affects heart and large vessels while sparing soft tissues such as brain and marrow (*32*). Lamin-B dominates in soft tissues, consistent not only with lamin-A appearing low in antibody-staining of neuroendocrine tissues and hematopoietic cells (*27*) [despite epitope masking (*33*)] but also with lamin-B knockout mice dying at birth with defects in brain development and tissue innervation (*34*). In other words, the normal function of cells in stiff tissues is most dependent on lamin-A.

In nuclear-enriched fractions as well as whole tissue lysates, extracellular matrix proteins were the other detected tissue proteins that scaled

[1]Molecular and Cell Biophysics Laboratory, University of Pennsylvania, Philadelphia, PA 19104, USA. [2]The Center for Systems and Computational Biology, Wistar Institute, Philadelphia, PA 19104, USA.

*These authors contributed equally to this work.
†Corresponding author. E-mail: discher@seas.upenn.edu

with E and also showed transcripts scaling with E in both man and mouse (fig. S2). Collagen-1 is the most abundant protein in animals, and its two fiber-coassembling isoforms both gave collagen-1 ~ $E^{1.5}$ (Fig. 1G). Gels made with purified collagen-1 scale as ~ $E^{0.5}$ (35), but a different exponent for tissue seems consistent with additional matrix or cell components contributing to tissue mechanics. Indeed, collagen-3, -5, -6, -11,

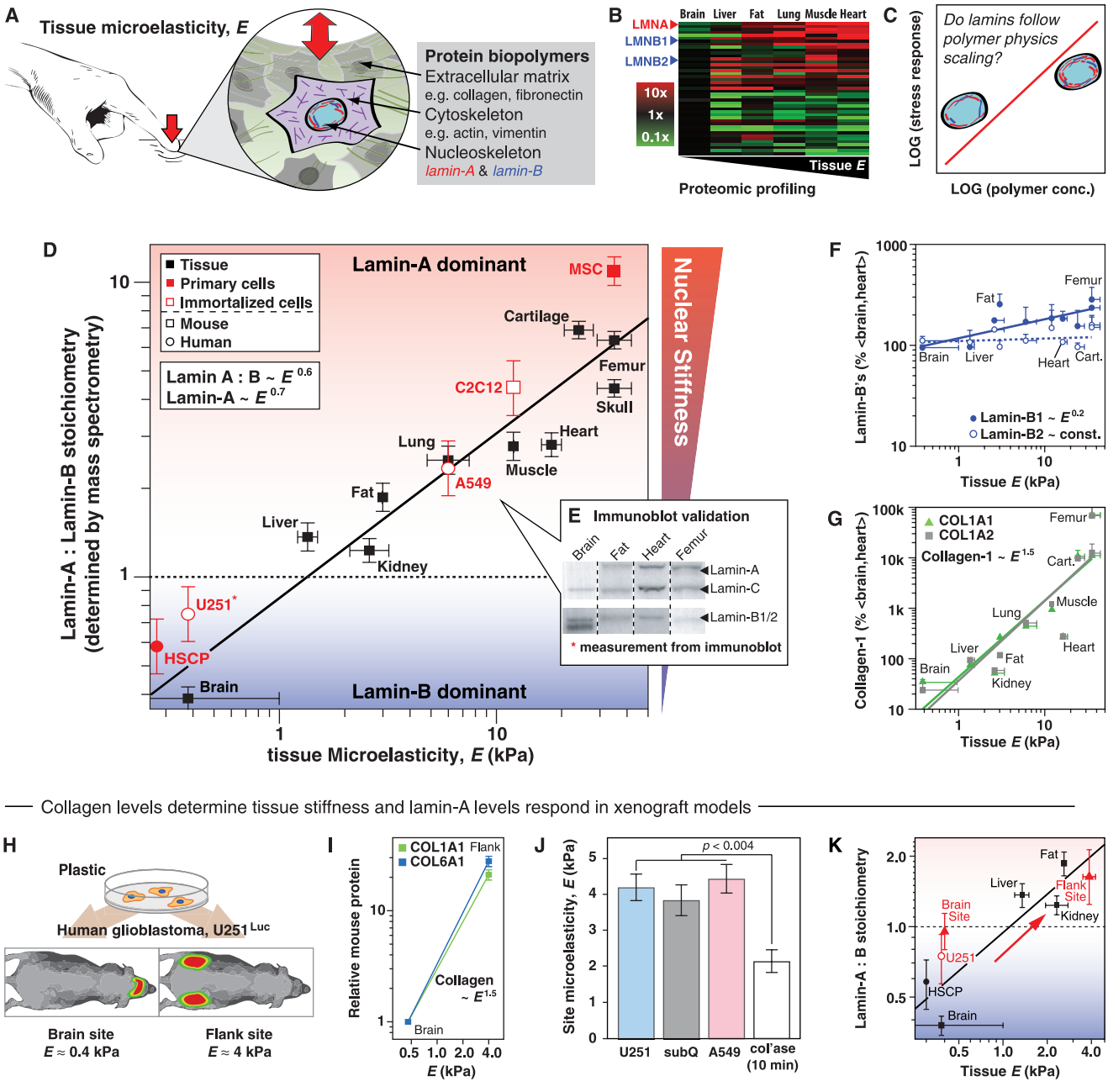

Fig. 1. Lamin-A and collagen levels scale with tissue stiffness, but collagen determines stiffness while lamin-A responds. (**A**) Tissue deformation under force is quantified by E and transfers stresses through the extracellular matrix and the cytoskeleton into the nucleus. (**B** and **C**) The proteomes of adult mouse tissues were profiled to determine whether scaling of mechanical properties with biopolymer concentration exists across tissues. (**D**) Quantitative proteomics of multiple human and mouse tissues and cells revealed scaling with E of the absolute ratio or stoichiometry of lamin-A to lamin-B through MS quantification of a pan-lamin peptide. Differences in ratios are significant with brain ≪ liver < fat < heart, lung, and muscle ≪ skull ≪ femur and cartilage, where < indicates $P \leq 0.05$ and ≪ indicates $P \leq 0.01$. Nuclei with abundant lamin-A are stiff (20). Cultured cells showed the same trend as their primary source tissue. HSCP, human hematopoietic stem cell progenitors from marrow; U251, human glioblastoma cells from brain; A549, human adenocarcinoma epithelial cells from lung; C2C12, mouse myoblast cells from muscle; MSC, osteo-prone human mesenchymal stem cells from marrow. (**E**) MS trends were validated by immunoblotting (representative blots taken from fig. S5A). (**F**) Lamin-B1 scales very weakly with E, whereas lamin-B2 is constant on average. (**G**) Collagen-1 isoforms scale strongly with E. (**H**) Human glioblastoma cells U251^{Luc} (expressing luciferase for imaging) were xenografted into mouse brain and flank, and 4-week-old tumors were profiled by MS proteomics. (**I**) Mouse-derived collagens in U251 grown in mouse brain and flank scale with E as observed for adult mouse tissues. (**J**) Stiffness of flank tumors made with high (A549) or low (U251) lamin-A:B cells was similar to the stiffness of the subcutaneous site (subQ). Tumors were 50% softer after only a brief treatment with collagenase (col'ase). (**K**) Lamin composition and stiffness of the tumors fit adult tissue scaling. All points are significantly different where indicated ($n \geq 3$ MS measurements).

and -12 also scaled as ~ $E^{0.9\text{-}1.5}$. Our tissue profiling was unable to identify any compelling cytoskeletal candidate [particularly in the SRF or YAP1 pathways (fig. S1, A to C)] that could be a universal "mechanostat" similar to lamin-A for the nucleus. A possible reason is tissue-specific isoform usage, such as with the intermediate filament protein vimentin, which is restricted to specific lineages rather than being expressed in all cell types. Similar specialization seems likely to apply to isoforms of actin, myosin, and microtubules.

Matrix Determines Tissue Stiffness and Lamin-A Adjusts in Vivo

To address the relative affect of extracellular matrix and lamins on tissue stiffness, human-derived U251 glioblastoma tumors were grown in the brain and in subcutaneous flank sites of nude mice for label-free MS proteomics (Fig. 1H and fig. S6, A to C). In standard culture, these cells had a low A:B ratio similar to normal mouse brain (Fig. 1D). However, flank tumors of U251s had more matrix and were much stiffer than brain tumors, with scaling of collagen density versus E appearing typical of normal adult tissue (Fig. 1I). Flank tumors of human-derived A549 lung cells (A:B ≈ 2.3) had similar E as U251 tumors and were only slightly stiffer than normal subcutaneous tissue, revealing a response independent of initial lamin levels (Fig. 1J and fig. S6D). Collagenase treatment of fresh tumors reduced E by > 50% in just 10 min, suggesting that collagen is a key determinant of tissue stiffness, unlike lamin-A. Consistent with this interpretation, human matrix or matrix-associated proteins were among the few proteins more than twofold higher in the flank compared with the soft brain site. Moreover, human lamin-A levels proved higher in flank versus brain sites (fig. S6), whereas lamin-B1 and lamin-B2 were only slightly higher in brain. U251 cells thus adjust their lamin-A:B ratio by 1.5-fold, which fits remarkably well to the stiffness-dependent scaling of lamin-A:B found in normal tissues (Fig. 1K).

Two other intermediate filament (IF) proteins exhibited site-dependent differences in U251 cells that were notably similar to lamin-A. Human glial fibrillary acidic protein (GFAP) and vimentin were both lower in the softer brain than in the flank (fig. S6B). GFAP expression is known to be restricted to cells of the central nervous system plus a few nonepithelial lineages, so its up-regulation in flank by human brain–derived U251 cells was not expected. Indeed, mouse GFAP was almost undetectable in flank but abundant in brain (fig. S6C). On the other hand, human nestin (yet another IF protein) in the grafted U251 cells was slightly higher in brain than flank, similar in response to the human B-type lamins. These additional findings for lineage-restricted, cytoplasmic IFs thus reinforced the finding that different IFs exhibit different sensitivities to different microenvironments.

Lamin-A Conformation and Abundance Are Mechanosensitive in Cultured Cells

To understand how lamins sustain stress, we focused on cultures of human-derived U251s, A549s, and low-passage mesenchymal stem cells (MSCs), which collectively span the broad range in lamin-A:B (Fig. 1D). Imaging of lamins under constant immunostaining conditions showed the expected increase in lamin-A intensity as well as juxtaposed networks (*24*) of lamins (Fig. 2, A and B). To dissect molecular responses of lamins to physical stress, we applied cysteine-shotgun MS (CS-MS) which involves using a fluorescent dye to covalently tag cysteines that are conformationally cryptic but exposed by stress (*36*). When nuclei were isolated from cells and subjected to controlled shear (Fig. 2C), stability against nuclear rupture was seen to increase with lamin-A levels: U251 < A549 < [A549 overexpressing green fluorescent protein (GFP)–lamin-A] (Fig. 2D). Peeling of lamin-A off of stressed nuclei as seen by immunofluorescence demonstrated the responsiveness of lamin-A to stress. CS-MS revealed several nuclear proteins in the 60 to 80 kD range as susceptible to stress (fig. S7), with Cys^{522} in lamin-A's immunoglobulin (Ig) domain identified as a stress-sensitive site (Fig. 2E). Studies of pure recombinant Ig domain showed the labeling kinetics of Cys^{522} captured domain unfolding in thermal and solvent denaturation (Fig. 2F and fig. S8, A to E), and this same site in nuclear lamin-A showed 70% more labeling as shear was increased. A nearby Cys^{591} in the tail was also labeled but was insensitive to stress.

A lamin-A point mutation R453W in the Ig domain that causes muscular dystrophy (*37*) and that destabilized the purified domain (Fig. 2F) also produced dysmorphic nuclei in A549 cells expressing a GFP-lamin-A with the mutation (Fig. 2G). After labeling the adherent cells with the Cys-reactive fluorescent dye, lamin-A was enriched by immunoprecipitation and analyzed by MS (IP-MS). Labeling of the Ig's Cys^{522} increased significantly (Fig. 2H), whereas labeling of the tail's Cys^{591} was unaltered. The mutant also showed fivefold less phosphorylation at a proximal Ser^{390} without differences at head or tail phospho-Ser (Fig. 2I and fig. S8, F and G); synthetic peptides and phosphopeptides were made and confirmed the linearity of quantitation by MS (fig. S8F). Lamin-A phosphorylation is known to promote disassembly (*38*) and also protein turnover (*39*).

Stresses in the cell are transmitted to the nucleus and lamina through various interactions, and because cytoskeletal tension increases with matrix stiffness (*5*), CS-MS was used to assess matrix effects on lamin-A. MSCs cultured on either soft gels (0.3 kPa) or stiff gels (40 kPa) exhibited the expected low- and high-tension phenotypes with stiffness-induced increases in (i) cell and nuclear spreading (Fig. 3A and fig. S9A), (ii) stress fiber assembly (Fig. 3A and fig. S9, B and C), and (iii) levels of α-smooth muscle actin (Fig. 3, B and C). On soft matrix, the nuclear envelope appeared highly wrinkled (Fig. 3D), but stiff matrix and high tension "smoothed out" nuclear wrinkles and flattened the nucleus. CS-MS was applied to 3-day cultures, with an anticipation of more labeling of the stress-sensitive Ig domain in the high-tension state, but Cys labeling proved similar in both the Ig and tail sites in cells on soft versus stiff gels (Fig. 3, E and F). On the other hand, phosphorylation proved significantly higher in cells on soft matrices at all four MS-detectable sites (Fig. 3, G and H, and fig. S9D). Because lamin-A phosphorylation promotes disassembly (*38*) and turnover (*39*), the results suggested an inverse relationship between phosphorylation and matrix stiffness. Indeed, the total amount of lamin-A increased significantly in both MSCs and A549 cells on stiff substrates (Fig. 3, I and J, and fig. S9, E to G). Lamin-A's increased levels could thus compensate in part for the increased force per molecule in cells on stiff substrates, and this increased level would tend to maintain stability of the protein and its folded domains. Consistent with an increase in IF assembly with cell tension, MSCs treated with a myosin-II inhibitor to inhibit cell tension have also been found to depolymerize vimentin filaments (*36*). However, because lamin-B did not change significantly with matrix stiffness (fig. S9G) and no lamin-B phosphopeptides were detected, additional study of this mechanism for lamin-A and other mechanosensitive IFs is needed.

Lamin-A Enhances Matrix Elasticity-Directed Differentiation

Matrix elasticity directs lineage specification of human bone marrow–derived MSCs in culture toward bone, fat, or other tissue types with mechanisms based in part on myosin-II generated stresses (*5*). Because lipodystrophy is one of the many diseases involving *LMNA* and because adipocytes are common in human marrow, the softness of fat was mimicked with a soft gel (E = 0.3 kPa), and precalcified bone or "osteoid" was mimicked with a stiff gel (E = 40 kPa). Bone marrow–derived MSCs typically have a very high A:B ratio (Fig. 1D) that probably reflects their osteogenic niche origins (*40*), and indeed even with standard adipogenic media only a very small percentage of MSCs on stiff matrix (~1%) (Fig. 4A) showed after 2 weeks of culture the oil-red–positive lipid droplets that are phenotypic of fat. In these cells, stress fibers were displaced by oil droplets that sometimes deformed the nuclear envelope (Fig. 4B and fig. S10A). Soft matrix increased adipogenesis to 8%, but this increased to nearly 20% with partial knockdown of LMNA. MS profiling also revealed an abundant fatty acid ligase (ACSL1) up-regulated nearly 100-fold with knockdown (fig. S11A). Knockdown did not affect adipogenesis of cells on stiff matrix, which invariably showed about 20-fold fewer adipogenic cells than knockdown cells on soft matrix.

Osteogenesis of MSCs was modulated over a 20-fold range through a combination of matrix elasticity and controlled expression of lamin-A (Fig. 4, C and D). Soft matrix always repressed osteogenesis, but stiff matrix plus lamin-A overexpression led to 80% of cells being positive for a standard marker of osteogenesis. Optimal osteogenic conditions also increased endogenous lamin-A expression (by twofold), whereas adipogenic

conditions slightly suppressed lamin-A (Fig. 4E). Thus, insoluble and soluble factors combined to promote lamina remodeling consistent in trend with soft and stiff tissue lineages (Fig. 1D). Although traditional cultures of MSCs on rigid plastic or glass (with unknown matrix) also showed that lamin-A knockdown favored adipogenesis (*41*) and that lamin-A overexpression favored osteogenesis (*42*), cultures here on controlled matrix suggest that matrix is upstream, consistent with tissue studies (Fig. 1, H to J).

Matrix elasticity–directed lineage specification of MSCs is based in part on myosin-II–generated cell tension and the accompanying cell spreading (*5*, *11*), which roughly paralleled nuclear shape changes (Figs. 3A and 4E, and fig. S9, A and B). Myosin-IIA was indeed increasingly active and assembled with stiffness-dependent decreases in phosphorylation near myosin-IIA's coiled-coil tail (fig. S9C), as we reported recently (*43*). Thus, phosphorylation of Ser/Thr residues just beyond the coiled coils (e.g., Fig. 3H) inhibits assembly of both myosin-IIA and lamin-A homodimers into the respective functional higher-order filaments, and such phosphorylation appeared consistently higher in cells on soft matrices compared with stiff matrices for both proteins. On the other hand, overexpression of lamin-A in cells on stiff matrix did not increase tail phosphorylation of myosin-IIA, suggesting a nonlinear relationship between cytoskeleton tension and lamin-A at the highest levels.

Additional indicators of cell tension tended to increase in vitro with matrix elasticity and/or

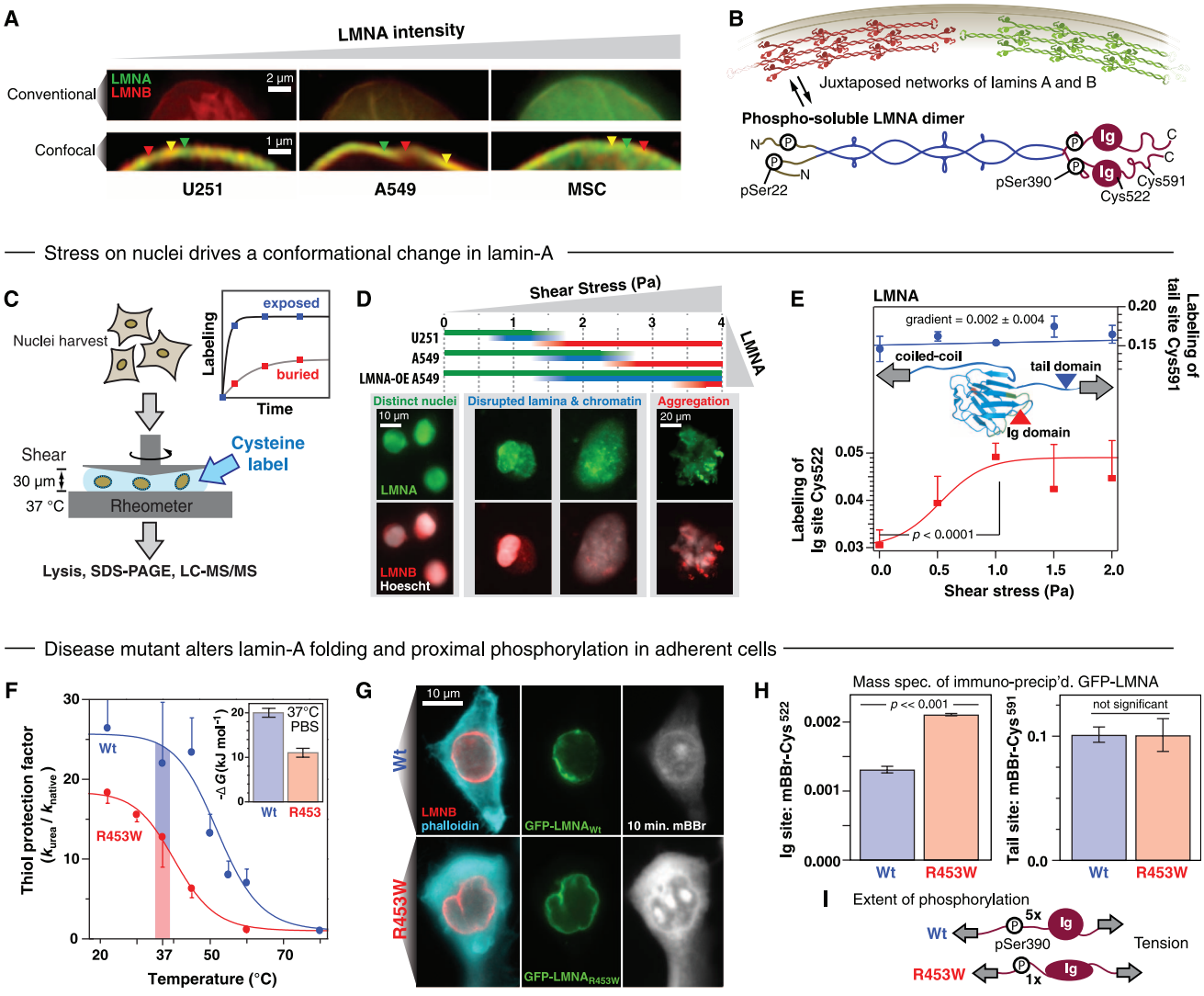

Fig. 2. Nuclear stability is conferred by lamin-A, which unfolds under stress and couples to phosphorylation. (**A**) High-resolution images of the nuclear envelope of U251s, A549s, and MSCs show juxtaposed regions of lamins A (green) and B (red), consistent with earlier observations in HeLa cells (*24*). Triangles highlight domains of lamins A (green), B (red), and overlap (yellow). (**B**) Higher-order assembly of lamin typical of intermediate filament proteins and the lamin-A dimer solubilized by phosphorylation (*38*), annotated with MS-detectable phosphorylation and cysteine sites. (**C**) Shearing of nuclei showed that lamin conformation responds to mechanical stress. A cysteine-reactive label [monobromobimane (mBBr)] was added to nuclei and sheared for 40 min at the indicated stresses in a cone and plate rheometer. All protein was then solubilized and the extent of reaction at each detected cysteine quantified by MS, scaled by the unlabeled protein. (**D**) A549 nuclei imaged following shear stress. Greater lamin expression confers mechanical robustness to the nuclei, limiting disruption of chromatin. (**E**) The Ig-like domain of lamin-A has a cryptic cysteine, Cys^{522}, that is buried in the crystal structure (Protein Data Bank accession number 1IFR) but showed 70% more labeling in stressed A549 nuclei. Labeling of Cys^{591} in the tail of lamin-A did not change with stress (mean ± SEM from curve fit; $P \leq 0.05$, $n \geq 3$ MS measurements). (**F**) A point mutant R453W within the lamin Ig domain that is known to cause muscular dystrophy showed decreased domain stability at 37°C as measured by cysteine labeling rates and tryptophan fluorescence (inset). (**G**) Images of adherent A549 cells transfected with wild-type or mutant GFP-tagged lamin were labeled with 400 μM mBBr for 10 min. (**H**) Labeling of wild-type and R453W lamin of mBBr measured by MS after immunoprecipitation of GFP (IP-MS) showed greater in vivo labeling of mutant in adherent cells; the tail domain showed no significant difference. (**I**) In contrast, phosphorylation at Ser^{390} was fivefold higher in wildtype lamin-A. All points are significantly different, as indicated ($n \geq 3$ MS measurements).

lamin-A levels in MSCs. Not only was α-smooth muscle actin suppressed on soft matrix where lamin-A was low (Fig. 3, B and C), but knockdown of lamin-A also suppressed α-smooth muscle actin (*ACTA2*) transcript and protein (Fig. 4, F and G and fig. S12, A and B), together with many other key targets and components of the SRF pathway that regulates expression of *ACTA2* as well as many cytoskeletal genes (*18*) involved in differentiation to both soft and stiff tissue lineages [neurogenesis (*44*), myogenesis (*18*), and osteogenesis (*45*)]. SRF is regulated in part by nuclear actin (*18*, *46*), and lamin-A binds nuclear actin (*47*) as well as other proteins that also bind nuclear actin (*48*); this provided a mechanism for SRF regulation by lamin-A, as also suggested by overexpression studies of one protein (emerin) that binds both lamin-A and actin (*49*). Tissue analyses showed that SRF target proteins did not generally scale with tissue *E* (figs. S2B and S3D) and that *SRF* and *ACTA2* transcripts increased nontrivially with *E* (fig. S2C). Because high SRF activity can inhibit differentiation of some lineages [e.g., epithelial cells (*11*)], mechanosensitive lamin-A is likely just one coregulator of the SRF pathway.

One transcription factor implicated in lipodystrophy, SREBP1 (*SREBF1*), is known to bind lamin-A in distributing between nucleus and cytoplasm (*50*). SREBP1 is not only an early response factor in adipogenesis (*51*) but, according to chromatin-IP (fig. S12C), it also regulates *ACSL1* and another adipogenic survival factor *FABP5* (*52*), both of which increased with LMNA knockdown (Fig. 4F).

YAP1 has been reported to be excluded from the nucleus in a functionally important manner during adipogenesis of MSCs and also functionally localized to the nucleus during osteogenesis of MSCs (*11*), but neither *YAP1* transcript levels nor its binding partners or target genes changed with lamin-A knockdown (Fig. 4F). Although YAP1 protein levels did decrease with lamin-A knockdown (fig. S12, A and B), and YAP1 did tend to translocate as expected into the nucleus with increased matrix *E* (Fig. 4, H to J, and fig. S12D), lamin-A overexpression in cells on stiff matrix also produced decreases in both total YAP1 levels and nuclear localization (Fig. 4H). Fluorescence intensity profiles through the nucleus further showed many of the overexpressing cells as well as a fraction of wild-type cells on stiff matrix with YAP1 enriched at the nuclear envelope. The nonmonotonic response of YAP1 versus lamin-A levels in vitro was also found for YAP1 protein and transcript levels versus tissue stiffness (Fig. 4K and fig. S12E). Consistent with this, neither YAP1 nor SRF were predicted to directly drive *LMNA* expression (fig. S13A), and *LMNA* has not been found to be a direct target of these factors as detected by chromatin-IP (*18*, *53*). We thus sought a pathway that could directly regulate *LMNA* and thereby impact lineage.

Retinoic Acid Pathway Regulates Lamin-A Transcription, but Lamin-A Protein Regulates an RA Receptor

LMNA level is transcriptionally regulated, with both message and protein fitting the same power law scaling in mouse and man ($R^2 = 0.95$) (Fig. 5A). Promoter methylation was minimal in *LMNA* across a range of cell types (fig. S13B). Bioinformatics analyses of promoters for *LMNA*, *LMNB1*, and *LMNB2* predict retinoic acid (RA) transcription factor sites only in *LMNA* (Fig. 5B and fig. S14), and chromatin-IP has confirmed binding of RA nuclear receptors to *LMNA* (fig. S12C) consistent with experiments on RA-responsive elements (RARE) in *LMNA* (*54*). Neither RA factors nor collagens were greatly affected by lamin-A knockdown (Fig. 4F and fig. S13C), except for RARB, which is a downstream target of the RA pathway. This placed extracellular matrix upstream of lamin-A together with the level of transcription factors that likely regulate lamin-A, while also suggesting that the RA pathway might be modulated by lamin-A.

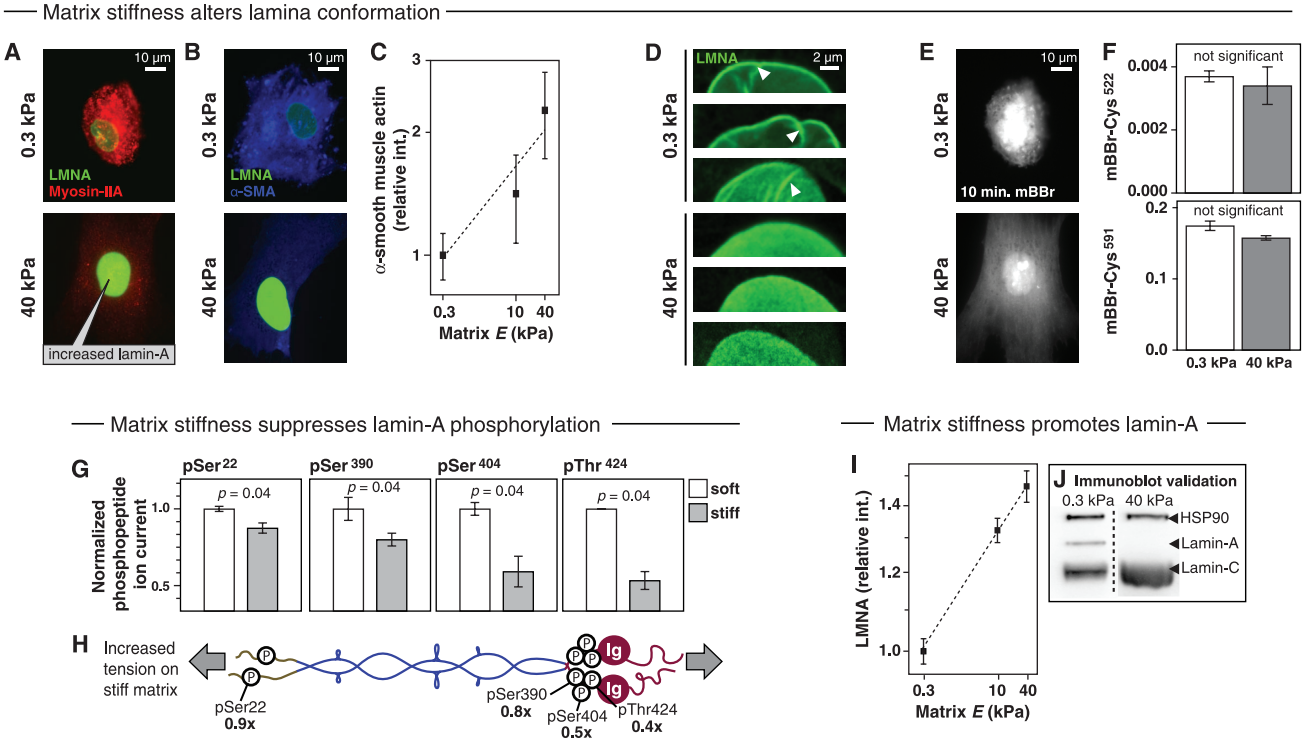

Fig. 3. Cell and nuclei spread on stiff matrix, suppressing lamin-A phosphorylation and increasing lamin-A and cell tension. Response of MSCs to substrate stiffness was characterized. (**A**) Cells are more rounded on soft (0.3 kPa) matrix, whereas on stiff (40 kPa) matrix they spread with more pronounced stress fibers, consistent with higher cell tension. (**B** and **C**) Levels of α-smooth muscle actin were higher on stiff matrix. (**D**) Confocal microscopy showed wrinkled nuclei on soft matrix, and smoothed-out and flattened nuclei on stiff matrix. Images are of the middle *z*-section of different nuclei. (**E** and **F**) Cell and nuclei rapidly label with mBBr, but quantitation of lamin-A labeling by IP-MS showed no significant difference in labeling of either the Ig domain or tail sites on soft versus stiff substrate. (**G** and **H**) Phosphorylation at Ser^{390} is ~30% higher on soft substrate, predictive of solubilization. (**I** and **J**) Quantitative immunofluorescence and immunoblot show lamin-A increased with substrate stiffness. This tends to reduce the mechanical stress per molecule and maintain the Ig fold. Blots were taken from the same membrane. All points are significantly different ($P \leq 0.05$; $n \geq 3$ MS and IF measurements).

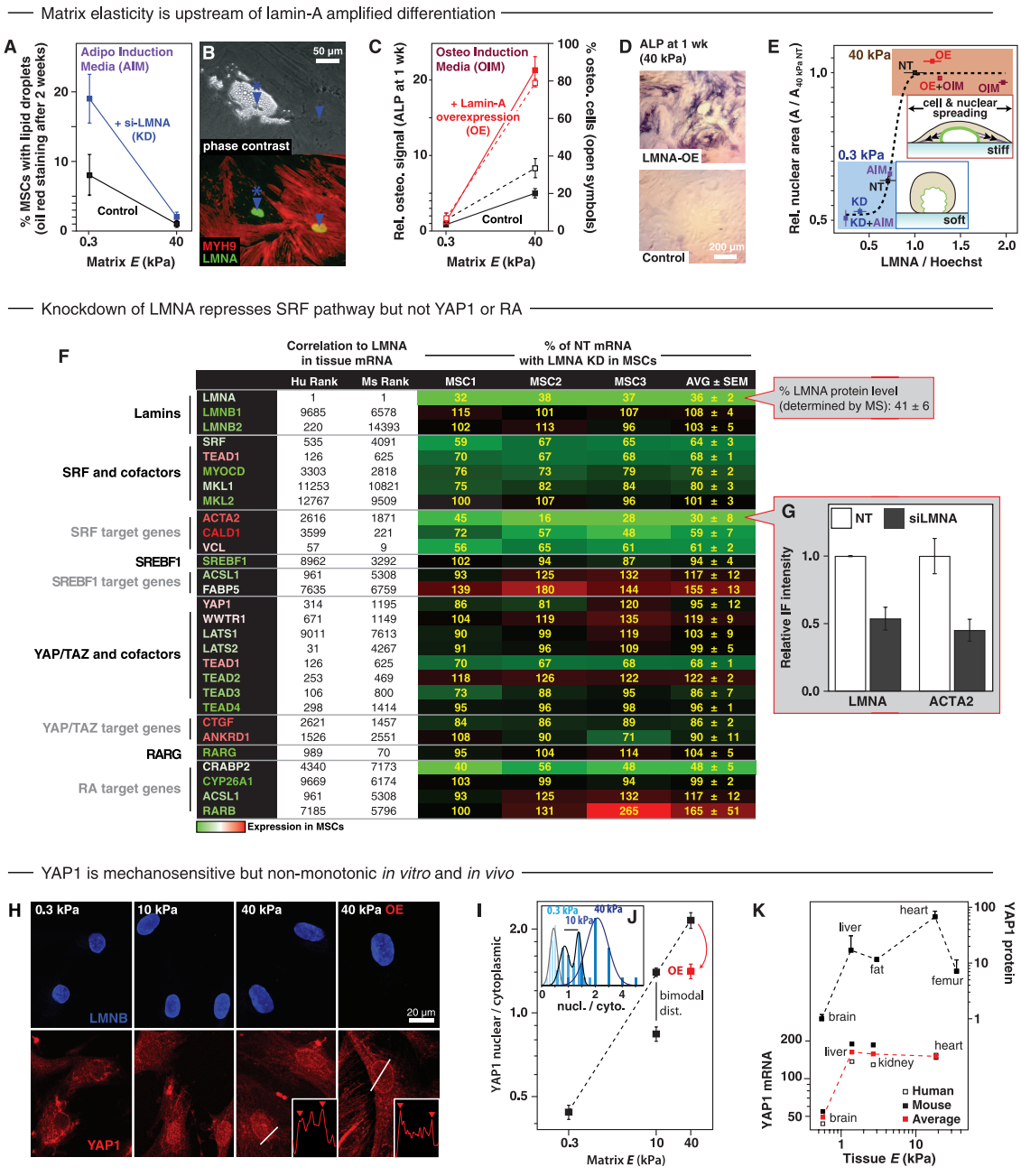

Fig. 4. Matrix elasticity directs stem cell differentiation, which is enhanced by lamin-A as it regulates SRF and YAP1. (**A**) Partial knockdown (KD) of lamin-A in MSCs with si-LMNA in combination with soft matrix (0.3 kPa) and an adipo-inducing media–maximized adipogenesis ($P \leq 0.02$ knockdown versus control). Stiff matrix (40 kPa) suppressed adipogenesis in parallel cultures, with no significant effect of knockdown. Knockdown of lamin-A was to 35% of wild-type or scrambled-siRNA. (**B**) Adipogenesis in MSCs on plastic showed that cells with oil droplets (phase contrast microscopy; nucleus indicated by blue arrow with asterisk) had minimal stress fibers (myosin-IIa immunofluorescence) compared with cells without oil droplets (nucleus indicated by blue arrow without asterisk). (**C**) Overexpression (OE) of lamin-A in MSCs in combination with stiff matrix and an osteo-inducing media–maximized osteogenesis ($P \leq 0.0001$). Soft matrix suppressed osteogenesis in parallel cultures, with no significant effect of overexpression. (**D**) Alkaline phosphatase (ALP) staining was done after 1 week as a measure of osteogenic signal, together with the fraction of cells with staining. (**E**) Correlation between nuclear area and lamin-A level with treatments on soft and stiff matrix (normalized to Hoechst stain). NT, non-treated control. Inset cartoons highlight the relationship between cell and nuclear spread area as well as cell tension. (**F**) Pathway analyses after knockdown of *LMNA* in three different MSCs. Gene symbols are colored according to mRNA abundance in MSCs (green, low; red, high) from microarray data for 11 soft tissues in human and 10 soft tissues in adult mouse (of 14,985 gene annotations common to mouse and human), and genes are ranked based on Pearson correlations with lamin-A. SRF and related transcription factors and target genes all show reduced levels with lamin-A knockdown, whereas neither *YAP1* nor its target genes were affected. TEAD1 has been implicated in both YAP1 and SRF pathways, but lamin-A knockdown suppresses *TEAD1* similar to *SRF*, suggesting that it is in the SRF pathway. A transcription factor predicted to regulate lamin-A (*RARG*) was not affected by lamin-A knockdown, and few RA pathway transcripts changed with *LMNA* knockdown except *CRABP2* (*89*), which decreased. *CRABP2* is upregulated in osteoarthritis models where COL1A1 increases in osteogenic-like processes (*90*). The SREBF1-regulated gene, *FABP5*, increases to give an average ratio for message of *CRABP2*/*FABP5* ~ 0.3 relative to untreated cells; both CRABP2 and FABP5 are known to bind RA, and the change in the RA signaling ratio (*CRABP2*/*FABP5*) was consistent with switching of differentiation pathways (*91*). (**G**) The decrease in *ACTA2*, downstream of SRF, was confirmed at the protein level in MSCs by immunofluorescence. (**H**) High-resolution confocal microscopy of YAP1 in MSCs cultured on substrates of increasing stiffness show increasing nuclear localization, as reported previously (*11*). Insets highlight observation of enrichment at the nuclear envelope, which was especially evident with lamin-A overexpression. (**I**) Plot shows a fourfold increase in nuclear to cytoplasmic ratio of YAP1 with increasing matrix stiffness in MSCs, except that lamin-A overexpression decreases nuclear YAP1. (**J**) YAP1 was also bimodally distributed on substrates of intermediate stiffness (10 kPa). (**K**) YAP1 protein and mRNA levels in tissues of increasing stiffness showed nonmonotonic trends, with the mRNA data averaged from human and mouse microarrays. All points are significantly different, as indicated ($n \geq 3$ imaging, IF, and immunoblot experiments).

Enzymatically derived from vitamin A, RA regulates development and regeneration and is a normal component of serum (~10 nM). It enhances lamin-A expression in embryonic carcinoma cells (*54*) while repressing lamins in adult granulocyte differentiation (*55*). Here, a lamin-A promoter driving GFP in A549 cells (Fig. 5C and fig. S14B) showed that RA was repressive, whereas an antagonist (AGN-193109, denoted AGN) enhanced expression (Fig. 5D). RA nuclear receptors are the major RA effectors and were likely involved; indeed, a mutated promoter construct (Δ-*LMNA*) lacking four of six RAREs (Fig. 5B and fig. S14B) showed no significant response to RA or AGN (Fig. 5D). Immunoblots of endogenous lamin-A confirmed RA responsiveness (fig. S15, A to E), and a pharmacodynamics study demonstrated nM activity (*56*) as well as a twofold dynamic range in lamin-A:B expression (fig. S15, F and G). MSCs transfected with the promoter constructs showed an increase in expression in cells on stiff matrix compared with soft matrix for the full promoter, whereas Δ-*LMNA* showed no significant difference (Fig. 5E). Mechanical and chemical cues were combined to assess lamin-A protein in MSCs cultured on gels (Fig. 5, F and G), with the cells on stiff matrix (or on plastic) showing the expected lamin-A increase with AGN treatment and decrease with RA, but the effects were entirely suppressed on soft matrix. Matrix elasticity is thus upstream of the RA pathway, which is, in turn, upstream of lamin-A transcription.

Based on RA pathway effects on lamin-A expression in cells on stiff matrix (Fig. 5F), we hypothesized measurable effects on osteogenesis. AGN indeed enhanced osteogenesis of MSCs on stiff matrix, consistent with the AGN-driven increase in lamin-A level, whereas RA suppressed osteogenesis on stiff matrix, and neither drug had

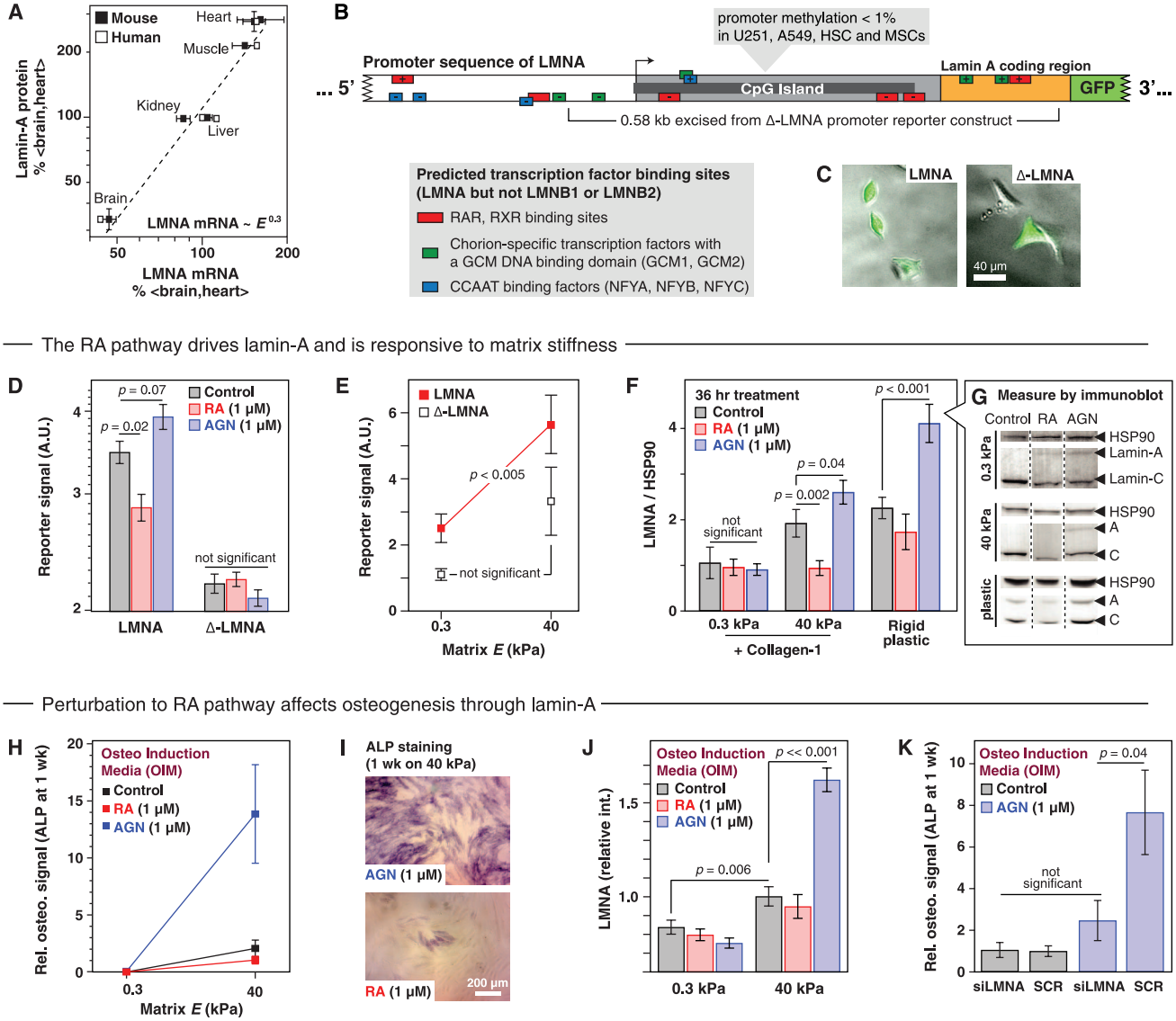

Fig. 5. Matrix stiffness is upstream of RA regulation of lamin-A transcription. (**A**) *LMNA* message correlates with protein (R^2 = 0.95) across tissue. (**B**) Promoter-reporter construct for *LMNA* is annotated with six predicted binding sites of transcription factors in RA pathway and a deletion construct (Δ-*LMNA*) lacking four RA factor binding sites. (**C**) A549 cells transfected with GFP reporter constructs. (**D**) Antagonist (AGN) and agonist (RA) increase and decrease, respectively, expression from the *LMNA* promoter-reporter and not Δ-*LMNA*; lamin-A protein shows the same response. (**E**) *LMNA* reporter activity increased significantly in MSCs grown on stiff (40 kPa) versus soft (0.3 kPa) matrix, but Δ-*LMNA* showed no significant difference. (**F**) RA and AGN regulate lamin-A in MSCs only on stiff matrix. Gels were coated with collagen-1 for comparison to cultures on untreated plastic, and immunoblotting (**G**) was performed after 36 hours culture (mean ± SEM from titration; all blots from same membrane; $P \leq 0.05$; $n \geq 3$ immunoblots). (**H**) AGN coupled with stiff matrix to increase osteogenesis, determined by ALP staining (**I**). (**J**) Increased osteogenic potential was coincident with increased lamin-A levels, measured by immunofluorescence. (**K**) Lamin-A was necessary for the increased osteogenic potential of MSCs treated with AGN as coincident treatment with siRNA against *LMNA*-abrogated osteogenesis.

an effect on MSCs on soft matrix (Fig. 5, H and I). The increased osteogenic potential of AGN-treated MSCs on stiff matrix was reflected in higher lamin-A levels (Fig. 5J), and the effect was nullified by simultaneous treatment with small interfering RNA (siRNA) against LMNA (Fig. 5K). Ectopic bone with MSC grafts has been found to be inhibited by RA and a RARG-specific agonist (*57*, *58*), and *RARG* knockout mice also exhibit osteochondral defects and live only weeks longer than the few weeks that *LMNA*-deficient mice survive (*59*–*61*). Chromatin-IP has thus far identified the *RUNX2* gene to be a target of RA transcription factors but not yet SRF (fig. S12C). *RARG* message generally increased in mouse and man versus tissue *E*, and RARG protein likewise increased in mouse tissue (Fig. 6A and fig. S12E). Fat showed low levels of RARG, and lamin-A knockdown did appear to switch RA pathways toward one that should favor adipogenesis (Fig. 4F). In MSCs, RARG was mostly nuclear in immunostaining (Fig. 6B), and its levels were relatively unperturbed by knockdown of lamin-A (fig. S12, A and B). However, RARG's nuclear-to-cytoplasmic ratio increased fourfold from soft to stiff matrix and was further suppressed by lamin-A knockdown (Fig. 6C). This effect of the lamina on nuclear translocation of RARG was similar in magnitude to the translocation of mechanosensitive YAP1 (Fig. 4I). Moreover, in cells on stiff matrix, RARG also localized to the nuclear envelope (Fig. 6B).

One of the very few other factors found in the nuclear proteome that correlated well with tissue *E* was polymerase I and transcript release factor (PTRF) (fig. S1). *PTRF* transcript also correlated strongly with both *LMNA* and *COL1A1* across mouse and man transcriptomes (fig. S2D), and lamin-A knockdown strongly decreased *PTRF* levels in MSCs (fig. S13C). Consistent with *PTRF* being downstream of lamin-A, chromatin-IP identifies *PTRF* to be a target gene for both RA and SRF transcription factors (fig. S12C).

To directly perturb the nuclear envelope by means other than knockdown or overexpression of lamin-A, we overexpressed the membrane protein SUN2, which shuttles from the endoplasmic reticulum (ER) to the inner nuclear envelope, where it cross-links the nuclear lamina to the cytoskeleton (*48*). We hypothesized that SUN2 overexpression would saturate cross-linking sites and effectively decouple the nucleus from the cytoskeleton. SUN2 overexpression indeed produced nuclear rounding and decreased lamin-A levels (figs. S16, A and B), and it also increased cytoplasmic RARG (fig. S16C). SUN2 interacted with lamin-A based on MS analyses of proteins that coimmunoprecipitated with lamin-A (Fig. 6D) [as seen in other assays (*62*)]. Consistent with such an interaction, nucleus-enriched tissue proteomics indicated SUN2 ~ $E^{0.9}$, even though total *SUN2* showed no trend with *E* (fig. S1B). SUN2 was also found in one co-IP with RARG (Fig. 6E), which might explain RARG's enrichment at the envelope (Fig. 6B); however, interactions are likely to be indirect and/or weak at least because cytoplasmic RARG appeared more diffuse than SUN2 in the ER (fig. S16C). In the same set of experiments, a similar IP-MS approach was taken to identify possible binding partners for YAP1, particularly any factors involved in enrichment at the envelope (Fig. 4H). IP-MS (Fig. 6E) identified the YAP1 paralog TAZ (WWTR1), which has been reported to form a heterodimer with YAP1 (*63*), and YAP1 phosphorylation at a serine indicated interactions with a key kinase in the Hippo pathway (*64*). In addition, the co-IP included ELYS (AHCTF1 and MEL-28), which is known to be enriched at the nuclear envelope (*65*), but any YAP1-ELYS interactions are again likely to be indirect and/or weak and in need of further study together with RARG and SUN2. Nonetheless, our finding that lamin-A protein indirectly regulated lamin-A transcription (through factors that might also bind RARG) means that the apparent mechanoregulation of message could simply be a consequence of feedback from mechanoregulated protein.

High Lamin-A Impedes Nuclear Remodeling Under Stress

Because tissue stress and matrix stiffness stabilize expression of lamin-A, which clearly conferred protection against stress-driven rupture of isolated nuclei (Fig. 2D), we sought a real-time analysis of single-cell nuclear responses to stress. Nuclei in diverse cell types—including embryonic stem cells with very low lamin-A (*20*)—were aspirated into micropipettes at stresses of kPa, which is similar to tensions in cells (*5*) and also similar in magnitude to tissue stiffnesses (Fig. 1D). Each nucleus was found to extend in a viscoelastic manner within just ~10 s (Fig. 7, A to C). As a function of lamin-A:B stoichiometry, the effective viscosity increased more rapidly than the effective elasticity (Fig. 7, D and E). Lamin-B thus acted like the elastic walls of a balloon, driving the nucleus to return to its original shape, whereas lamin-A contributed more as a highly viscous fluid within the balloon to impede deformation. Consistent with this physical distinction between lamin isoforms, fluorescence correlation spectroscopy has shown lamin-A to be mobile and lamin-B to be immobile (*24*).

In vivo cell migration has been seen to dynamically distend a nucleus by twofold or more reversibly over tens of minutes (*20*). On such long time scales, stress might extend a nucleus locally to a length similar to a typical chromosome (e.g., 5 μm), but a stiffness-limited extension rate is likely important because elongation of chromatin within the extended nucleus (*20*) implies rearrangements of chromatin-lamina interactions (*66*, *67*). We hypothesized therefore that across distinct cell types with very different epigenetic features, the time needed for the nucleus to rearrange or relax, τ, would depend primarily on lamin-A level (Fig. 7F). Indeed, for a broad range in lamin-A:B ratio across various glial, epithelial, and mesenchymal cell types with or without knockdown or overexpression of lamin-A, τ varied ~10,000-fold. This level of variation is similar to time-scale differences that would be obtained in aspirating water versus honey. As functions of lamin-A:B stoichiometry, the steeply positive power laws [τ ~ (Lamin-A:B)$^{2.5}$] (fig. 7, G and H) were also consistent with predictions from polymer physics (Box 1). The scaling revealed a dominating contribution of lamin-A to nuclear viscosity relative to lamin-B's contribution to nuclear elasticity. While low lamin-A proved insufficient to protect against extreme stresses that completely disrupted chromatin packing (Fig. 2D), the 30-fold higher lamin-A in stiff tissue relative to soft tissue (Fig. 1D) would tend to impede rapid nuclear distension. Thus, high stresses and/or stress fluctuations typical in a stiff tissue such as muscle, heart, or bone (high *E* in Fig. 1D) will not "shock" the nucleus and disrupt chromosome territories or chromatin-lamina interactions (Fig. 7I) that contribute to epigenetic regulation (*66*, *67*) or, in the extreme, cause DNA breaks.

Many progeroid syndromes—beyond progeria due to defective lamin-A—involve mutations that impair proteins important to DNA repair (*68*). The finding by IP-MS (Fig. 6D) that one DNA repair factor, XRCC6 (Ku70) (*69*), pulled down with lamin-A from two cell types using high-affinity antibody and that *XRCC6* was slightly but consistently decreased upon *LMNA* knockdown (fig. S13C) suggests a mechanochemical link of DNA repair to lamin-A. Further study is motivated by a previous MS finding that both XRCC6 and ELYS pull down with biotinylated lamin-A bound with low affinity (μM) to a streptavidin analog (*70*). Regardless of a possible molecular link to DNA repair factors, lamin-A clearly protects the nucleus against stress.

Systems Mechanobiology: Core Gene Circuit Yields Steady-State Scaling for Lamin-A

High matrix stiffness is associated with an increased stress or tension on the nucleus and promotes lamin-A expression and a physically stiffer nucleus. If we thus assume that tension in the rope-like supercoil assemblies of lamin-A filaments suppresses the affinity of an enzyme that initiates phosphorylation/solubilization/degradation of lamin-A, then a parsimonious gene circuit (Fig. 8A) could be modeled mathematically (Fig. 8, B and C), with lamin-A protein effectively feeding back on its own message. Mechanics was explicitly included only in the stress-dependent protein turnover term; synthesis of message and protein as well as degradation of message were all assumed to be linear, with all rate constants chosen to be of order unity. As a test of whether such a model could capture key experimental trends, computational results showed that steady-state lamin-A levels scaled with (Tension)$^{0.7}$, which parallels the scaling of lamin-A with tissue microelasticity *E* (Fig. 1D), noting that Tension ~ *E*. Kinetic measurements of lamin-A changes with cell mechanical perturbations are clearly needed to further develop such a model.

Discussion

Matrix elasticity is upstream of lamin-A levels in the 3D xenograft model as well as in the 2D

RARG increases with tissue stiffness and its location in cultured cells is modulated by matrix *E*

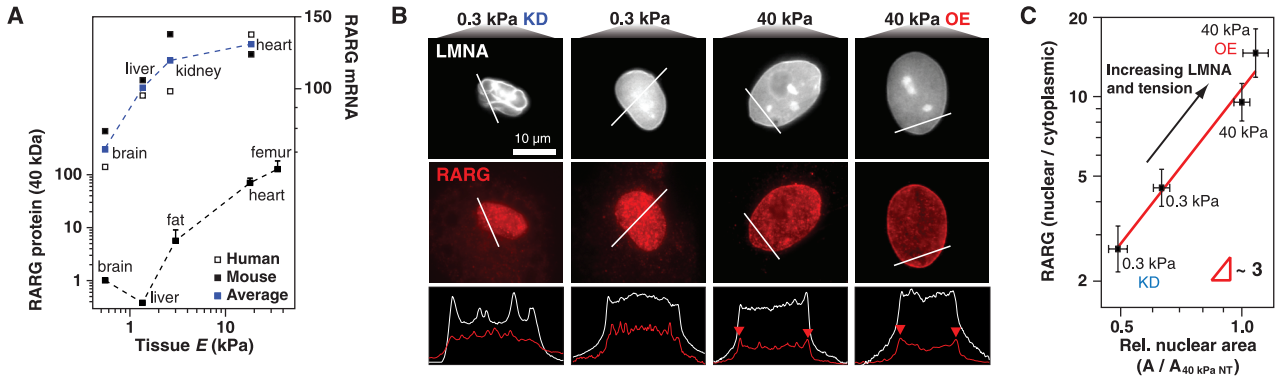

Immunoprecipitation-MS identifies potential binding partners

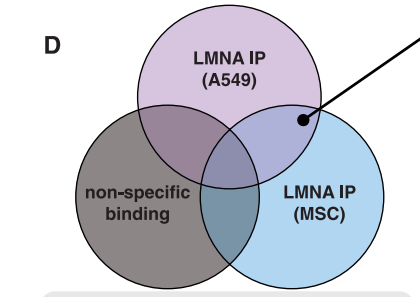

*** LMNA detection** (also detected in non-specific set)
- ▶ Peptides detected with phosphorylation at: Ser[22], Ser[390] (CDK1 sites), Ser[404] (AKT site), Thr[424] (not previously reported).
- ▶ Three peptides specific to lamin-A.
- ▶ One peptide specific to lamin-C.

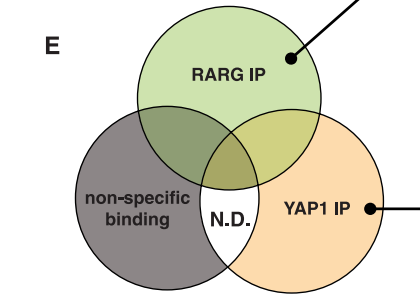

YAP1 detection
- ▶ One peptide detected with phosphorylation at Ser[109] (LATS site).
- ▶ One peptide specific to YAP1 spliceoform.

WWTR1 detection
- ▶ One peptide detected with phosphorylation at Ser[89] (LATS site).

IP from MSC lysate with LMNA (60 - 80 kDa)†	Annotation	# Peptides (≥5)
* Lamin A,C (LMNA, 65 and 74 kDa)	Nucl. envelope	57
Lamin B2 (LMNB2, 68 kDa)	Nucl. envelope	22
▶ SUN domain-containing protein 2 (SUN2, 80 kDa)	Nucl. envelope	21
Lamin B1 (LMNB1, 66 kDa)	Nucl. envelope	21
Lamina-associated polypeptide 2, isoform alpha (TMPO, 51 kDa)	Nucl. envelope	12
Torsin-1A-interacting protein 1 (TOR1AIP1, 66 kDa)	Nucl. envelope	8
X-ray repair cross-complementing protein 6 (XRCC6, 70 kDa)	Chromatin binding	22
Heterochromatin protein 1-binding protein 3 (HP1BP3, 61 kDa)	Chromatin binding	11
FACT complex subunit (SSRP1, 81 kDa)	Chromatin binding	8
ATP-dependent RNA helicase (DDX18, 75 kDa)	Chromatin binding	8
Nucleolar protein 58 (NOP58, 60 kDa)	RNA / nucleolar	13
Ribosomal L1 domain-containing protein 1 (RSL1D1, 55 kDa)	RNA / nucleolar	9
RNA-binding protein 39 (RBM39, 59 kDa)	RNA / nucleolar	6
Splicing factor U2AF 65 kDa subunit (U2AF2, 54 kDa)	RNA / nucleolar	6
Pescadillo homolog (PES1, 68 kDa)	RNA / nucleolar	5
† Also detected with >2 peptides / protein in A549s	100 % Nuclear / 0 % Cytoplasmic	

IP from A549 lysate with RARG (30 - 80 kDa)	Annotation	# Peptides (≥4)
▶ SUN domain-containing protein 2 (SUN2, 80 kDa)	Nucl. envelope	4
Retinoic acid receptor gamma (RARG, 43 - 50 kDa)	Chromatin binding	4
Something about silencing protein 10 (UTP3, 55 kDa)	Chromatin binding	4
Nuclear receptor coactivator 5 (NCOA5, 66 kDa)	Chromatin binding	4
E3 ubiquitin-protein ligase (TRIM21, 54 kDa)	RNA / nucleolar	14
ELAV-like protein 1 (ELAVL1, 36 kDa)	RNA / nucleolar	11
RNA-binding protein Raly (RALY, 32 kDa)	RNA / nucleolar	10
Eukaryotic initiation factor 4A-III (EIF4A3, 47 kDa)	RNA / nucleolar	6
Nucleophosmin (NPM1, 33 kDa)	RNA / nucleolar	5
Transformer-2 protein homolog beta (TRA2B, 34 kDa)	RNA / nucleolar	5
Heterogeneous nuclear ribonucleoprotein A0 (HNRNPA0, 31 KDa)	RNA / nucleolar	5
Pre-mRNA-processing factor 19 (PRPF19, 55 kDa)	RNA / nucleolar	5
Ribosome biogenesis protein WDR12 (WDR12, 48 kDa)	RNA / nucleolar	4
Serine/arginine-rich splicing factor 10 (SRSF10, 31 kDa)	RNA / nucleolar	4
Probable ATP-dependent RNA helicase (DDX6, 54 kDa)	RNA / nucleolar	4
Calcium/calmodulin-dependent protein kinase type II alpha (CAMK2A, 54 kDa)	Cytoplasmic	7
Cytochrome b-c1 complex subunit 1, mitochondrial (UQCRC1, 53 kDa)	Cytoplasmic	5
Calcium/calmodulin-dependent protein kinase type II beta (CAMK2B, 73 kDa)	Cytoplasmic	4
Aldehyde dehydrogenase X, mitochondrial (ALDH1B1, 57 kDa)	Cytoplasmic	4
Eukaryotic translation termination factor 1 (ETF1, 49 kDa)	Cytoplasmic	4
	75% Nuclear / 25 % Cytoplasmic	

IP from A549 lysate with YAP1 (30 - 80 kDa)	Annotation	# Peptides (≥3)
Yorkie homolog (YAP1, 54 kDa)	Chromatin binding	15
WW domain-containing transcription regulator protein 1 (WWTR1, 44 kDa)	Chromatin binding	5
Protein-glutamine gamma-glutamyltransferase 2 (TGM2, 77 kDa)	Cytoplasmic	3
Histone acetyltransferase (KAT7, 71 kDa)	Chromatin binding	3
▶ Protein ELYS (AHCTF1, 252 kDa)	Nucl. pore complex	3

Median ion current

Fig. 6. Lamin-A protein regulates nuclear translocation of RA receptor. (**A**) RARG protein and message (mouse and human average) increased in tissues of increasing stiffness. (**B**) High-resolution confocal microscope images of RARG in MSCs on matrices of various stiffnesses and with knockdown or overexpression of lamin-A. Nuclear midsections showed cytoplasmic RARG on soft matrix and increasing localization of RARG to the nuclear periphery with increasing lamin level. (**C**) Nuclear-to-cytoplasmic ratio of RARG scales with matrix elasticity and was directly affected by lamin-A knockdown or overexpression. All points are significantly different, as indicated ($n \geq 3$ IF experiments). (**D**) Proteins coimmunoprecipitated with lamin-A, common to both A549s and MSCs but not found in a nonspecific control (against GFP, which was not present in the sample), were analyzed by MS. (**E**) Proteins associated with immunoprecipitated RARG or YAP1, but not with control samples (a combined list of proteins precipitating with antibody to GFP, not present in the sample, and proteins binding to antibody-free beads). Protein lists were compiled by combining hits from duplicate experiments. The nuclear membrane protein SUN2 was common to both lamin-A and RARG immunoprecipitation experiments. N.D., not detected.

culture models. Lamin-A knockdown in MSCs indeed did not affect expression of the key collagens that scale with tissue stiffness but did suppress the SRF pathway that promotes expression of abundant actin-myosin cytoskeletal components. Soft matrix likewise appears to minimize cytoskeletal stress or tension on the wrinkled nucleus, which thus minimizes stress on lamin-A and thereby favors its phosphorylation and turnover. Low lamin-A protein limits its own transcription by altering nuclear localization of RA transcription factors: Soft matrix and low lamin-A produce the highest cytoplasmic levels of RARG, and the same conditions not only showed the lowest *LMNA* promoter activity but also showed no significant changes of lamin-A protein levels with added RA and AGN. With adipogenic stimuli that include a soft matrix, partial knockdown of lamin-A in MSCs (to lamin-A:B ~ 3) maximized in vitro adipogenesis, consistent with A:B scaling in tissue profiling.

At least for stiff tissue cells with abundant RARG, the response in the vitamin A pathway was also downstream of matrix stiffness. Stiff matrix and high lamin-A led to the highest nuclear levels of RARG, and the same conditions showed not only the highest *LMNA* promoter activity but also about a twofold variation in lamin-A levels upon addition of RA and AGN. AGN enhanced lamin-A, typical of a stiff tissue, and MSC osteogenesis also increased. Differentiation might also be sensitive to splice-forms because AGN increased the A splice-form of *LMNA*, as did forced overexpression, and tissue profiling showed bone has more A than C splice-form, all of which motivates further study. In human bone tissue, lamin-A is among the 20 most abundant proteins detected by MS, together with several SRF-regulated gene products (ACTB, ACTA2, and MYL9) (*71*), and whereas SRF positively regulates a key transcription factor (RUNX2) in osteogenesis (*45*), chromatin-IP has thus far identified the *RUNX2* gene to be a direct target of RA transcription factors and not of SRF. Lamin-A overexpression in MSCs on stiff matrix not only enhanced osteogenesis but also produced a modest decrease in nuclear YAP1 consistent with the measured nonmonotonic responses of YAP1 across tissues. A complex interplay between YAP1 and/or lamin-A might reconcile past observations that YAP1 promotes osteogenesis (*11*) but also inhibits RUNX2 (*72*); switching between YAP1 and TAZ (WWTR1) activities is also possible, because TAZ can promote osteoblast differentiation of MSCs by enhancing RUNX2-dependent transcriptional

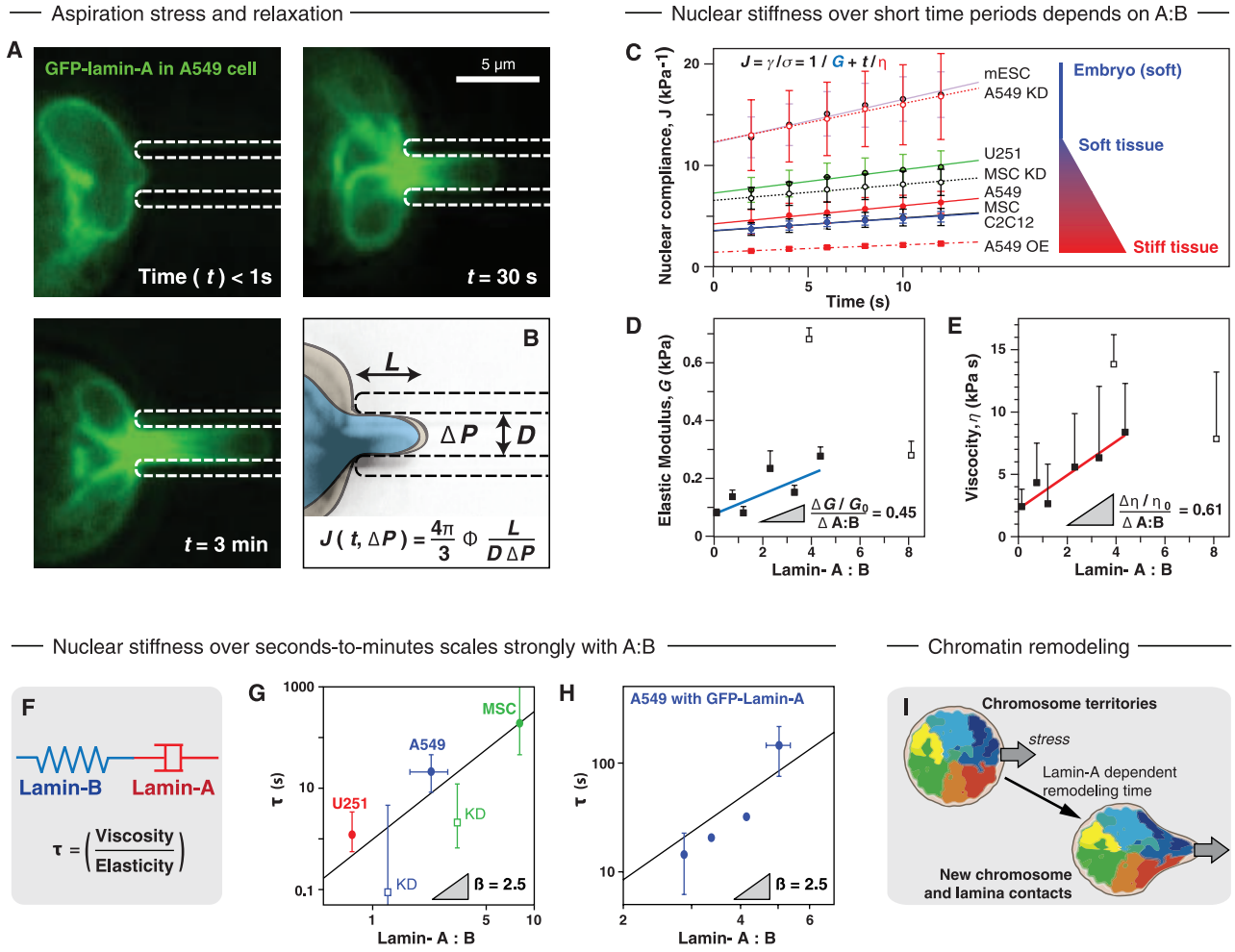

Fig. 7. Lamin-A confers a viscous stiffness to nuclei that impedes nuclear remodeling by stress. (**A**) Micropipette aspiration of an A549 cell nucleus expressing GFP-lamin-A shows extension of the lamina with time. (**B**) Schematic showing how nuclear compliance is calculated from image analysis as a function of time and aspiration pressure. (**C**) Modeling compliance over the first 12 s of deformation, with contributions from elasticity (G) and viscosity (η) in nuclei with different lamina compositions. (**D** and **E**) Relationship between the characteristic lamin-A:B ratio and (D) the elastic modulus or (E) the viscosity. The outlier points, A549 OE and MSC, indicated by open symbols, were omitted from the linear fits. (**F**) The response of the lamina can be considered as a combination of elastic and viscous components, with an elongation response time, τ (see Box 1). τ was calculated for nuclei extended to ~5 μm by micropipette aspiration over seconds-to-minutes time scales in cells with different lamin-A:B ratios (**G**) and in A549 cells overexpressing GFP-lamin-A (**H**). Lamin ratios were calculated from a combination of immunoblotting and MS methods. The scaling of τ with changes in the lamin-A:B ratio, β, was found to be the same in both experiments. (**I**) A potential biological consequence of nuclear distension is the remodeling of chromosome territories and chromatin-envelope interactions. All points are significantly different where indicated ($n \geq 3$ nuclei).

activation (73), and the IP-MS data suggested a YAP1-TAZ interaction. Regardless, the proposed gene circuit for lamin-A seems to be one important core module that modulates various transcriptional pathways (RA, SREBP1, SRF, and YAP1) in enhancing matrix elasticity–directed differentiation.

Our multifaceted approach to a broad range of solid tissues using proteomics and transcriptomics plus knockdown in a highly plastic stem cell that expresses abundant lamin-A seems useful for generic pathway analyses. Indeed, polymerase I and transcript release factor (PTRF) was one of the few factors that not only correlated well with tissue *E*, and decreased with lamin-A knockdown, but also is a known target of RA and SRF transcription factors. The additional fact that mutations in human *PTRF* cause muscular dystrophies and lipodystrophies that also result from *LMNA* mutations (74) suggests an additional feedback into intersecting pathways. Understanding the physiological determinants of normal lamin levels could thus begin to clarify why some laminopathies have phenotypes that dominate in a particular subset of tissues.

Beyond a role in regulating transcription factors, the lamins interact directly with many other nuclear proteins and form lamina-associated domains (LADs) that are repressive regions rich in heterochromatin (66, 67). LADs have roles in some aspects of lineage-specific differentiation, and so the 30-fold variations in lamin-A with tissue stiffness imply a physical regulation of LADs. The relative abundance of A versus B-type lamins could be critical, and despite the weak scaling observed for lamin-B1 and -B2 in solid tissues, nucleated blood cells show large variations in lamin-B (55). Mechanisms of regulation of lamin-Bs within soft marrow are thus far unclear, but human hematopoietic stem cells (HSCPs) do exhibit a soft nuclear phenotype (20) consistent with soft marrow. The MSCs studied herein were also human bone marrow–derived, and their potential to contribute to both rigid bone and softer marrow fat is relevant to marrow microenvironments and to a distinct influence of osteoblasts and adipocytes on HSCPs (75).

Lamins as Stress-Modulated Lineage Enhancers

Neither A- nor B-type lamins are essential for lineage induction or specification. *LMNA* knockout mice develop all tissues but die weeks after birth with growth retardation of connective tissues and also muscular dystrophy (59–61) that is very severe compared with the prototypical mouse model of muscular dystrophy (Dmd^{mdx}), which lives for 2 years (76). *LMNA* expression is therefore essential for maturation and survival against the incessant stressing in adult tissues, and once the lamin level matches to the stress, then the optimal level can enhance a prespecified lineage. The weakly modulated B-type lamins are also dispensable in embryonic development; lamin-B knockout mice die at birth as neurons apoptose (34) in migration through the dense midcortex, which stretches normal nuclei by four- to fivefold (20). The lamin knockouts thus suggest important structure-stabilizing roles for the lamins, but the findings reveal lamin-A to be the most stress-inducible differentiation-enhancing factor and lamin-B2 to be the most refractory. Distinct regulation of stress-inducible isoforms versus constitutive isoforms is reminiscent of the heat shock protein 90 isoform family that constitutes roughly 2% of protein mass in mammalian cells (77). This seems no coincidence because mechanical work and heat are, after all, two key terms in inescapable thermodynamic laws that cells have evolved and adapted to.

Although softening or stiffening the nucleus through lamin-A knockdown or overexpression could physically modulate the cytoskeleton and cell spreading in a manner similar to matrix elasticity, nuclear effects were not as large as matrix effects. This could be because cytoskeleton-nuclear interactions are several times smaller in net area than cell-matrix interactions; from this purely physical point of view, matrix elasticity should be upstream of nuclear mechanics and lamin regulation. In addition, tissue elasticity does not appear greatly affected by nuclear mechanics: In a stiff tissue such as skeletal muscle ($E \sim 12$ kPa), nuclei make up just 0.15% of muscle volume, whereas cytoskeletal volume is almost 60% (78), and in a much softer tissue such as liver ($E \sim 1.5$ kPa), the nuclear-to-cytoplasmic percentage is much higher but still small at around 6 to 7% (79). Nonetheless, lamin-A:B levels did adjust by about twofold in primary adult cells (MSCs) as well as cell lines (U251 and A549) in response to tissue microenvironments in vivo, or else soft gels and stiff substrates (including rigid plastic), and/or soluble factors in the RA pathway. Although this typical range for the nuclear "mechanostat" is a fraction of the lamin-A:B range found across adult tissues, fibroblasts with abundant lamin-A not only lose nearly all of it when reprogrammed to induced pluripotent stem cells (iPSCs) (80) but also are more efficiently reprogrammed (>20-fold) by RA agonists (81) that our results suggest suppress lamin-A. Modifiers beyond the RA pathway could thus couple to the lamin mechanostat and further amplify its range up or down to better match microenvironment stiffness and stress.

Common Structures Under Tension: Supercoiled Helical Assemblies

The α-helical coiled coil and the collagen triple helix are the two known motifs for supercoiled multistranded proteins (82). Both structures tend to assemble into rope-like fibers that are often subjected to tension, but how tension affects structure or turnover is understudied. Collagen-I fibers are degraded more slowly by matrix protease when tension is applied (83), consistent with the well-known atrophy of disuse of connective tissue. The initial findings that lamin-A's filamentous coiled-coil assembly is hyperphosphorylated in cells with low tension on soft matrix is consistent with higher turnover and requires in-depth study but seems to suggest a more general model of biostabilization by tension. Lamin-B1 and -B2 appear less susceptible to this mechanochemical regulation, perhaps because farnesylation of these proteins concentrates them at the nuclear envelope.

Box 1. Polymer physics of the nuclear lamina as a shock absorber

Lamin-A's nonlinear contribution to viscosity in nuclear mechanics relative to lamin-B's contribution to solidlike elasticity can be understood from polymer physics theory. Such theories focus on averages (e.g., mean concentration) while neglecting heterogeneities in molecular states such as polydispersity (e.g., lamin-A splice-forms). For a viscoelastic object such as the model of Fig. 7F, the response time in elongation (92) is

$$\tau = (\text{Viscosity}/\text{Elasticity})$$

This is the time required for the energy stored upon rapid stretching of the elastic component to be dissipated by the viscous component. For large polymers, τ is typically seconds to minutes as opposed to nanoseconds for small solutes (92). Moreover, as a function of concentration c of polymers ranging from filamentous proteins and DNA to synthetic polymers that are concentrated enough to interact (not dilute), theory and experiment show that Viscosity ~ c^a with scaling exponent $a = 3 \pm 1$ (93, 94). Simple polymer physics therefore predicts that Viscosity ~ $[\text{Lamin-A}]^3$. The elasticity of a polymer network such as a lamin-B network, is expected to be proportional to chain density, and so Elasticity ~ $[\text{Lamin-B}]^1$. Therefore

$$\tau_{\text{theory}} \sim [\text{Lamin-A}]^3/[\text{Lamin-B}]^1 = [\text{Lamin-A:B}]^3$$

Experiment gave $\tau \sim [\text{Lamin-A:B}]^{2.5}$ (Fig. 7, G and H). Additional interactions of lamin-A with lamin-B might also affect network elasticity as Elasticity ~ $[\text{Lamin-A:B}]^b$, and our measurements indicate $b \approx 1$ for $t \to 0$ (Fig. 7, C to E) and $b \approx 0.5$ on minute time scales. Regardless, the nonlinear scaling result is similar, $\tau_{\text{theory}} \sim c^{3-b} \approx c^{2 \text{ to } 2.5}$. Lamin-A thus contributes to nuclear mechanics primarily as a concentrated polymer that slowly flows when stressed.

Additional structural modulators of supercoil assembly are also likely to contribute to pathophysiological responses. The Ig domain of lamin-A, which affects filament assembly (*84*) and interacts with a range of nuclear and nuclear-membrane proteins in addition to the SUNs (*62*) responds conformationally to stress. Phosphorylation at the nearby Ser^{390}, a target of CDK1 (*85*), was found to differ between wild-type lamin-A and the less stable mutant. Force-driven structural changes in the cytoskeletal protein p130Cas (*86*) also regulate its phosphorylation by tyrosine kinases, although stress increases phosphorylation of p130Cas and decreases it in lamin-A. Density of lamin-A is ultimately regulated to limit the stress per molecule, thereby adjusting nuclear strength and stiffness consistent with polymer physics and with expectations for a mechanostat. The multifunctionality of a nuclear IF protein such as lamin-A thus results in mechanosensitive feedback on multiple pathways that contribute to differentiation.

Materials and Methods

Whole-Mouse Tissue Lysis

NSG mice (NOD/SCID/IL-2Rγ$^{-/-}$) were 4 to 8 months in age ($n = 5$ mice). Protocols approved by Penn's Institutional Animal Care and Use Committee (IACUC) were used throughout. Sections of fresh tissue (~50 mm^3 heart, brain, liver, lung, kidney, and cartilage from ear) were finely chopped with a razor blade on ice. Additional experiments used flash-frozen tissue (~50 mm^3 heart, brain, liver, lung, skeletal muscle, kidney, cartilage from ear, skull, and marrow-free thigh bone), which was finely ground in a pestle and mortar on dry ice. The resulting pastes were suspended in 300-μL ice-cold lysis buffer [1x RIPA buffer (radio immunoprecipitation assay buffer), 1x NuPAGE LDS running buffer (polyacrylamide gel electrophoresis, lithium dodecyl sulfate, from Invitrogen), 0.1% protease inhibitor cocktail (PIC)]. After 30 min incubation at 4°C, samples were subjected to 5 × 20 × 1 s pulses with a probe sonicator (intermediate setting, on ice). A reducing agent was added [β-mercaptoethanol (BME) to 1%] and the samples were heated to 80°C for 10 minutes before ultracentrifugation [1 hour at 90,000 revolutions per minute (rpm) in a TLA120.1 rotor (Beckman) at 4°C]. The blue aqueous layer was then carefully extracted from between layers of fat and any insoluble pelleted material.

Nuclear Enrichment from Mouse Tissue [adapted from (87)]

Sections of flash-frozen tissue (~50 mm^3 heart, brain, liver, lung, skeletal muscle, and fat) were thawed on ice, finely chopped with a razor blade and suspended in 10 mL buffer A [10 mM 4-(2-hydroxyethyl)-1-piperazineethanesulfonic acid (HEPES), 1.5 mM $MgCl_2$, 10 mM KCl, 0.5 mM dithiothreitol (DTT) with 0.1% (PIC, Sigma Aldrich)]. The tissue was then disrupted on ice with a Dounce homogenizer [10 strokes with a loose-fitting pestle (B grade), 10 strokes with a tight-fitting pestle (A grade)] and persistent detritus was removed by passage through a 40-μm cell filter (Fisher Scientific). Crude nuclear material was then pelleted by centrifugation (10 min at 5000 rpm at 4°C), resuspended in 1 mL buffer S1 (10 mM HEPES, 0.25 M sucrose, 10 mM $MgCl_2$, and 0.1% PIC) and layered over 1 mL buffer S3 (10 mM HEPES, 1.2 M sucrose, 0.5 mM $MgCl_2$, and 0.1% PIC). Nuclear material was pelleted by centrifugation [10 min at 5000 rpm in a TLS-55 swinging-bucket rotor (Beckman) at 4°C] and resuspended in 50 μL ice-cold lysis buffer [1x RIPA, 1x NuPAGE LDS running buffer (Invitrogen), 0.1% PIC]. After 30 min incubation at 4°C, samples were subjected to 15 × 1 s pulses with a probe sonicator (low setting, on ice). Before gel electrophoresis, a reducing agent was added (BME to 1%), heated to 80°C for 10 min, and centrifuged to pellet any insoluble material (10 min at 13,300 rpm).

Mass Spectrometry

Gels from SDS–polyacrylamide gel electrophoresis (SDS-PAGE) (NuPAGE 4 to 12% bis-tris, Invitrogen) were loaded with 12 μL of lysate per lane and run at 10 min × 100 V, followed by 20 min × 160 V. Coomassie-stained polyacrylamide gel sections were washed [50% 0.2 M ammonium bicarbonate (AB) solution, 50% acetonitrile (ACN), 30 min at 37°C], dried by lyophilization, incubated with a reducing agent [20 mM tris(2-carboxyethyl)phosphine (TCEP) in 25 mM AB solution at pH 8.0, 15 min at 37°C], and alkylated [40 mM iodoacetamide (IAM) in 25 mM AB solution at pH 8.0, 30 min at 37°C]. The gel

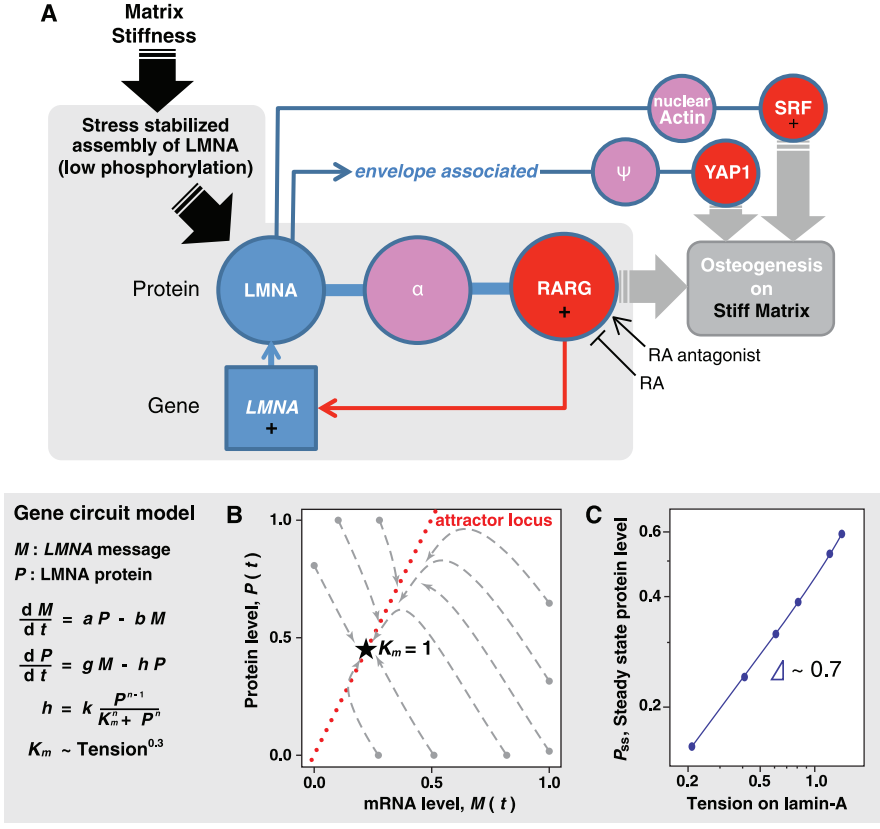

Fig. 8. A feedback-based gene circuit for lamin-A exhibits polymer physics scaling if cell tension suppresses protein turnover. (**A**) Gene circuit connecting matrix stiffness to osteogenesis; not shown is an overlapping circuit for adipogenesis on soft matrix that includes the positive regulator SREBP1. LMNA protein level is regulated by a stress-sensitive phosphorylation mechanism and feeds back into *LMNA* transcript through interaction with RARG, possibly through an intermediary, α, and can be perturbed with antagonist (AGN) or agonist (RA). LMNA protein also influences location of YAP1 (through a possible intermediary, Ψ) to drive cell fate (*11*), and LMNA regulates SRF through interaction with nuclear actin (*49*). A simple model was generated based on this circuit: Time evolution of *LMNA* mRNA (*M*) level is dependent on the LMNA protein level (*P*), whereas the protein level itself is regulated by a tension-dependent degradation term, *h*. The model shows that tension-regulated protein turnover can produce steady-state (SS) protein levels that scale with cell tension. (**B**) Trajectories of lamin-A message and protein as the model converges from a range of initial conditions to a single steady-state solution appropriate to the tension. (**C**) Setting the kinase/protease binding coefficient, K_m, to be proportional to $(\text{Tension})^{0.3}$ allows the model to generate steady-state lamin scaling with tension consistent with experiment (Fig. 1D).

sections were dried by lyophilization before in-gel trypsinization [20 μg/mL sequencing grade modified trypsin in buffer as described in the manufacturer's protocol (Promega), 18 hours at 37°C with gentle shaking]. The resulting solutions of tryptic peptides were acidified by the addition of 50% digest dilution buffer (60 mM AB solution with 3% methanoic acid).

Peptide separations (5 μL injection volume) were performed on 15-cm PicoFrit column (75 μm inner diameter, New Objective) packed with Magic 5 μm C18 reversed-phase resin (Michrom Bioresources) using a nanoflow high-pressure liquid chromatography system (Eksigent Technologies), which was coupled online to a hybrid LTQ-Orbitrap XL mass spectrometer (Thermo Fisher Scientific) via a nanoelectrospray ion source. Chromatography was performed with solvent A (Milli-Q water with 0.1% formic acid) and solvent B (acetonitrile with 0.1% formic acid). Peptides were eluted at 200 nL/min for 3 to 28% B over 42 min, 28 to 50% B over 26 min, 50 to 80% B over 5 min, and 80% B for 4.5 min before returning to 3% B over 0.5 min. To minimize sample carryover, a fast blank gradient was run between each sample. The LTQ-Orbitrap XL was operated in the data-dependent mode to automatically switch between full-scan MS [in terms of mass m and charge z: m/z = 350 to 2000 in the Orbitrap analyzer (with resolution of 60,000 at m/z 400)] and the fragmentation of the six most intense ions by collision-induced dissociation in the ion-trap mass analyzer.

Raw mass spectroscopy data was processed using Elucidator (version 3.3, Rosetta Biosoftware). The software was set up to align peaks in data from samples derived from corresponding molecular weight regions of the 1D gels. Peptide and protein annotations were made using SEQUEST (version 28, Thermo Fisher Scientific) with full tryptic digestion and up to two missed cleavage sites. Peptide masses were selected between 800 and 4500 amu with peptide mass tolerance of 1.1 amu and fragment ion mass tolerance of 1.0 amu. Peptides were searched against a database compiled from UniRef100 (November 2010) mouse and human, plus contaminants and a reverse decoy database. A deltaCn of 0.01 and mass error limit of 20 parts per million (ppm) was used, resulting in a false positive rate of ~10%. In these experiments, only proteins detected with three or more peptides were considered. [Therefore, for positive identification of a protein, $P < (0.1)^3$.] The peptide database was modified to search for alkylated cysteine residues (monoisotopic mass change, Δ = +57.021 Da) and oxidized methionine (Δ = +15.995 Da). In proteomic profiling experiments, we also considered the acetylation of lysine (Δ = +42.011 Da), methylation of lysine and arginine (Δ = +14.016 Da), hydroxylation of lysine, proline, aspartate, and asparagine (Δ = +15.995 Da), and phosphorylation of serine, tyrosine, threonine, histidine, and aspartate (Δ = +79.966 Da). In experiments in which cysteine residues were labeled with monobromobimane (mBBr), the modification was searched for in three possible oxidation states (Δ = +133.053 Da, Δ = +150.056 Da, and Δ = +151.064 Da). Peptides derived from the autolysis of trypsin were considered to be contaminants and were not used in subsequent calculations. When evaluating total ion current, only signals from annotated peptides were summed. The Peptide Ratio Fingerprint (PRF) algorithm was coded for Mathematica (version 8, Wolfram Research) and was used for all MS protein quantitation (*88*). Synthetic, HPLC-purified versions of key peptides were purchased from GenScript (figs. S4 and S8, E and F) and were used to confirm MS detection and linearity of response.

Determination of Absolute Lamin Ratio (A + C)/(B1 + B2)

When comparing the lamin composition in samples from two conditions—for example, a control and a knockdown—MS analysis allowed the relative (fold) change in lamin level to be established in the lamin-A,C overlap region, lamin-B1, lamin-B2, and an overlap peptide that is common to all lamins, LLEGEEER (fig. S4). These ratios were combined to calculate the absolute ratio between A-type and B-type lamin

$$\left(\frac{[\text{Lamin A}]}{[\text{Lamin B}]}\right)_{\text{condition1}} = \frac{f_{\text{LLEGEEER}} - f_{\text{Lamin B1, B2}}}{f_{\text{Lamin A}} - f_{\text{LLEGEEER}}}$$

where f represents the fold change in protein level in going from condition 1 (e.g., the control) to condition 2 (e.g., the knockdown). Because this measurement was dependent on detection of a single peptide, it was repeated a number of times to obtain a confident measure of the A:B ratio in condition 1. Subsequent derivation of the ratio in condition 2 had no additional dependence on detection of LLEGEEER.

$$\left(\frac{[\text{Lamin A}]}{[\text{Lamin B}]}\right)_{\text{condition2}} = \left(\frac{[\text{Lamin A}]}{[\text{Lamin B}]}\right)_{\text{condition1}} \times \frac{f_{\text{Lamin A}}}{f_{\text{Lamin B1, B2}}}$$

The parameter $f_{\text{Lamin B1,B2}}$ represents the overlap between the two B-type lamins. Although we show that lamin-B1 and lamin-B2 were detected in similar quantities and that neither change to a great extent compared with lamin-A,C (Fig. 1F and fig. S4D), we derived this value from median ion current values.

$$R = \frac{\text{Median ion current}_{\text{Lamin B1}}}{\text{Median ion current}_{\text{Lamin B2}}}$$

$$f_{\text{Lamin B1, B2}} = \frac{R^* f_{\text{Lamin B1}} + f_{\text{Lamin B2}}}{1 + R}$$

The tissue experiments shown in Fig. 1D were measured relative to a "condition 1" average of brain and heart denoted as <brain, heart>, a reference point chosen in the middle of the elasticity scale for which we had many tissue duplicates (n = 4 mice for heart and brain). A lysate of A549 cells (n = 3 culture replicates) was used as a reference point for all cell measurements in Fig. 1D. MS measurements of isolated nuclear material were made in technical triplicates.

Fluid Shear on Isolated Nuclei

Isolated A549 nuclei suspended in nuclei wash buffer were diluted to about 250 nuclei per μL. Nuclei samples were labeled with 150 μM mBBr and immediately loaded into a cone and plate rheometer (Bohlin Gemini) with the stage heated to 37°C. To control for baseline labeling at this temperature an identical sample was placed in a 37°C water bath. Samples were spun in the rheometer for 10 to 40 min with a 10-μm gap. Shear force varied from 0.5 to 5 Pa in different samples. After the run, labeling in both sample and control was quenched with 2 mM glutathione. For each condition, a sample was taken to be imaged. Samples were prepared for MS as described above. To facilitate identification of the labeled lamin Ig domain peptide by MS, recombinantly expressed, mBBr labeled, and trypsinized lamin Ig domain was spiked into control A549 lysate.

Labeling Cysteines with mBBr in Adherent Cells

Low-passage primary human MSCs were seeded on soft (0.3 kPa), intermediate (10 kPa), and stiff (40 kPa) polyacrylamide gels and cultured for 2 days in Dulbecco's minimum essential medium (Invitrogen) supplemented with 10% fetal bovine serum. A549 cells cultured on plastic were transfected with wild-type and R453W-mutant GFP-lamin constructs using Lipofectamine 2000 (LF2k, Invitrogen) per the manufacturer's protocol. Cells were washed with phosphate-buffered saline (PBS) before labeling with freshly prepared 400 μM mBBr in PBS at 37°C. After 10 min, the cells were harvested by trypsinization, suspended in ice-cold media, pelleted, and frozen at –20°C. Samples were enriched before MS analysis by immunoprecipitation of lamin-A or GFP, as described below. In addition, a portion of cells were washed thoroughly after mBBr labeling, fixed with formaldehyde, and immunostained for lamin-A (mouse monoclonal sc-7292, Santa Cruz), α-smooth muscle actin (mouse monoclonal A5228, Sigma Aldrich), and nonmuscle myosin-IIA (rabbit polyclonal M8064, Sigma Aldrich) for imaging at high resolution.

Model of Lamin Transcript and Protein Levels

The rate equations for lamin-A protein (P) and mRNA (M) concentrations, respectively, include synthesis and degradation

$$\frac{dM}{dt} = aP - bM$$
$$\frac{dP}{dt} = gM - hP$$

where a is first-order protein-induced mRNA production rate constant, b is first-order mRNA degradation rate constant, g is first-order mRNA

translational rate constant, h is force-dependent protein degradation, modeled as

$$h = k\frac{P^{n-1}}{K_m^n + P^n}$$

where k is maximal protein degradation rate, n is cooperativity coefficient ≥ 2 typical of dimer-based interactions, and K_m is affinity of kinase/protease for the lamin meshwork, which increases with stress or tension sustained by the meshwork. Like pulling on a coiled rope, the key idea is that tension on this meshwork of lamin-A coiled-coil protein squeezes out free volume and sequesters the enzyme's binding site on lamin-A. At steady-state

$$\frac{dP}{dt} = \frac{dM}{dt} = 0$$

thus yielding nonzero steady-state values for P and M

$$\{P_{SS}, M_{SS}\} = \left\{\frac{bk}{ga} - \frac{1}{2}\sqrt{\left(\frac{bk}{ga}\right)^2 - 4K_m}, \frac{aP_{SS}}{b}\right\}$$

Based on the steady-state analysis above, a solution only exists if

$$\left(\frac{bk}{ga}\right)^2 - 4K_m > 0$$

Time evolution of P and M was modeled in Mathematica (Wolfram) with example trajectories in Fig. 8B as a phase plot of $P(t)$ versus $M(t)$ converging to $\{P_{SS}, M_{SS}\}$. Although steady-state values depend on the various rate constants, we assumed all to be important and of order ~1 as we focus on K_m: At high stresses where lamin-A assembly is favored, K_m increases so that lamin-A phosphorylation/degradation decreases. Plotting P_{SS} against different values for K_m fit a power-law $P_{SS} \sim K_m^2$. If $K_m = (\text{tension})^{0.3}$, then $P_{SS} \sim (\text{tension})^{0.7}$, as found experimentally for lamin-A (Fig. 8C).

References and Notes

1. H. M. Frost, Bone "mass" and the "mechanostat": A proposal. *Anat. Rec.* **219**, 1–9 (1987). doi: 10.1002/ar.1092190104; pmid: 3688455
2. V. Vogel, M. Sheetz, Local force and geometry sensing regulate cell functions. *Nat. Rev. Mol. Cell Biol.* **7**, 265–275 (2006). doi: 10.1038/nrm1890; pmid: 16607289
3. B. P. C. Chen *et al.*, DNA microarray analysis of gene expression in endothelial cells in response to 24-h shear stress. *Physiol. Genomics* **7**, 55–63 (2001). pmid: 11595792
4. D. E. Discher, P. Janmey, Y. L. Wang, Tissue cells feel and respond to the stiffness of their substrate. *Science* **310**, 1139–1143 (2005). doi: 10.1126/science.1116995; pmid: 16293750
5. A. J. Engler, S. Sen, H. L. Sweeney, D. E. Discher, Matrix elasticity directs stem cell lineage specification. *Cell* **126**, 677–689 (2006). doi: 10.1016/j.cell.2006.06.044; pmid: 16923388
6. R. J. Pelham Jr., Y. Wang, Cell locomotion and focal adhesions are regulated by substrate flexibility. *Proc. Natl. Acad. Sci. U.S.A.* **94**, 13661–13665 (1997). doi: 10.1073/pnas.94.25.13661; pmid: 9391082
7. B. Trappmann *et al.*, Extracellular-matrix tethering regulates stem-cell fate. *Nat. Mater.* **11**, 642–649 (2012). doi: 10.1038/nmat3339; pmid: 22635042
8. S. Khetan *et al.*, Degradation-mediated cellular traction directs stem cell fate in covalently crosslinked three-dimensional hydrogels. *Nat. Mater.* **12**, 458–465 (2013). doi: 10.1038/nmat3586; pmid: 23524375
9. P. C. Georges, W. J. Miller, D. F. Meaney, E. S. Sawyer, P. A. Janmey, Matrices with compliance comparable to that of brain tissue select neuronal over glial growth in mixed cortical cultures. *Biophys. J.* **90**, 3012–3018 (2006). doi: 10.1529/biophysj.105.073114; pmid: 16461391
10. T. A. Ulrich, E. M. de Juan Pardo, S. Kumar, The mechanical rigidity of the extracellular matrix regulates the structure, motility, and proliferation of glioma cells. *Cancer Res.* **69**, 4167–4174 (2009). doi: 10.1158/0008-5472.CAN-08-4859; pmid: 19435897
11. S. Dupont *et al.*, Role of YAP/TAZ in mechanotransduction. *Nature* **474**, 179–183 (2011). doi: 10.1038/nature10137; pmid: 21654799
12. A. J. Engler *et al.*, Myotubes differentiate optimally on substrates with tissue-like stiffness: Pathological implications for soft or stiff microenvironments. *J. Cell Biol.* **166**, 877–887 (2004). doi: 10.1083/jcb.200405004; pmid: 15364962
13. A. J. Engler *et al.*, Embryonic cardiomyocytes beat best on a matrix with heart-like elasticity: Scar-like rigidity inhibits beating. *J. Cell Sci.* **121**, 3794–3802 (2008). doi: 10.1242/jcs.029678; pmid: 18957515
14. P. M. Gilbert *et al.*, Substrate elasticity regulates skeletal muscle stem cell self-renewal in culture. *Science* **329**, 1078–1081 (2010). doi: 10.1126/science.1191035; pmid: 20647425
15. H. J. Kong, T. R. Polte, E. Alsberg, D. J. Mooney, FRET measurements of cell-traction forces and nano-scale clustering of adhesion ligands varied by substrate stiffness. *Proc. Natl. Acad. Sci. U.S.A.* **102**, 4300–4305 (2005). doi: 10.1073/pnas.0405873102; pmid: 15767572
16. N. Huebsch *et al.*, Harnessing traction-mediated manipulation of the cell/matrix interface to control stem-cell fate. *Nat. Mater.* **9**, 518–526 (2010). doi: 10.1038/nmat2732; pmid: 20418863
17. B. Zhao, K. Tumaneng, K. L. Guan, The Hippo pathway in organ size control, tissue regeneration and stem cell self-renewal. *Nat. Cell Biol.* **13**, 877–883 (2011). doi: 10.1038/ncb2303; pmid: 21808241
18. E. N. Olson, A. Nordheim, Linking actin dynamics and gene transcription to drive cellular motile functions. *Nat. Rev. Mol. Cell Biol.* **11**, 353–365 (2010). doi: 10.1038/nrm2890; pmid: 20414257
19. J. T. Connelly *et al.*, Actin and serum response factor transduce physical cues from the microenvironment to regulate epidermal stem cell fate decisions. *Nat. Cell Biol.* **12**, 711–718 (2010). doi: 10.1038/ncb2074; pmid: 20581838
20. J. D. Pajerowski, K. N. Dahl, F. L. Zhong, P. J. Sammak, D. E. Discher, Physical plasticity of the nucleus in stem cell differentiation. *Proc. Natl. Acad. Sci. U.S.A.* **104**, 15619–15624 (2007). doi: 10.1073/pnas.0702576104; pmid: 17893336
21. J. Lammerding *et al.*, Lamins A and C but not lamin B1 regulate nuclear mechanics. *J. Biol. Chem.* **281**, 25768–25780 (2006). doi: 10.1074/jbc.M513511200; pmid: 16825190
22. W. H. De Vos *et al.*, Repetitive disruptions of the nuclear envelope invoke temporary loss of cellular compartmentalization in laminopathies. *Hum. Mol. Genet.* **20**, 4175–4186 (2011). doi: 10.1093/hmg/ddr344; pmid: 21831885
23. H. Herrmann, S. V. Strelkov, P. Burkhard, U. Aebi, Intermediate filaments: Primary determinants of cell architecture and plasticity. *J. Clin. Invest.* **119**, 1772–1783 (2009). doi: 10.1172/JCI38214; pmid: 19587452
24. T. Shimi *et al.*, The A- and B-type nuclear lamin networks: Microdomains involved in chromatin organization and transcription. *Genes Dev.* **22**, 3409–3421 (2008). doi: 10.1101/gad.1735208; pmid: 19141474
25. N. Wang, J. D. Tytell, D. E. Ingber, Mechanotransduction at a distance: Mechanically coupling the extracellular matrix with the nucleus. *Nat. Rev. Mol. Cell Biol.* **10**, 75–82 (2009). doi: 10.1038/nrm2594; pmid: 19197334
26. G. V. Shivashankar, Mechanosignaling to the cell nucleus and gene regulation. *Annu. Rev. Biophys.* **40**, 361–378 (2011). doi: 10.1146/annurev-biophys-042910-155319; pmid: 21391812
27. J. L. V. Broers *et al.*, A- and B-type lamins are differentially expressed in normal human tissues. *Histochem. Cell Biol.* **107**, 505–517 (1997). doi: 10.1007/s004180050138; pmid: 9243284
28. C. Storm, J. J. Pastore, F. C. MacKintosh, T. C. Lubensky, P. A. Janmey, Nonlinear elasticity in biological gels. *Nature* **435**, 191–194 (2005). doi: 10.1038/nature03521; pmid: 15889088
29. M. L. Gardel *et al.*, Elastic behavior of cross-linked and bundled actin networks. *Science* **304**, 1301–1305 (2004). doi: 10.1126/science.1095087; pmid: 15166374
30. T. Kim, W. Hwang, H. Lee, R. D. Kamm, Computational analysis of viscoelastic properties of crosslinked actin networks. *PLOS Comput. Biol.* **5**, e1000439 (2009). doi: 10.1371/journal.pcbi.1000439; pmid: 19609348
31. G. Strobl, *The Physics of Polymers: Concepts for Understanding their Structure and Behavior* (Springer, New York, 2007).
32. H. J. Worman, Nuclear lamins and laminopathies. *J. Pathol.* **226**, 316–325 (2012). doi: 10.1002/path.2999; pmid: 21953297
33. D. Tunnah, C. A. Sewry, D. Vaux, E. C. Schirmer, G. E. Morris, The apparent absence of lamin B1 and emerin in many tissue nuclei is due to epitope masking. *J. Mol. Histol.* **36**, 337–344 (2005). doi: 10.1007/s10735-005-9004-7; pmid: 16283426
34. Y. Kim *et al.*, Mouse B-type lamins are required for proper organogenesis but not by embryonic stem cells. *Science* **334**, 1706–1710 (2011). doi: 10.1126/science.1211222; pmid: 22116031
35. Y. L. Yang, L. M. Leone, L. J. Kaufman, Elastic moduli of collagen gels can be predicted from two-dimensional confocal microscopy. *Biophys. J.* **97**, 2051–2060 (2009). doi: 10.1016/j.bpj.2009.07.035; pmid: 19804737
36. C. P. Johnson, H. Y. Tang, C. Carag, D. W. Speicher, D. E. Discher, Forced unfolding of proteins within cells. *Science* **317**, 663–666 (2007). doi: 10.1126/science.1139857; pmid: 17673662
37. I. Krimm *et al.*, The Ig-like structure of the C-terminal domain of lamin A/C, mutated in muscular dystrophies, cardiomyopathy, and partial lipodystrophy. *Structure* **10**, 811–823 (2002). doi: 10.1016/S0969-2126(02)00777-3; pmid: 12057196
38. R. D. Goldman, Y. Gruenbaum, R. D. Moir, D. K. Shumaker, T. P. Spann, Nuclear lamins: Building blocks of nuclear architecture. *Genes Dev.* **16**, 533–547 (2002). doi: 10.1101/gad.960502; pmid: 11877373
39. J. Bertacchini *et al.*, The protein kinase Akt/PKB regulates both prelamin A degradation and Lmna gene expression. *FASEB J.* **27**, 2145–2155 (2013). doi: 10.1096/fj.12-218214; pmid: 23430973
40. K. A. Moore, I. R. Lemischka, Stem cells and their niches. *Science* **311**, 1880–1885 (2006). doi: 10.1126/science.1110542; pmid: 16574858
41. R. Akter, D. Rivas, G. Geneau, H. Drissi, G. Duque, Effect of lamin A/C knockdown on osteoblast differentiation and function. *J. Bone Miner. Res.* **24**, 283–293 (2009). doi: 10.1359/jbmr.081010; pmid: 18847334
42. P. Scaffidi, T. Misteli, Lamin A-dependent misregulation of adult stem cells associated with accelerated ageing. *Nat. Cell Biol.* **10**, 452–459 (2008). doi: 10.1038/ncb1708; pmid: 18311132
43. M. Raab *et al.*, Crawling from soft to stiff matrix polarizes the cytoskeleton and phosphoregulates myosin-II heavy chain. *J. Cell Biol.* **199**, 669–683 (2012). doi: 10.1083/jcb.201205056; pmid: 23128239
44. P. P. Y. Lu, N. Ramanan, Serum response factor is required for cortical axon growth but is dispensable for neurogenesis and neocortical lamination. *J. Neurosci.* **31**, 16651–16664 (2011). doi: 10.1523/JNEUROSCI.3015-11.2011; pmid: 22090492
45. J. Chen *et al.*, Serum response factor regulates bone formation via IGF-1 and Runx2 signals. *J. Bone Miner.*

Res. **27**, 1659–1668 (2012). doi: 10.1002/jbmr.1607; pmid: 22434656
46. C. Baarlink, H. Wang, R. Grosse, Nuclear actin network assembly by formins regulates the SRF coactivator MAL. *Science* **340**, 864–867 (2013). doi: 10.1126/science.1235038; pmid: 23558171
47. D. N. Simon, M. S. Zastrow, K. L. Wilson, Direct actin binding to A- and B-type lamin tails and actin filament bundling by the lamin A tail. *Nucleus* **1**, 264–272 (2010). doi: 10.4161/nucl.1.3.11799; pmid: 21327074
48. D. N. Simon, K. L. Wilson, The nucleoskeleton as a genome-associated dynamic 'network of networks'. *Nat. Rev. Mol. Cell Biol.* **12**, 695–708 (2011). doi: 10.1038/nrm3207; pmid: 21971041
49. C. Y. Ho, D. E. Jaalouk, M. K. Vartiainen, J. Lammerding, Lamin A/C and emerin regulate MKL1-SRF activity by modulating actin dynamics. *Nature* **497**, 507–511 (2013). doi: 10.1038/nature12105; pmid: 23644458
50. D. J. Lloyd, R. C. Trembath, S. Shackleton, A novel interaction between lamin A and SREBP1: Implications for partial lipodystrophy and other laminopathies. *Hum. Mol. Genet.* **11**, 769–777 (2002). doi: 10.1093/hmg/11.7.769; pmid: 11929849
51. J.-T. Ayala-Sumuano *et al.*, Srebf1a is a key regulator of transcriptional control for adipogenesis. *Sci. Rep.* **1**, 178 (2011). doi: 10.1038/srep00178; pmid: 22355693
52. X. Ma *et al.*, SiRNA against Fabp5 induces 3T3-L1 cells apoptosis during adipocytic induction. *Mol. Biol. Rep.* **37**, 4003–4011 (2010). doi: 10.1007/s11033-010-0059-5; pmid: 20238174
53. B. Zhao *et al.*, TEAD mediates YAP-dependent gene induction and growth control. *Genes Dev.* **22**, 1962–1971 (2008). doi: 10.1101/gad.1664408; pmid: 18579750
54. K. Okumura, Y. Hosoe, N. Nakajima, c-Jun and Sp1 family are critical for retinoic acid induction of the lamin A/C retinoic acid-responsive element. *Biochem. Biophys. Res. Commun.* **320**, 487–492 (2004). doi: 10.1016/j.bbrc.2004.05.191; pmid: 15219855
55. A. L. Olins *et al.*, Nuclear envelope and chromatin compositional differences comparing undifferentiated and retinoic acid- and phorbol ester-treated HL-60 cells. *Exp. Cell Res.* **268**, 115–127 (2001). doi: 10.1006/excr.2001.5269; pmid: 11478838
56. C. Agarwal, R. A. S. Chandraratna, A. T. Johnson, E. A. Rorke, R. L. Eckert, AGN193109 is a highly effective antagonist of retinoid action in human ectocervical epithelial cells. *J. Biol. Chem.* **271**, 12209–12212 (1996). doi: 10.1074/jbc.271.21.12209; pmid: 8647816
57. K. Shimono *et al.*, Potent inhibition of heterotopic ossification by nuclear retinoic acid receptor-γ agonists. *Nat. Med.* **17**, 454–460 (2011).
58. W. Zhang *et al.*, Implantation of adult bone marrow-derived mesenchymal stem cells transfected with the neurotrophin-3 gene and pretreated with retinoic acid in completely transected spinal cord. *Brain Res.* **1359**, 256–271 (2010). doi: 10.1016/j.brainres.2010.08.072; pmid: 20816761
59. T. Sullivan *et al.*, Loss of A-type lamin expression compromises nuclear envelope integrity leading to muscular dystrophy. *J. Cell Biol.* **147**, 913–920 (1999). doi: 10.1083/jcb.147.5.913; pmid: 10579712
60. D. Jahn *et al.*, A truncated lamin A in the *Lmna*$^{-/-}$ mouse line: Implications for the understanding of laminopathies. *Nucleus* **3**, 463–474 (2012). doi: 10.4161/nucl.21676; pmid: 22895093
61. N. Kubben *et al.*, Post-natal myogenic and adipogenic developmental: Defects and metabolic impairment upon loss of A-type lamins. *Nucleus* **2**, 195–207 (2011). doi: 10.4161/nucl.2.3.15731; pmid: 21818413
62. F. Haque *et al.*, Mammalian SUN protein interaction networks at the inner nuclear membrane and their role in laminopathy disease processes. *J. Biol. Chem.* **285**, 3487–3498 (2010). doi: 10.1074/jbc.M109.071910; pmid: 19933576
63. M. Murakami, M. Nakagawa, E. N. Olson, O. Nakagawa, A WW domain protein TAZ is a critical coactivator for TBX5, a transcription factor implicated in Holt-Oram syndrome. *Proc. Natl. Acad. Sci. U.S.A.* **102**, 18034–18039 (2005). doi: 10.1073/pnas.0509109102; pmid: 16332960
64. B. Zhao *et al.*, Inactivation of YAP oncoprotein by the Hippo pathway is involved in cell contact inhibition and tissue growth control. *Genes Dev.* **21**, 2747–2761 (2007). doi: 10.1101/gad.1602907; pmid: 17974916
65. C. Franz *et al.*, MEL-28/ELYS is required for the recruitment of nucleoporins to chromatin and postmitotic nuclear pore complex assembly. *EMBO Rep.* **8**, 165–172 (2007). doi: 10.1038/sj.embor.7400889; pmid: 17235358
66. J. M. Zullo *et al.*, DNA sequence-dependent compartmentalization and silencing of chromatin at the nuclear lamina. *Cell* **149**, 1474–1487 (2012). doi: 10.1016/j.cell.2012.04.035; pmid: 22726435
67. W. Meuleman *et al.*, Constitutive nuclear lamina-genome interactions are highly conserved and associated with A/T-rich sequence. *Genome Res.* **23**, 270–280 (2013). doi: 10.1101/gr.141028.112; pmid: 23124521
68. T. Dechat *et al.*, Nuclear lamins: Major factors in the structural organization and function of the nucleus and chromatin. *Genes Dev.* **22**, 832–853 (2008). doi: 10.1101/gad.1652708; pmid: 18381888
69. B. L. Mahaney, K. Meek, S. P. Lees-Miller, Repair of ionizing radiation-induced DNA double-strand breaks by non-homologous end-joining. *Biochem. J.* **417**, 639–650 (2009). doi: 10.1042/BJ20080413; pmid: 19133841
70. N. Kubben *et al.*, Identification of differential protein interactors of lamin A and progerin. *Nucleus* **1**, 513–525 (2010). pmid: 21327095
71. R. D. A. M. Alves *et al.*, Unraveling the human bone microenvironment beyond the classical extracellular matrix proteins: A human bone protein library. *J. Proteome Res.* **10**, 4725–4733 (2011). doi: 10.1021/pr200522n; pmid: 21892838
72. S. K. Zaidi *et al.*, Tyrosine phosphorylation controls Runx2-mediated subnuclear targeting of YAP to repress transcription. *EMBO J.* **23**, 790–799 (2004). doi: 10.1038/sj.emboj.7600073; pmid: 14765127
73. J. H. Hong *et al.*, TAZ, a transcriptional modulator of mesenchymal stem cell differentiation. *Science* **309**, 1074–1078 (2005). doi: 10.1126/science.1110955; pmid: 16099986
74. Y. K. Hayashi *et al.*, Human PTRF mutations cause secondary deficiency of caveolins resulting in muscular dystrophy with generalized lipodystrophy. *J. Clin. Invest.* **119**, 2623–2633 (2009). doi: 10.1172/JCI38660; pmid: 19726876
75. J.-W. Shin *et al.*, Mechanobiology of bone marrow stem cells: From myosin-II forces to compliance of matrix and nucleus in cell forms and fates. *Differentiation* **2013**, (2013). doi: 10.1016/j.diff.2013.05.001; pmid: 23790394
76. J. S. Chamberlain, J. Metzger, M. Reyes, D. W. Townsend, J. A. Faulkner, Dystrophin-deficient mdx mice display a reduced life span and are susceptible to spontaneous rhabdomyosarcoma. *FASEB J.* **21**, 2195–2204 (2007). doi: 10.1096/fj.06-7353com; pmid: 17360850
77. H. Zhang, F. Burrows, Targeting multiple signal transduction pathways through inhibition of Hsp90. *J. Mol. Med.* **82**, 488–499 (2004). doi: 10.1007/s00109-004-0549-9; pmid: 15168026
78. B. R. Eisenberg, A. M. Kuda, Stereological analysis of mammalian skeletal muscle. II. White vastus muscle of the adult guinea pig. *J. Ultrastruct. Res.* **51**, 176–187 (1975). doi: 10.1016/S0022-5320(75)80146-8; pmid: 1127796
79. J. Hope, Stereological analysis of the ultrastructure of liver parenchymal cells during pregnancy and lactation. *J. Ultrastruct. Res.* **33**, 292–305 (1970). doi: 10.1016/S0022-5320(70)90023-7; pmid: 5494317
80. A. Mattout, A. Biran, E. Meshorer, Global epigenetic changes during somatic cell reprogramming to iPS cells. *J. Mol. Cell Biol.* **3**, 341–350 (2011). doi: 10.1093/jmcb/mjr028; pmid: 22044880
81. W. Wang *et al.*, Rapid and efficient reprogramming of somatic cells to induced pluripotent stem cells by retinoic acid receptor gamma and liver receptor homolog 1. *Proc. Natl. Acad. Sci. U.S.A.* **108**, 18283–18288 (2011). doi: 10.1073/pnas.1100893108; pmid: 21990348
82. K. Beck, B. Brodsky, Supercoiled protein motifs: The collagen triple-helix and the alpha-helical coiled coil. *J. Struct. Biol.* **122**, 17–29 (1998). doi: 10.1006/jsbi.1998.3965; pmid: 9724603
83. B. P. Flynn *et al.*, Mechanical strain stabilizes reconstituted collagen fibrils against enzymatic degradation by mammalian collagenase matrix metalloproteinase 8 (MMP-8). *PLoS ONE* **5**, e12337 (2010). doi: 10.1371/journal.pone.0012337; pmid: 20808784
84. D. K. Shumaker *et al.*, Functions and dysfunctions of the nuclear lamin Ig-fold domain in nuclear assembly, growth, and Emery-Dreifuss muscular dystrophy. *Proc. Natl. Acad. Sci. U.S.A.* **102**, 15494–15499 (2005). doi: 10.1073/pnas.0507612102; pmid: 16227433
85. R. Heald, F. McKeon, Mutations of phosphorylation sites in lamin A that prevent nuclear lamina disassembly in mitosis. *Cell* **61**, 579–589 (1990). doi: 10.1016/0092-8674(90)90470-Y; pmid: 2344612
86. Y. Sawada *et al.*, Force sensing by mechanical extension of the Src family kinase substrate p130Cas. *Cell* **127**, 1015–1026 (2006). doi: 10.1016/j.cell.2006.09.044; pmid: 17129785
87. A. I. Lamond, **Nucleolar isolation protocol** (LamondLab.com, Dundee, Scotland, 2009) http://www.lamondlab.com/f7nucleolarprotocol.htm
88. J. W. Shin, J. Swift, K. R. Spinler, D. E. Discher, Myosin-II inhibition and soft 2D matrix maximize multinucleation and cellular projections typical of platelet-producing megakaryocytes. *Proc. Natl. Acad. Sci. U.S.A.* **108**, 11458–11463 (2011). doi: 10.1073/pnas.1017474108; pmid: 21709232
89. D. Su, L. J. Gudas, Gene expression profiling elucidates a specific role for RARgamma in the retinoic acid-induced differentiation of F9 teratocarcinoma stem cells. *Biochem. Pharmacol.* **75**, 1129–1160 (2008). doi: 10.1016/j.bcp.2007.11.006; pmid: 18164278
90. I. D. Welch, M. F. Cowan, F. Beier, T. M. Underhill, The retinoic acid binding protein CRABP2 is increased in murine models of degenerative joint disease. *Arthritis Res. Ther.* **11**, R14 (2009). doi: 10.1186/ar2604; pmid: 19173746
91. S. L. Yu, L. Levi, R. Siegel, N. Noy, Retinoic acid induces neurogenesis by activating both retinoic acid receptors (RARs) and peroxisome proliferator-activated receptor β/δ (PPARβ/δ). *J. Biol. Chem.* **287**, 42195–42205 (2012). doi: 10.1074/jbc.M112.410381; pmid: 23105114
92. H. A. Barnes, *Handbook of Elementary Rheology* (University of Wales, Institute of Non-Newtonian Fluid Mechanics, Cardiff, 2000).
93. M. Rubinstein, R. Colby, *Polymer Physics* (Oxford University Press, Oxford, 2003).
94. Y. Heo, R. G. Larson, The scaling of zero-shear viscosities of semidilute polymer solutions with concentration. *J. Rheol.* **49**, 1117 (2005). doi: 10.1122/1.1993595

Acknowledgments: We greatly appreciate support from the U.S. National Institutes of Health (NIH R01HL062352, P01DK032094, R01EB007049, and NCATS-8UL1TR000003), the U.S. National Science Foundation (grant 1200834, the University of Pennsylvania's Materials Research Science and Engineering Center, and Nano Science and Engineering Center, Nano/Bio Interface Center), the Human Frontier Science Program (to I.L.I. and D.E.D.), and the Stem Cell Xenograft Core (to A. Secreto, J. Glover, and G. Danet-Desnoyers) and Microarray Cores (P30-DK090969). We thank the Wistar Institute Proteomics Core for assistance with MS and standard data analyses. This work was also supported in part by U.S. NIH grants HL038794 (to D.W.S.) and CA010815 (National Cancer Institute core grant to the Wistar Institute). We thank D. Gilbert (Florida State University, Department of Biological Science), H. Herrmann (Heidelberg, DKFZ), and H. Worman (Columbia University, Department of Medicine), respectively, for GFP-lamin-A, recombinant lamins, and SUN2 plasmids.

Supplementary Materials

www.sciencemag.org/cgi/content/full/341/6149/1240104/DC1
Materials and Methods
Figs. S1 to S16
Tables S1 to S3
References (*95*–*123*)

6 May 2013; accepted 19 July 2013
10.1126/science.1240104

www.sciencemag.org/cgi/content/full/science.1240104/DC1

Supplementary Materials for

Nuclear Lamin-A Scales with Tissue Stiffness and Enhances Matrix-Directed Differentiation

Joe Swift, Irena L. Ivanovska, Amnon Buxboim, Takamasa Harada,
P. C. Dave P. Dingal, Joel Pinter, J. David Pajerowski, Kyle R. Spinler, Jae-Won Shin,
Manorama Tewari, Florian Rehfeldt, David W. Speicher, Dennis E. Discher*

*Corresponding author. E-mail: discher@seas.upenn.edu

Published 30 August 2013 on *Science* Express
DOI: 10.1126/science.1240104

This PDF file includes:

Other Supplementary Material for this manuscript includes the following:
(available at www.sciencemag.org/cgi/content/full/science.1240104/DC1)

Tables S2 and S3 as Excel files

Materials and Methods

Mass Spectrometry Datasets

Table S2 contains MS data processed in Elucidator (Rosetta Biosoftware). Peptides are grouped by "primary protein ID", that is the UniProt or UniParc accession number most commonly associated with peptides from a given protein. Alternative IDs are also listed for each peptide, along with annotations from the SEQUEST database. The integrated ion current, as determined by "peak volume" in Elucidator, is listed for each peptide. Where multiple samples were compared using the "alignment" feature in Elucidator, ion currents for the same peptide in different samples are listed in adjacent columns.

Cell culture

Human-derived alveolar epithelial (A549, CCL-185) and glioblastoma (U251) cell lines as well as mouse-derived myoblast (C2C12, CRL-1772) cell line were cultured according to protocols provided by the supplier (American Type Culture Collection). Fresh human bone marrow HSCs ($CD34^+$ cells, anonymous donors with Institutional Review Board approvals) were obtained from the Xenograft Core Facility at the University of Pennsylvania School of Medicine. Purity of the samples (>98%) was confirmed by flow cytometry with monoclonal antibody against human CD34 conjugated to Phycoerythrin. Primary human mesenchymal stem cells (anonymous donors with Institutional Review Board approvals) were similarly obtained and generally used at low passage (P<4) while cultured in low glucose Dulbecco's modification of Eagle's medium (DMEM, Invitrogen) with 10% fetal bovine serum (FBS, Sigma Aldrich).

Manipulation of lamin levels

siRNAs were purchased from Dharmacon (Thermo Scientific). A549 cells were passaged 24 hours prior to transfection. A complex of siRNA (30 nM siLMNA, 5'-GGUGGUGACGAUCUGGGCU-3' (*95*)) and Lipofectamine 2000 was prepared per manufacturer's instructions and incubated for 24 hrs per dose for up to three treatments in a week (in high glucose DMEM with 10% FBS for U251, F12 with 10% FBS for A549 or in low glucose DMEM with 10% FBS for MSC). Results were compared with those using the same dose of scrambled siRNA. GFP-lamin-A overexpression per Pajerowski *et al.* (*20*) with the lamin-A splice-form, was packaged and delivered by lentivirus for osteogenesis experiments.

Nuclei harvest from cultured cells

Following washing in PBS, cells were suspended in 10 mL ice-cold Buffer A and allowed to swell for 20 min. Cells were then ruptured with 12 strokes in a Dounce homogenizer (staining with trypan blue indicated that 75% of the A549 cells were lysed, although this was harder to ascertain for the MSCs due to cell clumping) and the nuclei pelleted by centrifugation (10 min. at 1000 rpm in a swinging-bucket rotor, 4 °C). The resulting pellet was resuspended in 1 mL Buffer S1 and layered over 1 mL Buffer S3. Centrifugation (10 min at 5000 rpm in a swinging-bucket rotor, 4 °C) yielded a small, loose, white pellet that was suspended in Nuclei Wash Buffer (0.2 M sucrose, 10 mM HEPES, 1 mM $MgCl_2$, 0.1% PIC).

Gel electrophoresis and immunoblotting

SDS-PAGE gels (NuPAGE 4-12% Bis-Tris, Invitrogen) were loaded with 2 – 14 μL of lysate per lane. For immunoblotting, each sample was loaded multiple times (3 to 5) with different volumes in order to establish a linear response. Additionally, load volumes were adjusted to give a readable response by immunoblotting whilst avoiding overloading and smearing, diluting the lysates with additional 1x NuPAGE LDS buffer if necessary. Gel electrophoresis was run for 10 min at 100 V and 1 hr at 160 V.

After blotting on a polyvinylidene fluoride membrane with an iBlot Gel Transfer Device (Invitrogen), the membrane was blocked with 5% non-fat dry milk solution. Membranes were incubated with primary antibody against B-type lamins (sc-6217, raised in goat, Santa Cruz Biotechnology; used at 1000-fold dilution) at 4 °C overnight. After washing, the membrane was incubated with 2000-fold diluted anti-goat HRP-conjugated IgG (Abcam), at room temperature for 1 hour. The blot was developed with ChromoSensor (GenScript) for 3 minutes at room temperature. Blot images were obtained using a Hewlett-Packard Scanjet 4850. Following stripping with Restore buffer (Thermo Scientific), the process was repeated with a lamin-A,C primary antibody (#2032, raised in rabbit, Cell Signaling Technology; used at 1000-fold dilution) in conjunction with an anti-rabbit HRP-conjugated IgG (GE Healthcare). Densitometry was performed using ImageJ (version 1.45, NIH). Igor Pro (version 6.22, WaveMetrics Inc.) was used for linear regression and associated error estimation. Immunoblot measurements were made with the following numbers of animal replicates: fat, lung, liver, kidney, muscle ($n = 1$); heart, cartilage, femur, skull ($n = 2$); brain ($n = 3$) (Fig. S5).

Immunostaining and cell imaging

Cells were rinsed with PBS, fixed with 4% paraformaldehyde (Fisher) for 20 min, washed twice with PBS and permeabilized with 0.5% Triton-X (Fisher) in PBS for 20 min. Cells were then treated with 5% BSA (blocking solution) for 1 hr. Following two additional PBS washes, samples were incubated overnight with primary antibodies at 1:300 dilution in 2% BSA solution with gentle agitation at 4 °C. The primary antibodies used were: lamin-A/C mouse monoclonal sc-7292, lamin-B goat polyclonal sc-6217, YAP mouse monoclonal sc-101199 (Santa Cruz Biotechnology); RAR-gamma rabbit polyclonal PA5-21463 (Thermo Scientific). Cells were washed twice in PBS and incubated with the corresponding secondary antibodies at 1:500 dilution for 45 minutes (Alexa Fluor 546, 594 and 647 nm; Invitrogen). Adherent cells on gels or glass coverslips were mounted with mounting media (Invitrogen ProLong Gold Antifade Reagent) or sometimes imaged with fixation and no mounting. Images of adherent cells were taken with an Olympus IX71 microscope in epifluorescence or else a confocal laser scanning mode with the 488 nm and 543 nm laser lines, for GFP and Alexa 546 dyes, respectively. Such excitation and sequential scanning data acquisition minimizes crosstalk between the two channels compared to the Hg arc illumination in epifluorescence in which case longer wavelength 647 nm dye was used. Images were taken with either a 20x 0.4 NA air objective (LCAch), 60x 1.25 NA oil objective (UPlan FI) or a 150x 1.45 NA oil objective (TIRFM). All images for quantitative analysis in a given experiment were taken under the same imaging conditions. Images taken with the 20x objective were based on the integrated intensity. For confocal imaging, images were captured with a 60x 1.25 NA oil objective (UPlan FI) using consecutive z-scans at 0.5 µm steps; with MSCs on stiff matrices, nuclei appeared sufficiently flattened, that such imaging conditions were unable to distinguish between lamin localization to the nucleoplasm or to the top or bottom of the nuclear envelope. Fluorescence intensity was measured along a cross-section in a z-stack representing the mid-plane of the nucleus using Image J and the ratio between the mean intensities inside and outside the nucleus was taken. When cells had multiple labels, as was the case for GFP-lamin-A expressing cells that were also immunostained for YAP1 or RARG, additional images were taken with single label samples. This demonstrated that crosstalk between different label channels was <5-10% of image intensity in the primary color channel and no more than 2-fold above background, which ruled out crosstalk artifacts.

Correlation and bioinformatics analysis

Human and mouse tissue transcript data (1.0 ST datasets) is available from: http://www.affymetrix.com/support/technical/sample_data/exon_array_data.affx. Transcriptomes from

whole genome microarrays (Affymetrix, Santa Clara, CA) were for mouse adult tissue: brain, heart, kidney, liver, lung, ovary, muscle, spleen, testis and thymus (*n = 3*). Human adult tissues were: brain, breast, heart, kidney, liver, pancreas, prostate, muscle, spleen, testis and thyroid (*n = 3*). Total RNA was extracted from human MSCs using Trizol and isolated by RNeasy (Qiagen) according to manufacturer's protocol. Total RNA was amplified and converted to cDNA using WT-Ovation Pico kit (NuGen) and converted to ST-cDNA, fragmented and biotin-functionalized using WT-Ovation Exon Module (NuGen). Hybridization cocktails were prepared at 45.4, 15.1 and 7.6 ng/μL ST-cDNA and mixed with Eukaryotic Hybridization Controls (GeneChip) at proportional concentrations. Each Sample was interrogated by sequential hybridization, rinse and scan cycles on a single Human Gene 1.0 ST DNA microarray (Affymetrix, Santa Clara, CA), from low to high concentration, and followed by two rinse-scan cycles in which no sample was added. In each experiment the scanned intensities that were obtained from all samples, five scans per array, were mutually RMA-summarized to transcription clusters gene levels so that the average and standard deviation (STD) could be calculated for each gene. Data for genes presented in the paper is contained in Table S3.

Xenograft tumor processing

Xenografts in flank and brain sites were generated per previous methods in either nu/nu mice (*96*) or NSG mice (*97*). All animal experiments were planned and performed according to IACUC protocols. After harvesting, tumor tissues were quickly weighed, snap-frozen with liquid nitrogen and homogenized. For 40 mg tissue, 1 mL of RIPA buffer was added on ice. Tissues were sonicated for 1.5 min and incubated on rocker at 4 degree for 2 hours. Samples were centrifuged (13k rpm for 20 min) and the supernatant collected. Protein concentration of lysates was measured by standard BCA assay (Thermo) and lysate containing 25 μg protein was loaded to each lane of Bis-Tris (4-12%) gel (Invitrogen). After electrophoresis (10 min at 100 V + 20 min at 160 V), the gel was stained with Coomassie brilliant blue dye. Samples were prepared for MS as described above. For tissue stiffness studies, A549 or U251 cells were injected into the flank, and after 28 days of tumor growth, mice were sacrificed and tumor and normal subcutaneous tissue was excised for study within ~2 hrs.

Micropipette aspiration of murine tissue

For untreated samples, tissue was immediately aspirated. Collagenase treated samples were incubated at 37°C for 10 minutes in the presence of 0.1 mg/mL collagenase (Sigma) and aspirated in the presence of enzyme. Capillary tubes of 1.0 mm inner diameter (World Precision Instruments) were pulled into micropipettes using a Flaming-Brown Micropipette Puller (Sutter Instrument) and cut further using a deFonbrune-type microforge (Vibratome). The average micropipette diameter was around 15 μm. A micropipette was attached to a dual-stage water manometer with reservoirs of adjustable height. Suction was applied by syringe, and the corresponding pressure was measured by a pressure transducer (Validyne) calibrated by a mercury U-tube manometer. Pressures for different experiments ranged from 1 to 20 kPa. Images were acquired using a Nikon Eclipse TE300 inverted microscope using a 20x objective and a Cascade CCD camera (Roper Scientific). Imaging was captured over 30 seconds of aspiration. Further image analysis was done using ImageJ. Stiffness was calculated per (*98*).

Polyacrylamide gel preparation

Polyacrylamide hydrogels of 0.3 kPa to 40 kPa stiffness were prepared as described previously (*99*). Gels for cell culture were further coated with type-I rat tail collagen or freshly prepared human fibronectin (BD Biosciences) as follows: Sulfo-Sanpah (Fisher Scientific) was dissolved in 50 mM, pH 8 HEPES to a concentration of 0.5 mg/ml and pipetted to form a complete coverage of the gels. Gels

were placed inside a UV chamber and illuminated for 10 min by 365 nm illumination. To minimize collagen fiber formation, collagen was first mixed in equal volume of 4 °C 0.1 M acetic acid (Fisher Scientific) and then diluted in 4 °C 50 mM, pH 8 HEPES to a final concentration of 0.2 mg/ml. Protein was incubated on the gels while on a shaker overnight at 37 °C. Prior to seeding cells, gels were UV-sterilized in cell culture hood for two hours. Gels were kept hydrated in PBS or deionized water during all preparation steps.

Lamin-A Ig domain purification

Plasmids containing WT lamin-A Ig domain in the pGEX-T4-1 expression vector were a gift from H. Worman. After transformation into BL21 E. Coli, the plasmids were induced with isopropyl β-D-1-thiogalactopyranoside (IPTG) to produce a fusion protein of lamin-A Ig and glutathione S-transferase (GST) with a thrombin cleavage site in-between. Protein was separated from cell lysates by binding to glutathione Sepharose 4B matrix (GE Healthcare Bio-sciences), and Ig was cleaved off the matrix by thrombin. Thrombin was removed from solution by binding to benzamidine Sepharose 4 Fast Flow matrix (GE healthcare Bio-sciences). Residual DNA was removed from solution by precipitation with 20 mM $MnCl_2$ and buffer was exchanged to PBS. The fold state of the recombinant Ig domain was determined over a range of temperatures and urea denaturant concentrations using a tryptophan fluorescence assay (Bruker) or by monitoring signal in circular dichroism at 230 nm (Applied Photophysics).

Cysteine labeling kinetics of lamin-A Ig domain

Purified lamin-A Ig domain (20 μM in PBS/urea) was labeled with 150 μM monobromobimane (mBBr, Invitrogen). Aliquots were taken at 5, 10, 20, and 40 min then quenched with 2.5 mM glutathione. 0 min samples were unlabeled Ig domain with glutathione. Reaction buffer was exchanged back to PBS by centrifugal filtration with Amicon Ultra 3,000 MWCO filters (Millipore). Samples were then digested with trypsin (Promega) overnight. 20 μL of digested sample was separated by HPLC (Shimadzu) with a Restek Viva C18 5μm 150 x 4.6 mm column. The extent of labeling was assessed by integration of the conjugated mBBr absorption peak at 396nm.

Immunoprecipitation

In order to maximize signal-to-noise and peptide coverage, immunoprecipitation (IP) was performed to enrich target proteins prior to analysis by mass spectrometry. Cell pellets were resuspended in ice-cold NP-40 lysis buffer (1% NP-40, 150 mM NaCl, 50 mM Tris, pH 8, 0.1% PIC; 100 μL / 1 million cells) and sonicated on ice (probe sonicator on low power setting: 1s x 10 x 5 pulses). Protein A Dynabeads were washed twice with 0.02% NP-40 in PBS (Bead Wash Buffer), incubated with antibody for 1 hr at 4 °C with gentle agitation (primary antibodies used for IP: lamin-A/C mouse monoclonal sc-7292 and YAP mouse monoclonal sc-101199, Santa Cruz Biotechnology; GFP rabbit polyclonal ab290, Abcam; RAR-gamma rabbit polyclonal PA5-21463, Thermo Scientific) and washed two more times in Bead Wash Buffer. In RARG and YAP experiments, the cell lysate was pre-cleared with antibody-free beads that were subsequently used as a control sample in order to identify non-specific binding. Cell lysates and antibody-coated beads were gently agitated at 4 °C for 2 hrs, then the beads were washed three times with ice-cold Bead Wash Buffer to remove proteins bound with low affinity. Beads were then resuspended in 20 μL LDS buffer with 1% BME and heated to 80 °C for 10 min. Samples were separated by SDS-PAGE and subsequently prepared for analysis by mass spectrometry.

Cell fate influenced by lamin levels and matrix elasticity

For adipogenic lineage, MSCs were plated (5000 cells per mm^2) on 0.3 kPa and 40 kPa polyacrylamide gels coated with human fibronectin at a concentration of 0.2 mg/ml (BD Biosciences #354008) and gel stiffnesses were checked after coating using AFM. Fibronectin was used because the MS results showed such tissue has relatively low collagen content (Fig. 1G). Cells were seeded on gels in DMEM media supplemented with 10% FBS and incubated overnight. For knockdown, cells were treated with Lipofectamine 2000 / siLMNA complex, prepared according to the manufacturer's protocol. Media was replaced after 12 hours, cells were washed with DPBS (Invitrogen) and adipogenic induction media (BMDS) was added. After 72 hours, the adipogenic media was removed and replaced with DMEM and siLMNA and the cycle repeated. The knockdown/induction procedure was performed three times consecutively. Cells were fixed and the fraction of oil-drop positive cells established by oil-red staining. Lamin-A levels were assessed by immunofluorescence. For osteogenic lineage: MSCs were transduced (or not) with lentivirus encoding GFP-lamin-A. Cells were transduced at MOI 50 and evaluated for survival and proliferation. The fraction of GFP-lamin-A positive cells prior to experiment was ~ 50%. Cells were seeded sparsely on 0.3 kPa and 40 kPa gels coated with monomeric collagen-1, with ~ 50% more cells on 0.3 kPa gels to achieve similar substrate coverage at the beginning of the experiment. After overnight culture, cells on soft gels were imaged in phase contrast and seen to be small and round versus large and spread on stiff gels. Cultures were then treated with osteogenic induction media for 1 week. Media was changed every 2- 3 days. Cells were fixed and immediately stained for alkaline phosphatase (ALP) activity. ALP activity was evaluated based on digitalized bright field images (10-15 images across gels) and quantified by fitting a double Gaussian function to the intensity distribution. Lamin-A levels were assessed by immunofluorescence as described above.

Promoter analysis

Promoter sequences were analyzed with the Genomatix software suite (Genomatix Software GmbH (*100*)). Mouse and human promoters (Eldorado database, December 2012) were searched against transcription factor matrices (version 9.0) using the Gene2Promoter tool. Transcription factor annotations were then examined using the MatInspector tool.

Methylation states of CpG islands

Cells were flash frozen and sent to Qiagen (Frederick, MD) for methyl-qPCR analysis. Methylation was measured in CpG islands in the promoter regions of human *LMNA*, *LMNB1* and *LMNB2*. Measurements were made with biological duplicates and technical triplicates.

Activation and inhibition of the retinoic acid pathway

Cultured cells were treated with either control solvent (0.15% EtOH, 0.15% DMSO in media with 10% FBS), solvent with all-trans retinoic acid (RA, 1 μM, Fisher Scientific) or solvent with inhibitor (AGN-193109, 1 μM, Santa Cruz Biotechnology).

Lamin-promoter GFP-reporter transfection and nucleofection

Reporter constructs (lamin-A, lamin-B and a truncated lamin-A, "Δ-*LMNA*") were purchased from Genecopoeia (Rockwille). A549 and U251 cells were transfected with LF2k (Invitrogen) as described in the manufacturer's instructions; MSCs were nucleofected with the Human MSC Nucleofector Kit (Lonza), used according to the manufacturer's directions. Reporter construct activity was initially checked by fluorescence microscopy (Fig. 5C) and quantified by FACS (Fig. 5D, see following protocol). For Fig. 5E, passage 4 MSCs obtained from a human female donor, age 28, were nucleofected

with wild type *LMNA* and Δ-*LMNA* promoters. Cells were cultured for two days, harvested and seeded on 0.3 kPa and 40 kPa UV-sterilized, rat-tail type-I collagen-coated polyacrylamide gels covalently attached to 18 mm square glass cover slips (*99*) and placed inside NUNC 2-chamber Lab□Tek™ II chambered coverglasses (Thermo Scientific). Samples were placed inside a Stagetop environmental chamber, maintained at 37 °C and 5% CO_2, and mounted on an Olympus IX81-DSU spinning disk confocal microscope. Promoter activity of randomly selected cells (n = 20 - 25) was evaluated after 48 hrs in culture on soft and stiff gels by epifluorescence. Flow cytometry analysis was also used to measure promoter activity: following transfection, media was replaced after four hours with appropriate cell growth media plus RA, AGN or solvent. After 48 hrs treatment, cells were harvested by trypsinization, fixed in 1.5% para-formaldehyde for ten minutes and resuspended in 2% FBS/PBS. Fluorescence signal was measured in the FITC channel with a FACS Vantage machine (Becton Dickinson), with gating for cell aggregates.

Micropipette aspiration of nuclei

As adapted from (*20, 98*), cells were treated with 0.2 μg/ml Latrunculin A (Sigma) for 1 hour at 37°C, detached with trypsin/EDTA, centrifuged and resuspended in aspiration buffer of 135 mM NaCl, 5mM KCl, 5 mM HEPES, 1.8 mM $CaCl_2$, 2 mM $MgCl_2$, 2% BSA, 1:3000 propidium iodide (Molecular Probes). Nuclei were stained with Hoechst 33342 (Molecular Probes). Nuclear compliance was measured as membrane extension under negative pressure inside a micropipette. Epifluorescence imaging was done with a Nikon TE300 inverted microscope coupled with a digital CCD camera (Roper Scientific, Tuscan AZ), using a 60x oil immersion objective.

A Correlation of nuclear proteins with tissue microelastcity (*E*) in mouse tissue

				Protein level in nuclei isolated from tissue						Correlation with tissue microelasticity, *E*		
Protein Name (Gene)	**<R-squared>**	**<PRF>**	**Total Pep**	**Brain**	**Liver**	**Fat**	**Lung**	**Muscle**	**Heart**	**Correlation**	**R-squared**	**Gradient**
Lamin A/C overlap (Lmna)	0.96	38.2	43	70 ± 1	163 ± 14	316 ± 31	610 ± 69	379 ± 32	535 ± 57	0.94*	0.88*	0.7*
SUN domain-containing protein 2 (Sun2)	0.50	3.0	6	41 ± 1	52 ± 4	258 ± 25	229 ± 26	1716 ± 143	887 ± 94	0.93	0.86	1.0
Torsin-1A-interacting protein 1 (Tor1aip1)	0.92	4.5	8	60 ± 1	231 ± 19	165 ± 16	848 ± 96	626 ± 52	684 ± 72	0.91	0.82	0.6
Nesprin-1 (Syne1)	-2.54	2.8	3	39 ± 1	116 ± 10	177 ± 17	200 ± 23	3826 ± 319	687 ± 73	0.86	0.74	0.9
Polymerase I and transcript release factor (Ptrf)	0.55	8.5	13	2 ± 0	12 ± 1	755 ± 73	1187 ± 134	120 ± 10	1274 ± 135	0.83	0.68	1.5
Transitional endoplasmic reticulum ATPase (Vcp)	0.83	9.0	14	46 ± 1	477 ± 40	250 ± 24	240 ± 27	375 ± 31	839 ± 89	0.79	0.62	0.5
Ahnak protein (Ahnak)	0.79	15.0	30	75 ± 1	236 ± 20	214 ± 21	3632 ± 411	1677 ± 140	563 ± 60	0.76	0.57	0.8
Lamin B1 (Lmnb1)	0.96	25.8	32	99 ± 3	62 ± 5	164 ± 15	243 ± 27	145 ± 15	131 ± 13	0.72*	0.52*	0.2*
Pyruvate kinase isozymes M1/M2 (Pkm2)	0.57	5.3	10	63 ± 1	3 ± 0	62 ± 6	33 ± 4	383 ± 32	627 ± 66	0.62	0.38	0.8
Non-POU domain-containing octamer-binding protein (Nono)	0.88	10.7	16	98 ± 2	96 ± 7	72 ± 9	96 ± 11	222 ± 23	123 ± 16	0.51	0.26	0.1
Nucleolar protein 58 (Nop58)	0.87	7.5	12	93 ± 2	616 ± 51	256 ± 25	236 ± 27	825 ± 69	209 ± 22	0.43	0.19	0.2
ATP-dependent RNA helicase DDX3X/Y overlap (Ddx3x/y)	0.90	6.0	10	97 ± 2	69 ± 6	65 ± 7	56 ± 7	187 ± 17	129 ± 14	0.41	0.17	0.1
Nucleolin (Ncl)	0.95	11.8	18	94 ± 2	732 ± 61	505 ± 49	467 ± 53	581 ± 48	221 ± 23	0.39	0.15	0.2
DEAD (Asp-Glu-Ala-Asp) box polypeptide 17 (Ddx17)	0.45	7.7	11	102 ± 2	103 ± 7	51 ± 4	60 ± 5	649 ± 60	138 ± 25	0.39	0.15	0.2
Lamin B2 (Lmnb2)	0.92	23.2	33	102 ± 3	70 ± 5	71 ± 8	91 ± 12	46 ± 5	91 ± 11	0.37*	0.14*	0.0*
Paraspeckle component 1 (Pspc1)	0.57	4.5	8	105 ± 2	73 ± 6	61 ± 6	142 ± 16	259 ± 22	73 ± 8	0.29	0.08	0.1
Selenium-binding protein 2 (Selenbp2)	0.95	3.2	7	73 ± 1	6010 ± 500	185 ± 18	831 ± 94	801 ± 67	453 ± 48	0.25	0.06	0.3
Staphylococcal nuclease domain-containing protein 1 (Snd1)	0.74	4.2	9	80 ± 1	4946 ± 412	627 ± 61	371 ± 42	248 ± 21	1110 ± 118	0.21	0.04	0.2
Heterogeneous nuclear ribonucleoprotein R (Hnrnpr)	0.80	8.2	12	103 ± 2	9 ± 1	67 ± 6	22 ± 3	67 ± 6	77 ± 8	0.09	0.01	0.1
Nucleolar protein 56 (Nop56)	0.65	9.7	15	98 ± 2	532 ± 44	236 ± 23	236 ± 29	158 ± 21	183 ± 22	0.07	0.00	0.0
Splicing factor 3A subunit 3 (Sf3a3)	0.59	4.7	7	101 ± 2	159 ± 13	108 ± 11	153 ± 16	150 ± 15	91 ± 9	0.05	0.00	0.0
Heterochromatin protein 1-binding protein 3 (Hp1bp3)	0.61	11.3	16	105 ± 2	47 ± 4	72 ± 7	176 ± 20	92 ± 7	64 ± 8	0.04	0.00	0.0
Polypyrimidine tract-binding protein 1 (Ptbp1)	0.83	3.3	5	80 ± 1	1272 ± 106	2611 ± 252	111 ± 13	75 ± 6	425 ± 45	-0.04	0.00	0.0
Splicing factor, proline- and glutamine-rich (Sfpq)	0.94	13.5	19	100 ± 2	128 ± 12	112 ± 11	175 ± 18	53 ± 4	123 ± 12	-0.14	0.02	0.0
Splicing factor U2AF 65 kDa subunit (U2af2)	0.60	4.0	6	104 ± 2	115 ± 10	110 ± 11	37 ± 4	198 ± 17	66 ± 7	-0.15	0.02	-0.1
Methyl-CpG-binding protein 2 (Mecp2)	0.78	14.3	22	107 ± 2	4 ± 0	55 ± 5	65 ± 7	15 ± 1	34 ± 4	-0.15	0.02	-0.1
Myelin expression factor 2 (Myef2)	0.65	8.3	15	108 ± 2	14 ± 1	13 ± 1	18 ± 2	57 ± 5	34 ± 4	-0.20	0.04	-0.1
DNA topoisomerase 1 (Top1)	0.86	5.3	8	98 ± 2	267 ± 22	144 ± 14	334 ± 38	137 ± 11	37 ± 4	-0.27	0.08	-0.1
Heterogeneous nuclear ribonucleoprotein A3 (Hnrnpa3)	0.87	5.0	8	109 ± 2	9 ± 1	153 ± 15	42 ± 5	54 ± 4	15 ± 2	-0.28	0.08	-0.2
Heterogeneous nuclear ribonucleoprotein L (Hnrnpl)	0.81	10.2	17	104 ± 3	16 ± 1	94 ± 8	26 ± 3	30 ± 2	50 ± 6	-0.30	0.09	-0.2
DEAD (Asp-Glu-Ala-Asp) box polypeptide 5 (Ddx5)	0.69	16.5	23	105 ± 2	112 ± 11	79 ± 7	61 ± 7	145 ± 8	61 ± 7	-0.31	0.10	-0.1
Thyroid hormone receptor-associated protein 3 (Thrap3)	0.40	3.7	6	105 ± 2	163 ± 14	132 ± 12	133 ± 14	152 ± 13	55 ± 4	-0.33	0.11	-0.1
Heterogeneous nuclear ribonucleoprotein A2/B1 (Hnrnpa2b1)	0.84	5.2	8	109 ± 2	4 ± 0	48 ± 5	22 ± 2	60 ± 5	3 ± 0	-0.39	0.15	-0.4
Heterogeneous nuclear ribonucleoprotein K (Hnrnpk)	0.87	11.8	18	109 ± 2	19 ± 2	49 ± 5	20 ± 2	56 ± 5	31 ± 3	-0.39	0.15	-0.2
Heterogeneous nuclear ribonucleoprotein Q (Hnrnpq)	0.75	4.8	8	106 ± 2	26 ± 2	157 ± 15	26 ± 3	26 ± 2	52 ± 5	-0.41	0.17	-0.2
Heterogeneous nuclear ribonucleoprotein M (Hnrnpm)	0.89	18.0	25	102 ± 2	153 ± 12	156 ± 15	142 ± 18	50 ± 4	93 ± 10	-0.42	0.18	-0.1
Core histone macro-H2A.1 (H2afy)	0.41	3.5	6	110 ± 2	13 ± 1	7 ± 1	24 ± 3	35 ± 3	13 ± 1	-0.46	0.21	-0.3
PC4 and SFRS1-interacting protein (Psip1)	0.87	7.5	13	105 ± 2	4 ± 0	4 ± 0	16 ± 2	21 ± 2	4 ± 0	-0.46	0.21	-0.4
Heterogeneous nuclear ribonucleoprotein U-like 2 (HHnrnpul2)	0.87	8.2	13	109 ± 2	73 ± 6	380 ± 37	44 ± 5	40 ± 3	32 ± 3	-0.53	0.28	-0.3
Heterogenous nuclear ribonucleoprotein U (Hnrnpu)	0.46	5.2	8	103 ± 2	128 ± 11	351 ± 34	88 ± 10	64 ± 5	28 ± 3	-0.54	0.29	-0.3
RNA-binding protein 39 (Rbm39)	0.89	4.2	7	104 ± 2	122 ± 10	34 ± 3	116 ± 13	48 ± 4	48 ± 5	-0.54	0.29	-0.2
Pre-mRNA-processing factor 19 (Prpf19)	0.79	5.7	10	104 ± 2	137 ± 13	113 ± 10	143 ± 22	52 ± 5	74 ± 8	-0.54	0.29	-0.1
Matrin-3 (Matr3)	0.85	4.8	8	107 ± 2	45 ± 4	45 ± 4	16 ± 2	75 ± 6	11 ± 1	-0.65	0.43	-0.4
RNA-binding protein FUS (Fus)	0.63	3.3	6	109 ± 2	23 ± 2	47 ± 5	17 ± 2	4 ± 0	27 ± 3	-0.71	0.50	-0.5
Serine/arginine-rich splicing factor 4 (Srsf4)	0.70	2.8	3	109 ± 2	90 ± 8	71 ± 7	127 ± 14	18 ± 1	17 ± 2	-0.75	0.56	-0.5

Median ion current <brain, heart> Normalization

*with additional tissues: kidney, cartilage, skull, femur

B Linkers between nucleus and cytoskeleton (LINC complex): nuclear protein scales with *E* (mRNA does not)

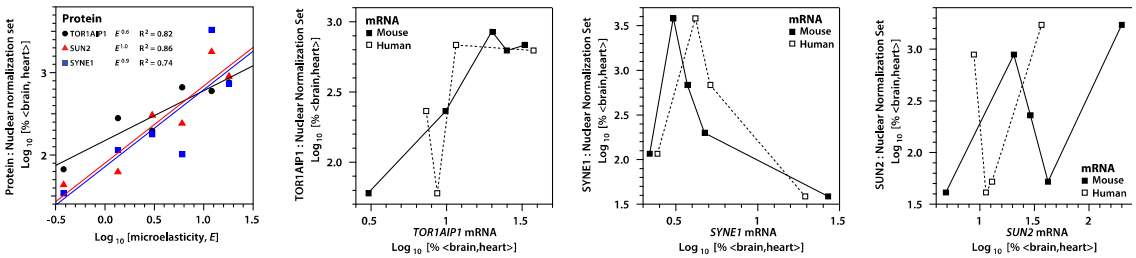

Fig. S1. Proteomic profiling of nuclei isolated from mouse tissue by quantitative, label-free mass spectrometry reveals lamin-A correlation with tissue microelasticity, *E*. (A) The R^2 value refers to the quality of the peptide : peptide ratios between control and sample datasets and the <PRF> ("peptide ratio fingerprint") refers to the mean number of peptides selected for quantification (see Methods, (*88*)). Protein quantities are indicated relative to an average of brain and heart (± SEM from technical triplicates). The color of the protein name indicates the median <brain, heart> ion current, an approximate measure of concentration. Proteins highlighted in blue were identified as part of a normalization peptide set common to and invariable in all samples. The right-hand columns show strength of correlation and coupling with tissue microelasticity (correlations of LMNA, LMNB1 and LMNB2 combine additional data from whole tissue preparations of kidney, cartilage, skull and femur). (B) For the non-lamin nuclear envelope proteins that were detected, nuclear protein levels are plotted versus microelasticity, showing good correlation. However, given that transcript levels relate to total expression, nuclear protein levels did not correlate with total expression, suggesting significant cytoplasmic fractions: *TOR1AIP1* is torsin-1A-interacting protein 1; *SYNE1* is nesprin-1; *SUN2* is sun-domain containing protein 2.

A Correlation of protein and mRNA with microelasticity (*E*) in mouse tissue

				MS Analysis Scores		Protein Correlation with Lamin-A			mRNA Correlation with *LMNA*				
Name (gene)	whole tissue	nucL frac.	Notes	Min. <R-Squared>	Min. <PRF>	Pearson	R-squared	Protein Power Law With *E*	<Gene Intensity> in Hu Heart	Pearson (Hu)	<Gene Intensity> in Ms Heart	Pearson (Ms)	<mRNA Power Law With *E*
Lamin-A/C overlap (Lmna)	•	o	Intermediate filament	0.92	24.8	1.000	1.000	**0.7**	8.024	1.00	9.848	1.00	**0.3**
Trans. growth factor-beta-induced ig-h3 (Tgfbi)	•	o	ECM	0.72	3.7	0.944	0.891	**0.9**	9.319	0.70	9.340	0.73	**0.4**
Collagen alpha-1(III) chain (Col3a1)	•	o	ECM	0.85	12.0	0.971	0.943	**1.5**	7.955	0.65	10.556	0.70	**0.5**
Collagen alpha-1(V) chain (Col5a1)	•	o	ECM	0.00	2.0	0.958	0.917	**1.3**	6.444	0.67	8.414	0.72	**0.2**
Collagen alpha-3(VI) chain (Col6a3)	•	o	ECM	0.87	35.8	0.905	0.819	**1.1**	8.599	0.74	9.170	0.70	**0.6**
Collagen alpha-1(VI) chain (Col6a1)	•	o	ECM	0.61	9.6	0.954	0.911	**1.4**	8.617	0.76	9.264	0.54	**0.4**
Collagen alpha-2(I) chain (Col1a2)	•	o	ECM	0.89	28.9	0.943	0.889	**1.5**	8.474	0.60	10.372	0.67	**0.5**
Collagen alpha-1(I) chain (Col1a1)	•	o	ECM	0.91	34.9	0.927	0.859	**1.5**	8.134	0.66	10.214	0.61	**0.4**
Periostin (Postn)	•	o	ECM	0.89	8.6	0.847	0.717	**1.2**	8.317	0.70	10.192	0.69	**0.7**
Collagen alpha-2(V) chain (Col5a2)	•	o	ECM	0.49	3.0	0.906	0.820	**1.3**	6.502	0.49	7.398	0.77	**0.2**
Collagen alpha-2(VI) chain (Col6a2)	•	o	ECM	0.74	5.4	0.862	0.744	**1.2**	8.577	0.77	9.791	0.57	**0.4**
Lumican (Lum)	•	o	ECM	0.51	3.9	0.947	0.898	**1.2**	8.054	0.61	10.482	0.55	**0.7**
Prolargin (Prelp)	•	o	ECM	0.91	7.8	0.861	0.741	**1.0**	8.316	0.50	10.972	0.76	**0.3**
Gelsolin (Gsn)	•	o	Cytoskeleton	0.74	5.4	0.823	0.677	**0.7**	10.834	0.59	12.657	0.62	**0.5**
Decorin (Dcn)	•	o	ECM	0.86	3.8	0.850	0.723	**1.1**	11.128	0.48	13.064	0.55	**0.5**
Nidogen-1 (Nid1)	•	o	ECM	0.81	4.0	0.531	0.282	**0.6**	7.985	0.75	10.483	0.88	**0.4**
Laminin subunit gamma-1 (Lamc1)	•	o	ECM	0.89	6.2	0.515	0.265	**0.5**	9.053	0.79	11.135	0.75	**0.5**
Vimentin (Vim)	•	o	Intermediate filament	0.92	5.4	0.701	0.492	**0.7**	9.393	0.48	12.557	0.66	**0.3**
Collagen alpha-1(XII) chain (Col12a1)	•	o	ECM	0.68	8.9	0.768	0.591	**1.1**	7.307	0.76	6.495	0.24	**0.3**
Myomesin-1 (Myom1)	•	o	Cytoskeleton	0.53	13.6	0.641	0.411	**1.4**	10.799	0.60	12.907	0.62	**1.2**
Filamin-A (Flna)	•	o	Cytoskeleton	0.84	32.2	0.605	0.366	**0.4**	9.210	0.61	10.525	0.63	**0.4**
Moesin (Msn)	•	o	Cytoskeleton	0.88	13.4	0.570	0.325	**0.3**	10.437	0.56	11.551	0.63	**0.3**
Myosin-1 (Myh1)	•	o	Cytoskeleton	0.87	18.5	0.843	0.710	**1.6**	2.841	0.37	5.495	0.27	**0.7**
Titin (Ttn)	•	o	Cytoskeleton	0.77	118.4	0.644	0.415	**1.3**	11.810	0.57	12.269	0.44	**1.5**
Filamin-C (Flnc)	•	o	Cytoskeleton	0.56	5.2	0.629	0.396	**1.0**	11.692	0.55	11.266	0.49	**1.1**
Cytoskeleton-associated protein 4 (Ckap4)	•	o	Cytoskeleton	0.84	6.6	0.640	0.410	**0.5**	8.460	0.62	9.344	0.29	**0.1**
Vinculin (Vcl)	•	o	Cytoskeleton	0.80	16.4	0.228	0.052	**0.2**	8.403	0.83	10.918	0.90	**0.5**
Myomesin-2 (Myom2)	•	o	Cytoskeleton	0.71	20.1	0.632	0.399	**1.3**	10.219	0.47	12.222	0.43	**1.2**
Myosin-4 (Myh4)	•	o	Cytoskeleton	0.78	18.6	0.710	0.505	**1.4**	3.159	0.48	5.576	0.24	**0.4**
Laminin subunit beta-2 (Lamb2)	•	o	ECM	0.89	6.8	0.345	0.119	**0.4**	9.372	0.84	11.538	0.59	**0.5**
SUN domain-containing protein 2 (Sun2)	o	•	Nucleus	0.86	3.6	0.765	0.585	**0.9**	8.274	0.20	9.251	0.38	**0.1**
Torsin-1A-interacting protein 1 (Tor1aip1)	o	•	Nucleus	0.93	6.6	0.894	0.799	**0.6**	8.289	0.23	9.168	0.06	**0.2**
Myosin-7 (Myh7)	•	o	Cytoskeleton	0.81	5.0	0.504	0.254	**1.0**	11.931	0.57	10.387	0.43	**1.1**
Myosin-2 (Myh2)	•	o	Cytoskeleton	0.70	8.4	0.697	0.486	**1.7**	5.776	0.36	6.160	0.24	**0.6**
Caldesmon (Cald1)	•	o	Cytoskeleton	0.89	6.6	0.426	0.181	**0.2**	8.410	0.39	7.840	0.73	**0.1**
Talin-1 (Tln1)	•	o	Cytoskeleton	0.87	19.3	0.250	0.063	**0.1**	9.022	0.74	10.921	0.67	**0.3**
Nebulin (Neb)	•	o	Cytoskeleton	0.69	23.8	0.623	0.388	**1.2**	5.650	0.37	6.461	0.29	**0.7**
Alpha-actinin-2 (Actn2)	•	o	Cytoskeleton	0.55	17.5	0.612	0.375	**1.3**	11.098	0.36	13.003	0.31	**1.1**
Myosin-6 (Myh6)	•	o	Cytoskeleton	0.79	40.4	0.470	0.221	**1.2**	9.972	0.55	13.483	0.35	**1.0**
Plectin (Plec)	•	o	Cytoskeleton	0.89	50.1	0.542	0.294	**0.5**	7.387	0.57	9.850	0.17	**0.2**
Keratin, type II cytoskeletal 2 epidermal (Krt2)	•	o	Intermediate filament	0.88	17.6	0.596	0.355	**0.9**	4.188	0.44	5.491	0.13	**0.0**
Alpha-actinin-3 (Actn3)	•	o	Cytoskeleton	0.77	13.6	0.597	0.357	**1.2**	5.101	0.44	6.747	0.04	**0.5**
Plastin-2 (Lcp1)	•	o	Cytoskeleton	0.90	13.4	0.449	0.201	**0.2**	8.928	0.23	10.115	0.51	**0.2**
Collagen alpha-1(XI) chain (Col11a1)	•	o	ECM	0.66	3.0	0.816	0.665	**0.8**	4.871	-0.44	6.897	0.38	**0.0**
Nestin (Nes)	•	o	Intermediate filament	0.81	11.8	0.145	0.021	**0.1**	8.115	0.62	7.587	0.63	**0.3**
Myosin-9 (Myh9)	•	o	Cytoskeleton	0.89	33.6	0.165	0.027	**0.0**	8.994	0.63	10.271	0.57	**0.2**
Keratin, type II cytoskeletal 5 (Krt5)	•	o	Intermediate filament	0.89	11.0	0.685	0.469	**0.7**	4.911	0.27	6.880	-0.19	**0.2**
Myosin-14 (Myh14)	•	o	Cytoskeleton	0.71	6.5	0.117	0.014	**0.2**	5.794	0.50	8.092	0.56	**0.1**
Vitronectin (Vtn)	•	o	ECM	0.88	4.7	0.505	0.255	**0.5**	6.934	0.12	9.824	0.13	**-0.3**
Unconventional myosin-Ic (Myo1c)	•	o	Cytoskeleton	0.86	3.7	-0.171	0.029	**-0.2**	8.903	0.93	10.509	0.66	**0.4**
Nesprin-1 (Syne1)	o	•	Nucleus	0.14	2.9	0.575	0.331	**0.9**	6.581	-0.38	8.943	0.27	**-0.1**
Lamin-B1 (Lmnb1)	•	o	Intermediate filament	0.85	6.8	0.533	0.284	**0.2**	8.362	-0.16	7.989	0.11	**0.0**
Plastin-3 (Pls3)	•	o	Cytoskeleton	0.85	6.4	0.111	0.012	**-0.1**	8.184	0.22	9.916	0.33	**-0.1**
Myosin-11 (Myh11)	•	o	Cytoskeleton	0.75	6.4	0.000	0.000	**-0.1**	6.293	0.26	9.501	0.49	**0.3**
Filamin-B (Flnb)	•	o	Cytoskeleton	0.79	18.2	0.003	0.000	**0.0**	7.711	0.31	9.645	0.17	**0.0**
Ezrin (Ezr)	•	o	Cytoskeleton	0.86	6.0	-0.010	0.000	**0.0**	10.056	0.11	9.651	0.27	**0.1**
Alpha-actinin-1 (Actn1)	•	o	Cytoskeleton	0.47	4.0	-0.246	0.061	**-0.1**	9.553	0.33	5.063	0.42	**0.0**
Radixin (Rdx)	•	o	Cytoskeleton	0.85	4.3	-0.116	0.013	**0.0**	9.045	-0.14	10.805	0.53	**0.1**
Lamin-B2 (Lmnb2)	•	o	Intermediate filament	0.86	5.4	-0.017	0.000	**0.0**	6.655	0.77	7.306	-0.62	**0.0**
Spectrin beta chain, brain 1 (Sptbn1)	•	o	Cytoskeleton	0.85	30.4	-0.374	0.140	**-0.1**	9.883	-0.21	11.623	0.31	**-0.1**
Myosin-10 (Myh10)	•	o	Cytoskeleton	0.65	3.3	-0.299	0.089	**-0.2**	7.396	-0.23	8.770	0.13	**-0.2**
Microtubule-associated protein 1B (Map1b)	•	o	Cytoskeleton	0.52	8.4	-0.214	0.046	**-0.1**	8.954	-0.48	8.751	-0.19	**-0.4**
Spectrin alpha chain, brain (Sptan1)	•	o	Cytoskeleton	0.84	42.8	-0.226	0.051	**0.0**	8.819	-0.68	10.899	-0.30	**-0.3**
Microtubule-associated protein 1A (Map1a)	•	o	Cytoskeleton	0.83	6.9	-0.296	0.088	**-0.1**	7.199	-0.56	7.352	-0.31	**-0.5**
Neurofilament heavy polypeptide (Nefh)	•	o	Intermediate filament	0.38	3.2	-0.071	0.005	**0.1**	4.667	-0.77	6.754	-0.56	**-0.6**
Tubulin alpha-1A chain (Tuba1a)	•	o	Cytoskeleton	0.90	6.4	-0.465	0.216	**-0.1**	9.080	-0.60	10.842	-0.11	**-0.2**
Microtubule-associated protein 6 (Map6)	•	o	Cytoskeleton	0.79	10.0	-0.306	0.094	**0.0**	5.656	-0.79	7.097	-0.25	**-0.3**
Neurofilament light polypeptide (Nefl)	•	o	Intermediate filament	0.88	14.8	-0.256	0.066	**-0.1**	4.702	-0.79	5.047	-0.44	**-0.9**
Neurofilament medium polypeptide (Nefm)	•	o	Intermediate filament	0.70	6.1	-0.285	0.081	**-0.1**	4.431	-0.82	5.343	-0.51	**-0.7**
Microtubule-associated protein 2 (Map2)	•	o	Cytoskeleton	0.71	13.5	-0.470	0.221	**-0.3**	5.770	-0.72	6.640	-0.52	**-0.7**
Tenascin-R (Tnr)	•	o	ECM	0.60	3.3	-0.544	0.295	**-0.5**	4.461	-0.75	5.928	-0.43	**-0.6**
Tubulin beta-2B chain (Tubb2b)	•	o	Cytoskeleton	0.81	6.4	-0.817	0.668	**-0.4**	6.066	-0.49	6.900	-0.25	**-0.3**

B Cytoskeleton components (SRF or YAP1 targets) do not scale with *E* (proteomic analysis)

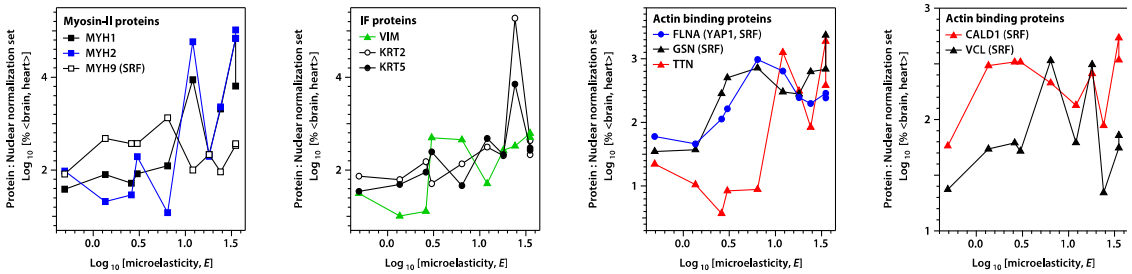

C *SRF* and *ACTA2* scaling with *E* (mRNA analysis)

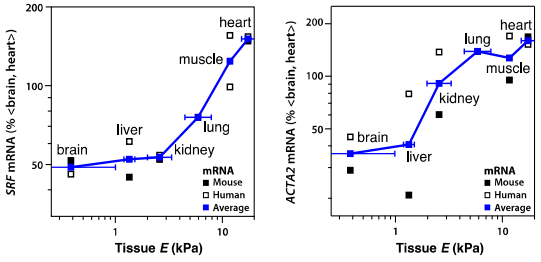

D Correlation between *PTRF*, *LMNA* and *COL1A1*

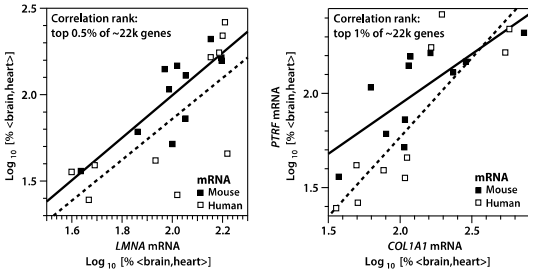

Fig. S2. Protein and mRNA correlations with *E* for structural and extracellular proteins: lamin-A and collagens show strong correlation in total protein and mRNA levels. Columns summarize proteomic and transcript data, and rows are sorted by the mean strength of correlation with lamin-A protein and transcript. Almost all of the most strongly correlated proteins are from the extra-cellular matrix (ECM). (B) Scaling of cytoskeletal protein levels with tissue microelasticity. The SRF and YAP1 pathways are mechanosensitive in culture and some of their detected products are highlighted here (*11*, *18*). Correlations with tissue stiffness are not as apparent as with lamin-A (Fig. 1D). SRF targets tend to show similar trends, such as caldesmon-1 (CALD1) and vinculin (VCL), suggesting accuracy of the protein measurements. (C) *SRF* and *ACTA2* mRNA vary with tissue microelasticity over a range of tissues in mouse and man: *SRF* shows flat response at low *E*, but steeply increases in stiffer tissues. (D) Polymerase I and transcript release factor (*PTRF*) message was found to correlate strongly with *LMNA* and *COL1A1* over a range of tissues in mouse and man, with correlation ranking in the top 1% of all genes in both cases.

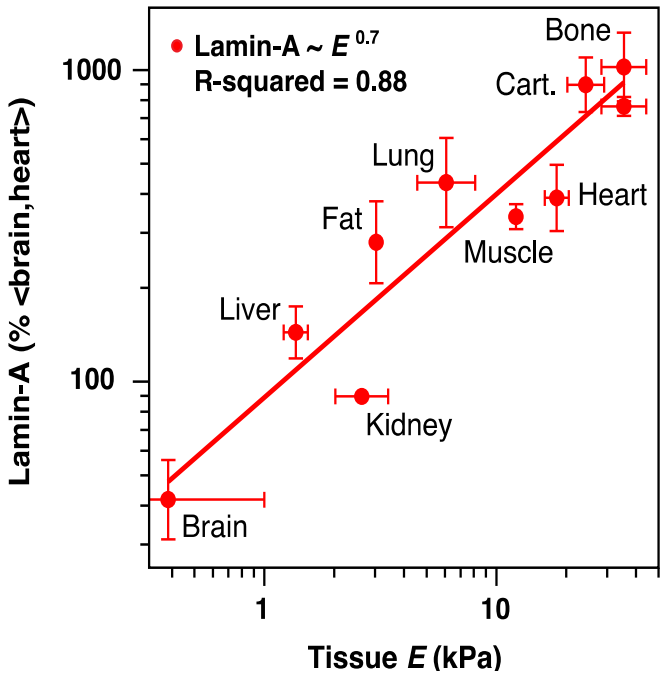

Fig. S3. Lamin-A scaling with *E*. Scaling of lamin-A protein in mouse tissue, as measured by mass spectrometry relative to a nuclear normalization set chosen to be invariant across all sampled tissues and expressed as a percentage of the mean average level in heart and brain. Note that this is the *relative* scaling of the concentration of the overlap region of lamin-A and -C splice-forms, in contrast to Fig. 1D which shows the *absolute* scaling of the ratio lamin-(A or C) : lamin-(B1 or B2), or Fig. S5D which separates the scaling of lamin-A and -C splice-forms.

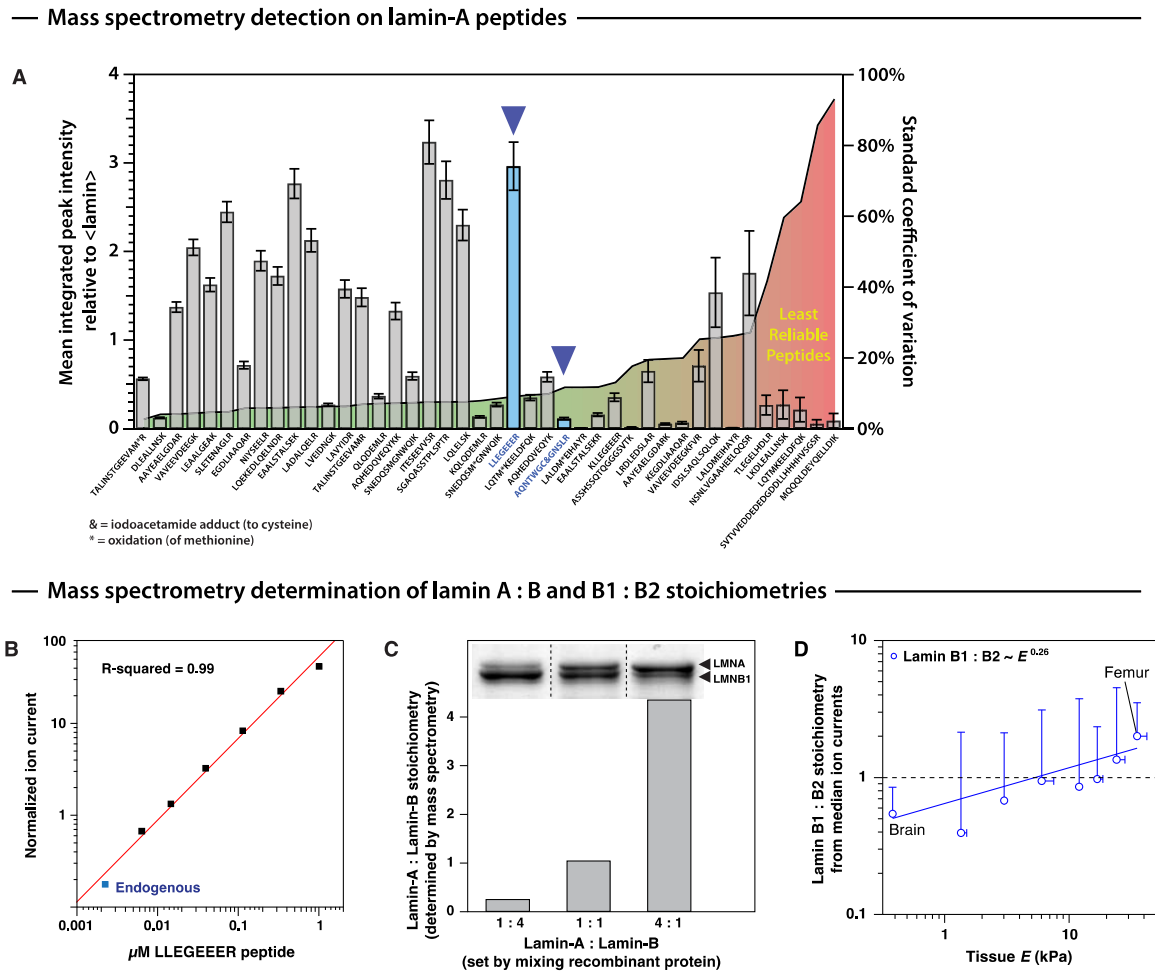

Fig. S4. Mass spectrometry quantification of lamin stoichiometries. (A) Integrated intensities of lamin-A peptides relative to the mean of all lamin-A peptides, averaged over a series of seven injections into the mass spectrometer of trypsinized A549 lysate (MW 55 – 160 kDa) at dilutions: 40%, 50%, 60%, 70%, 80%, 90% and 100% (error bars show SEM). The peptide used for lamin isoform determination, LLEGEEER, has the second highest signal of the lamin peptides and a standard error 9% of the mean signal intensity. The peptide used as a reporter of the folded state of the Ig domain (AQNTWGCGNSLR, Fig. 2) has a standard error of 12% of the mean signal intensity. (B) Mass spectrometry analysis of LLEGEEER peptide titrated into a tryptic digest of A549 cells shows a linear response to concentration over several orders of magnitude. (C) As proof of concept, the method for determining the absolute lamin-A:B ratio (see Methods) was applied to a mixture of recombinant lamin-A and lamin-B1. Mass spectrometry returned the absolute ratio expected from the original mixing stoichiometry (protein concentration was determined by UV-absorbance and matched by Coomassie staining of SDS-PAGE gels). (D) Scaling of lamin-B1:B2 ratio in mouse tissue, as measured by the ratio of median ion currents recorded in mass spectrometry. This rough estimate of stoichiometry suggests that lamin-B1 and B2 are present at similar concentrations.

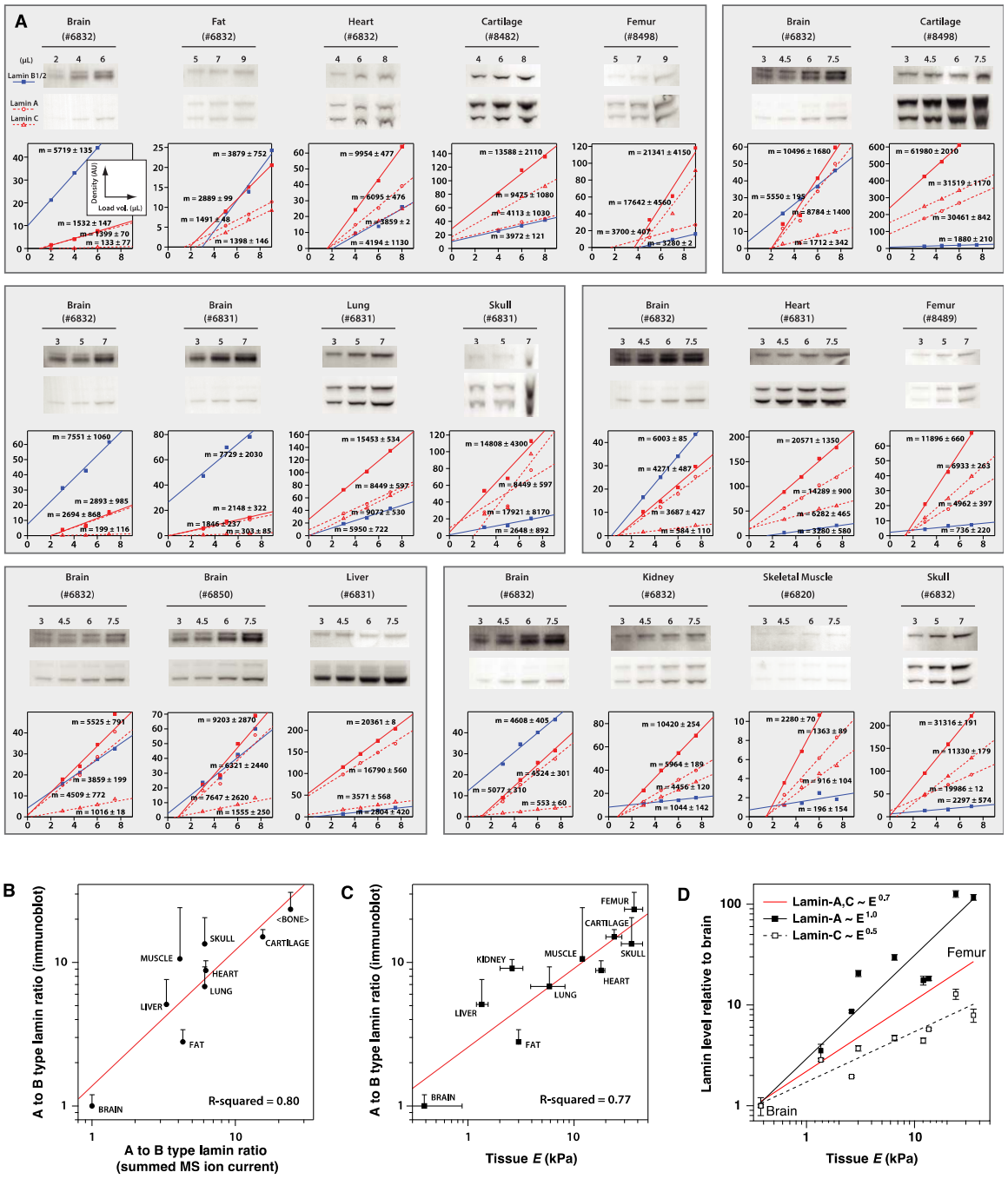

Fig. S5. Immunoblot validation of lamin quantification in tissue. (A) Multiple volumes were used to establish a linear response to concentration. Relative ratios of lamins A and B were calculated from ratios of gradients. Four-digit numbers identify different adult mice. A sample of brain (#6832) was used for common normalization of each immunoblot (separated in gray panels). (B) Correlation between mass spectrometry and immunoblot of lamin quantification in tissue. (C) Correlation between lamina composition, as determined by immunoblot (relative to brain), and tissue microelasticity. (D) Although this work focuses on total A-type lamin (i.e. the sum of both A and C splice-forms), immunoblotting allows separation of contributions from lamin-A and lamin-C. Total lamin-(A+C) scales with $E^{0.7}$ (Fig.

S3A), but splitting the two splice-forms shows that lamin-A scales more dramatically, with $E^{1.0}$, whereas lamin-C scales as $E^{0.5}$. Lamin-A is suppressed in the brain by microRNA *MIR-9* (*109*) and an analysis of *MIR-9s* in tissue microarrays confirms abundant expression in brain but without any systematic relation to *E*.

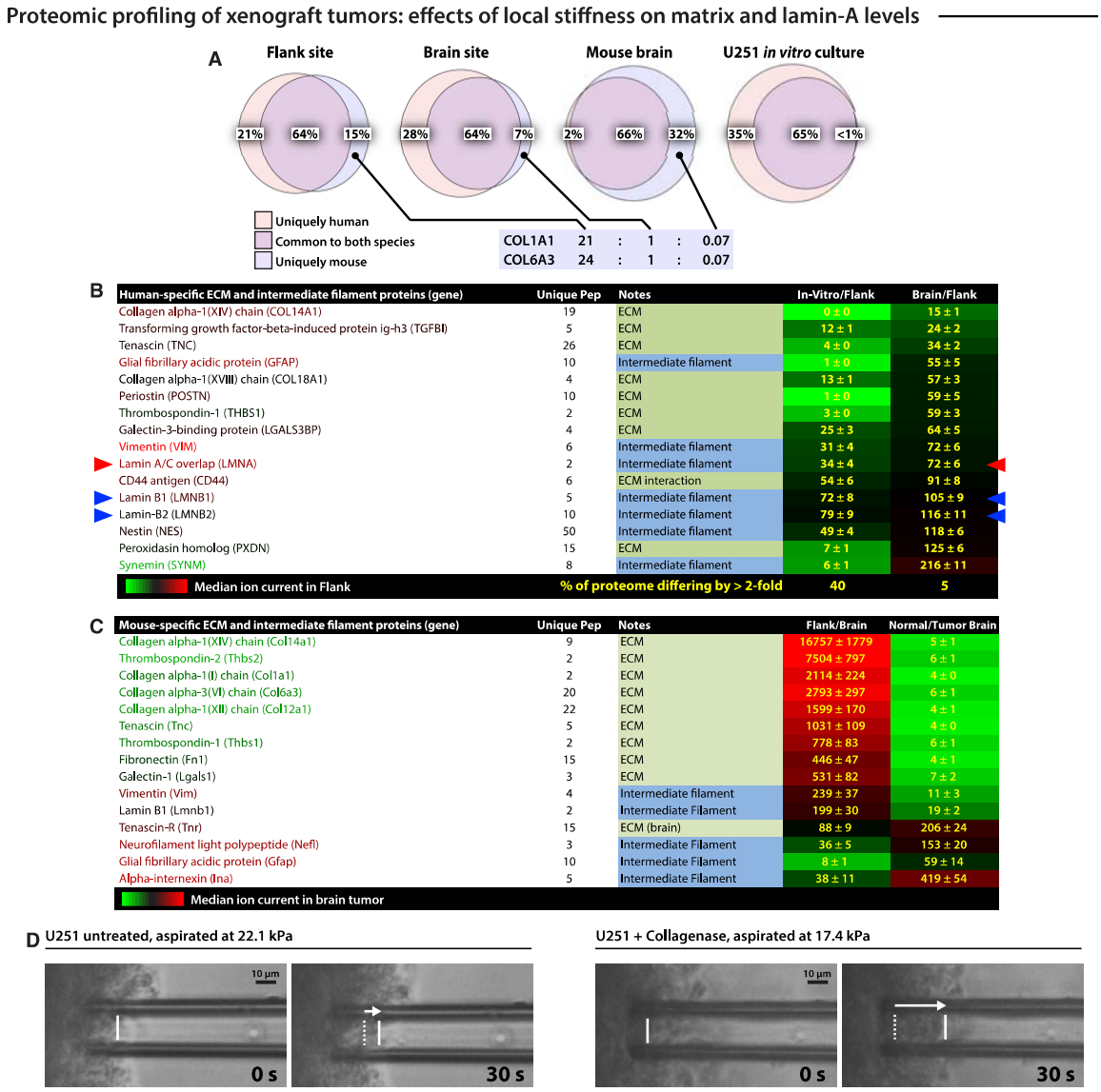

Fig. S6. Proteomic profiling of U251 xenograft tumors and mechanical properties of tumors. Xenografts were harvested after 4 wks, solubilized, and prepared for quantitative, label-free mass spectrometry. (A) About 20 - 30% of peptides from the tryptic digests were uniquely human, with quantitation done for almost 200 human proteins. Mouse collagens were quantified from uniquely mouse derived peptides. (B) Human cells in the brain express lower ECM proteins and lower lamin-A than human cells in the flank ($p \leq 0.05$; $n = 3$), consistent with brain being softer than flank per Fig. 1D. Lamin-B2 is essentially constant, and lamin-B1 changes much less than lamin-A, consistent with Fig. 1F. Only about 5% of quantifiable proteins indeed differ between the two *in vivo* sites by more than 2-fold. The difference between the flank tumor and cultured cells is more pronounced, with 40% of

proteins differing by more than 2-fold. (C) Mouse-specific proteins quantified by mass spectrometry. (D) Sample images showing micropipette aspiration of tumor tissue. A constant pressure is applied and the rate of deformation into the pipette is recorded. U251 tumor tissue is shown before and after 10 minutes treatment with collagenase, which significantly reduces the elasticity of the tissue.

Name (Gene)	Peptide Sequence (# = mBBr)	Domain annotations	Labeling observations
ATP-dependent RNA helicase (DDX18)	NLQC#LVIDEADR	close to DEAD box motif	no change in rate or extent
ATP-dependent RNA helicase (DDX3X)	DLMAC#AQTGSGK	nucleotide binding site	no change in rate or extent
	GC#HLLVATPGR		2x increase in label rate 0 - 2 Pa
	IGLDFC#K	close to DEAD box motif	no change in rate or extent
ATP-dependent RNA helicase (DDX5)	ELAQQVQQVAAEYC#R		no change in rate or extent
	STC#IYGGAPK		increase in extent of labeling above 1.5 Pa
	LIDFLEC#GK	close to DEAD box motif	no change in rate or extent
	RC#DELTR		no change in rate or extent
Calpain-2 catalytic subunit (CAPN2)	RPTEIC#ADPQFIIGGATR		increase in extent and rate of labeling
	LEIC#NLTPDTLTSDTYK		no consistent change in rate or extent
Cleavage and polyadenylation specificity factor subunit 6 (CPSF6)	ELHGQNPVVTPC#NK	RNA recognition motif	no consistent change in rate or extent
DNA replication licensing factor (MCM5)	AIAC#LLFGGSR	minichromosome maintenance	increase in extent of labeling above 1.5 Pa
DNA-dependent protein kinase catalytic subunit (PRKDC)	FLC#IFLEK		increase of initial label rate; increase in extent of labeling 0 - 1.5 Pa
	DILPC#LDGYLK		increase of initial label rate; increase in extent of labeling 0 - 0.5 Pa
	LAAVVSAC#K		slowing of initial label rate; increase in extent of labeling 0 - 1.5 Pa
	NILEESLC#ELVAK		kinetics too fast to measure; increase in extent of labeling 0 - 0.5 Pa
FACT complex subunit (SSRP1)	ADVIQATGDAIC#IFR		labeling extent drops 0 - 1 Pa; increases above 1 Pa
Guanine nucleotide-binding protein-like 3 (GNL3)	LYC#QELK		no change in rate or extent
	C#PQVEEAIVQSGQK		no change in rate or extent
	SEVC#FGK		no change in rate or extent
	LLGGFQETC#SK		no change in labeling extent, 1.5x increase in label rate; 0 - 1.5 Pa
Heat shock 70 kDa protein 1A/1B (HSPA1A/B)	FEELC#SDLFR		large increase in extent of labeling above 1 Pa
	C#QEVISWLDANTLAEKDEFEHK		low signal, noisy; increase in rate above 1 Pa
Heat shock cognate 71 kDa protein (HSPA8)	C#NEIINWLDK		large increase in extent of labeling above 1 Pa
	VC#NPIITK		large increase in extent of labeling above 1 Pa
Heat shock protein HSP 90-beta (HSP90AB1)	C#LELFSELAEDKENYK		increase in extent of labeling above 1.5 Pa
Heterogeneous nuclear ribonucleoprotein K (HNRNPK)	GSDFDC#ELR		increase in extent of labeling 0 - 1 Pa
Heterogeneous nuclear ribonucleoprotein L (HNRNPL)	LNVC#VSK	RRM3 domain	increase in extent of labeling 0 - 2 Pa
	LC#FSTAQHAS		no consistent change in rate or extent
Heterogeneous nuclear ribonucleoprotein M (HNRNPM)	AC#QIFVR		no consistent change in rate or extent
Heterogeneous nuclear ribonucleoprotein Q (SYNCRIP)	SAFLC#GVMK		no consistent change in rate or extent
	GFC#FLEYEDHK		no consistent change in rate or extent
Heterogeneous nuclear ribonucleoprotein U (HNRNPU)	VC#FEMK	B30.2/SPRY domain	increase in extent of binding 0 - 2 Pa
Lamin A (LMNA)	TVLCGTC#GQPADK	tail domain	no significant change in rate or extent
Lamin A/C (LMNA)	AQNTWGC#GNSLR	Ig domain	kinetics too fast to measure; increase in extent of labeling 0 - 1 Pa
Lamina-associated polypeptide 2, isoform alpha (TMPO)	SGIQPLC#PER		Fast labeling of soluble protein; additional labeling at above 1 Pa
	GGTLFGGEVC#K		Fast labeling of soluble protein; additional labeling at above 1 Pa
Leucine-rich PPR motif-containing protein, mitochondrial (LRPPRC)	C#VANNQVETLEK		increase in extent of labeling 0 - 0.5 Pa; no significant change in rate 0.5 - 1.5 Pa
	DILIAC#R	PPR repeat	increase in extent of labeling 0 - 1.5 Pa
Medium tumor antigen-associated 61 kDa protein (PPP2R1A)	ENVIMSQILPC#IK	PP2A subunit B binding site	probably no increase in extent of labeling, large increase in rate (0 - 2 Pa)
	DEC#PEVR	PP2A subunit B binding site	no consistent change in rate or extent
Nucleolar protein 11 (NOL11)	ESTSC#PVVQK		no consistent change in rate or extent
Nucleolar protein 56 (NOP56)	GLTDLSAC#K		2x slowing on labeling rate rate 0 -2 Pa
Nucleolin (NCL)	EALNSC#NK	RNA recognition motifi	ncrease in extent of labeling above 1.5 Pa
Origin recognition complex subunit 3 (ORC3)	ENVVNFIDC#LVR		no consistent change in rate or extent
Polyadenylate-binding protein 1 (PABPC1)	VVC#DENGSK	RNA recognition motif	no consistent change in rate or extent
Probable ATP-dependent RNA helicase (DDX41)	MVYLLEC#LQK	helicase C-terminal domain	no change in rate or extent
Pumilio domain-containing protein (KIAA0020)	GAILSSLLQSC#DLEVANK		no consistent change in rate or extent
Pyruvate kinase isozymes M1/M2 (PKM2)	NTGIIC#TIGPASR		increase in initial label rate 0 - 0.5 Pa; increase in extent of labelling 0.5 - 1 Pa
	C#DENILWLDYK		increase in initial label rate 0 - 1.5 Pa; increase in extent of labelling 0.5 - 1 Pa
	AGKPVIC#ATQMLESMIK	OCT4 binding region	increase of initial label rate; increase in extent of labeling 0 - 1 Pa
	PVIC#ATQMLESMIK	OCT4 binding region	increase of initial label rate; increase in extent of labeling 0 - 1 Pa
	GIFPVLC#K	OCT4 binding region	increase in initial label rate 0 - 0.5 Pa; increase in extent of labelling 0.5 - 1 Pa
Replication protein A 70 kDa DNA-binding subunit (RPA1)	DSLVDIIGIC#K		no change in labeling rate, slight increase in label extent (approx 30 %) (0 - 1.5 Pa)
Ribosomal L1 domain-containing protein 1 (RSL1D1)	EINDC#IGGTVLNISK		no consistent change in rate or extent
	SGSC#SAIR		no change in rate or extent
RNA-binding protein 14 (RBM14)	IFVGNVSAAC#TSQELR	RNA recognition motif	no change in rate or extent
RNA-binding protein 39 (RBM39)	C#PSIAAAIAAVNALHGR	NCOA6 binding region	increase in rate and extent of labeling (0 - 1.5 Pa)
Stress-induced-phosphoprotein 1 (STIP1)	ALSVGNIDDALQC#YSEAIK	HSC70 binding region	increase in extent of labeling above 1 Pa
SUMO-activating enzyme subunit 2 (UBA2)	VLVVGAGGIGC#ELLK	nucleotide binding region	large increase in extent of labeling above 1 Pa
Ubiquitin-like modifier-activating enzyme 1 (UBA1)	YFLVGAGAIGC#ELLK	nucleotide binding region	large increase in extent of labeling above 1 Pa
WD repeat domain 46 (WDR46)	IC#QADIVEAVDIASAAK		no change in extent of labeling, rate increases to be too fast to measure (0 - 2 Pa)
WD repeat-containing protein 43 (WDR43)	DISNC#WAPK		no consistent change in rate or extent
X-ray repair cross-complementing protein 5 (XRCC5)	LFQC#LLHR	proline rich region	increase in rate and extent of labeling above 1.5 Pa

Pink = increase in extent or rate of labeling. Green = decrease in extent or rate of labeling. Gray = no consistent change in extent or rate of labeling.

Fig. S7. CS-MS identifies multiple stress-sensitive proteins, including the Ig domain of lamin-A. Summary of cysteine-labeled peptides detected by LC-MS/MS from nuclear proteins in the 60 - 80 kDa weight range, following mBBr labeling of isolated A549 nuclei under 0 - 2 Pa shear stress (Figs. 2C and D). Labeling sites are classified as either responsive (pink) or unresponsive (grey) to shear stress. Stress sensitive proteins include GNL3, implicated in stem cell proliferation, and also pyruvate kinase (PKM2) in a domain known to interact with the transcription factor OCT4 (*110*).

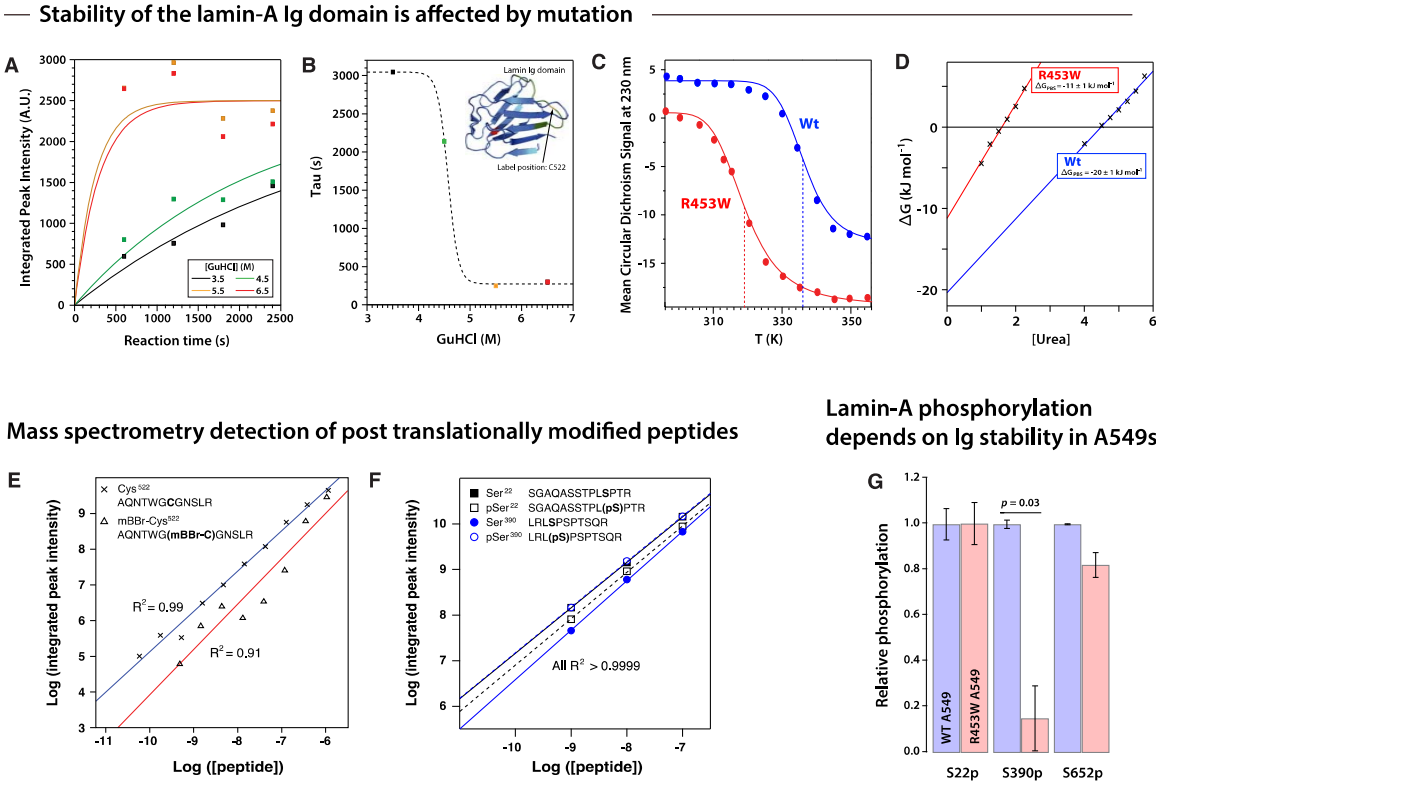

Fig. S8. Lamin-A responds to destabilizing mutation with altered folding and phosphorylation. (A) Rate of labeling of a cysteine residue in recombinantly expressed and purified lamin Ig domain at different concentrations of chemical denaturant, as determined by HPLC. (B) The labeling kinetics give a picture of the two-state unfolding of the domain, allowing an assessment of protein stability without spectroscopic techniques. Inset shows the crystal structure of the lamin Ig domain (PDB accession number: 1IFR) (*111*) with the position of the cysteine labeling site shown in yellow and the detected tryptic peptide highlighted in green. (C) Unfolding of recombinant wildtype (Wt) and disease mutant (R453W) lamin Ig domains as a function of temperature, as measured by circular dichroism (CD). (D) Extrapolation of the stabilities of Wt and R453W lamin Ig domains in buffer at 37 °C, measured by tryptophan fluorescence. Spiking key peptides into a tryptic digest of A549 cells confirmed that they could be correctly identified by mass spectrometry and that the detection signal is proportional to concentration: (E) the mBBr labeled peptide from the Ig domain of lamin-A, AQNTWGCGNSLR (Figs. 2E, H, 3F); (F) lamin-A phospho-peptides, SGAQASSTPLSPTR and LRLSPSPTSQR (Figs. 2I, 3G, H). (G) Phosphorylation was detected in experiments that quantified mBBr labeling in A549s and MSCs: Ser^{22} (lamin-A head domain, CDK1 target); Ser^{390} (lamin-A Ig domain, CDK1 target); Ser^{652} (lamin-A tail domain). In A549 cells, the extent of phosphorylation per lamin molecule is greatly reduced (five-fold) at the Ser^{390} site in the disease mutant; other sites were not significantly altered. This result demonstrates coupling between protein conformation and the modification of an adjacent phosphosite and thus could lead to regulation of lamina assembly.

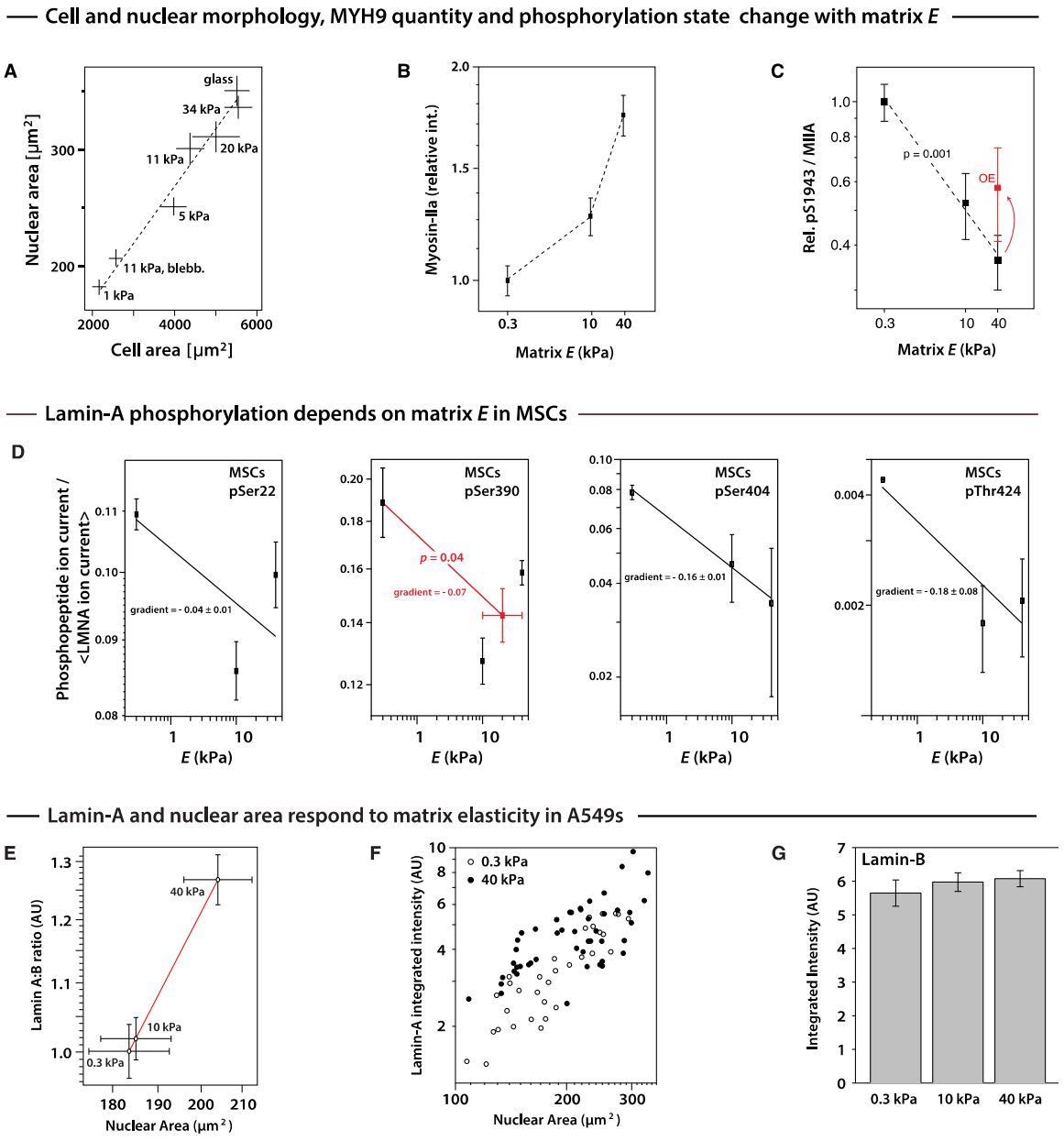

Fig. S9. Metrics of cell tension increased with matrix stiffness but lamin-A phosphorylation decreased. (A) Projected nuclear area is proportional to cell spread area in low passage MSCs on substrates of increasing stiffness. (B) Total levels of non-muscle myosin-IIA (MYH9, an SRF target gene) in MSCs, as determined by immunofluorescence, increases with substrate stiffness. (C) Phosphorylation of MYH9 at Ser^{1943}, indicates myosin deactivation (*43*) and decreases on stiffer substrates, although over-expression of LMNA induces an anomalous rise in phosphorylation. (D) Phosphorylation was detected at a number of LMNA sites in cells cultured on matrices of varying elasticity: Ser^{22}, Ser^{390} (CDK1 sites), Ser^{404} (*112*) and Thr^{424} (previously unreported). Phosphorylation was consistently higher on soft vs. stiff substrate. For Ser^{390}, both 10 and 40 kPa data points were combined into a single "stiff" point in order to achieve a statistically significant difference from soft (0.3 kPa) (Kruskal-Wallis $p = 0.04$). Phosphorylation of Ser^{390} was also detected in tissue, where division of

terminally differentiated cells is estimated to take years (*113, 114*). (E) A549 cells were cultured on substrates of different stiffnesses for 3 days. Cells were immunostained for lamins A and B after fixing. Analysis of the images revealed a weak but significant sensitivity to the microenvironment, with increase in lamin-A:B ratio and mean nuclear spread area on stiffer substrate. (F) Correlation between lamin-A level and nuclear area in A549 cells on soft and stiff substrate. (G) Lamin-B levels in A549 cells are not significantly affected by changes in substrate stiffness.

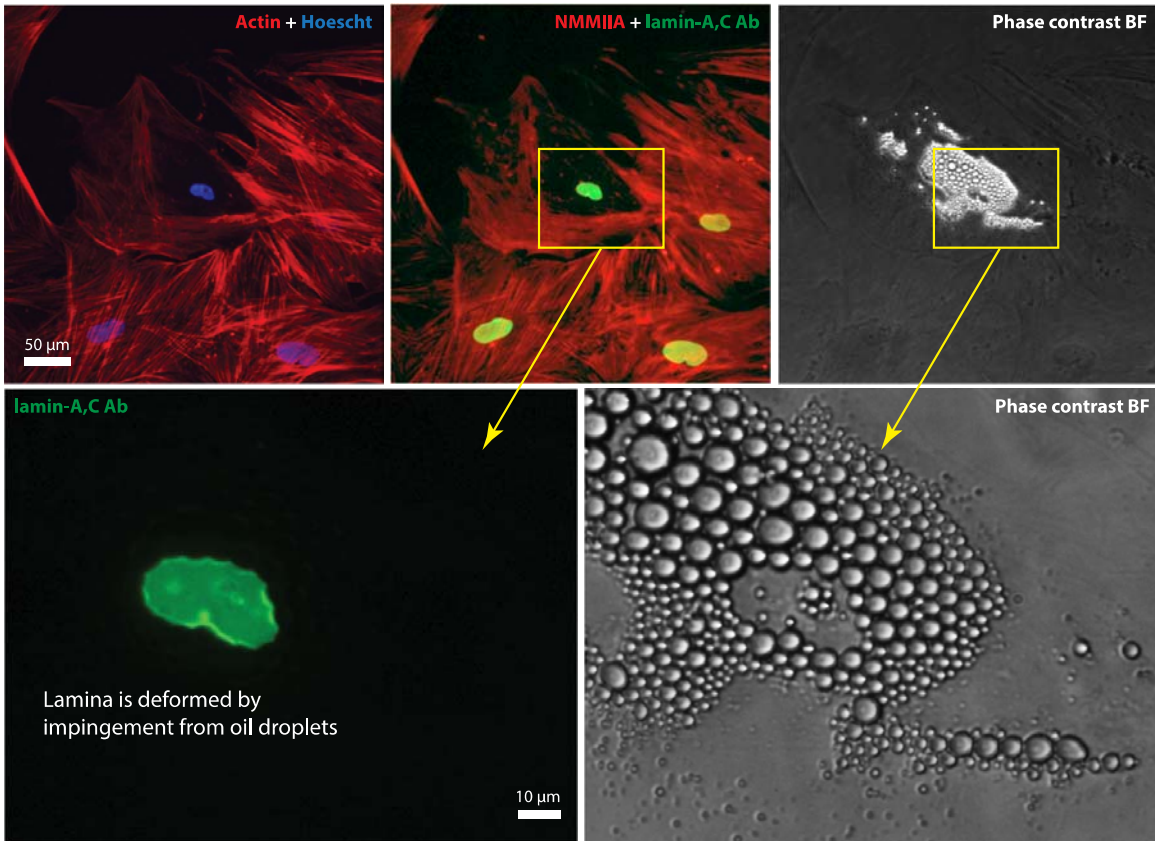

Fig. S10. Images of adipogenic MSCs reveals loss of cytoskeleton and deformed nucleus. Adipogenesis in MSCs grown on plastic with the formation of oil droplets observed by phase contrast microscopy. The oil droplets impinge on the nucleus causing deformation.

A

Protein (Gene)	Notes	<PRF> / Total	<R²>	AI / NT	Scr+AI / NT	KD+AI / NT	KD+AI / Scr+AI
Long-chain-fatty-acid--CoA ligase 1 (ACSL1)	Fatty acid & lipid metabolism	3.1 / 5	0.53	1892 ± 197	2841 ± 568	9669 ± 862	280 ± 71
Prolyl 4-hydroxylase subunit alpha-1 (P4HA1)	Collagen processing	5.3 / 10	0.53	21 ± 3	32 ± 5	39 ± 5	170 ± 41
Heat shock 70 kDa protein 1A/1B (HSPA1A/B)		3.4 / 7	0.66	109 ± 34	78 ± 3	98 ± 5	139 ± 13
Neutral alpha-glucosidase AB (GANAB)	Glycoprotein processing	8.0 / 15	0.76	158 ± 3	148 ± 7	194 ± 10	132 ± 12
Alpha-actinin-1/2/3/4 overlap (ACTN1/2/3/4)		3.9 / 6	0.85	104 ± 17	101 ± 11	107 ± 6	131 ± 40
Calnexin (CANX)		7.6 / 15	0.87	85 ± 36	145 ± 8	226 ± 53	129 ± 13
Peptidyl-prolyl cis-trans isomerase (FKBP10)		5.8 / 11	0.87	108 ± 3	87 ± 5	115 ± 7	128 ± 15
Gelsolin (GSN)		6.3 / 13	0.56	87 ± 5	133 ± 8	99 ± 6	112 ± 31
Protein disulfide-isomerase A4 (PDIA4)		6.5 / 12	0.74	171 ± 16	175 ± 17	197 ± 8	110 ± 10
Protein disulfide-isomerase (P4HB)		16.4 / 28	0.91	174 ± 13	179 ± 4	198 ± 8	104 ± 7
78 kDa glucose-regulated protein (HSPA5)	Stress response	17.4 / 25	0.94	144 ± 7	159 ± 8	165 ± 6	101 ± 5
Aminopeptidase N (ANPEP)	Differentiation processes	6.4 / 13	0.68	242 ± 34	305 ± 62	224 ± 30	100 ± 16
Ribosome-binding protein 1 (RRBP1)		9.0 / 17	0.66	83 ± 15	108 ± 6	98 ± 10	96 ± 10
Ribophorin-1 (RPN1)	Glycoprotein processing	10.0 / 18	0.87	207 ± 11	146 ± 9	136 ± 6	96 ± 7
Cytoskeleton-associated protein 4 (CKAP4)		14.3 / 21	0.90	207 ± 10	147 ± 8	129 ± 8	94 ± 10
Very long-chain specific acyl-CoA dehydrogenase, mito. (ACADVL)	Fatty acid & lipid metabolism	5.0 / 10	0.76	207 ± 14	302 ± 26	320 ± 25	93 ± 7
Transitional endoplasmic reticulum ATPase (VCP)		7.2 / 14	0.54	105 ± 14	155 ± 23	135 ± 12	91 ± 18
Elongation factor 2 (EEF2)		10.3 / 19	0.58	87 ± 5	133 ± 10	116 ± 7	90 ± 9
Stress-70 protein, mitochondrial (HSPA9)	Stress response	5.3 / 13	0.77	206 ± 104	333 ± 56	315 ± 12	90 ± 5
Alpha-actinin-4 (ACTN4)		14.5 / 26	0.84	122 ± 11	136 ± 6	97 ± 6	82 ± 6
Endoplasmin (HSP90B1)	Stress response	13.0 / 27	0.94	156 ± 15	204 ± 7	171 ± 9	81 ± 5
Protein disulfide-isomerase A3 (PDIA3)		13.1 / 17	0.94	177 ± 9	203 ± 6	160 ± 6	80 ± 5
Pyruvate kinase isozymes M1/M2 (PKM2)	Stimulates POU5F1 activation	15.8 / 27	0.84	49 ± 9	76 ± 5	57 ± 4	79 ± 10
Heat shock cognate 71 kDa protein (HSPA8)		14.6 / 20	0.95	130 ± 8	153 ± 8	115 ± 2	77 ± 5
Procollagen-lysine,2-oxoglutarate 5-dioxygenase 2 (PLOD2)	Collagen processing	10.3 / 17	0.91	92 ± 6	113 ± 4	73 ± 3	76 ± 16
Transketolase (TKT)		5.0 / 8	0.84	73 ± 9	126 ± 17	87 ± 7	75 ± 9
Alpha-actinin-1 (ACTN1)		17.6 / 27	0.86	141 ± 3	159 ± 7	102 ± 4	75 ± 9
Heat shock protein HSP 90-alpha (HSP90AA1)		7.5 / 12	0.86	93 ± 6	157 ± 6	104 ± 5	73 ± 13
Annexin A6 (ANXA6)		15.6 / 30	0.87	119 ± 4	105 ± 5	66 ± 4	71 ± 7
Vinculin (VCL)		18.5 / 29	0.89	179 ± 6	127 ± 5	82 ± 4	70 ± 4
Glucose-6-phosphate 1-dehydrogenase (G6PD)	Carbohydrate metabolism	3.2 / 6	0.60	289 ± 38	627 ± 127	412 ± 60	69 ± 5
Heat shock protein HSP 90-alpha/beta (HSP90AA/B1)		3.5 / 6	0.93	115 ± 5	173 ± 5	96 ± 4	61 ± 4
6-phosphofructokinase type C (PFKP)	Carbohydrate metabolism	3.6 / 9	0.73	145 ± 7	98 ± 81	83 ± 8	59 ± 8
WD repeat-containing protein 1 (WDR1)		6.3 / 11	0.85	89 ± 8	114 ± 8	59 ± 5	56 ± 6
Heat shock protein HSP 90-beta (HSP90AB1)		6.8 / 10	0.88	109 ± 8	135 ± 6	76 ± 7	56 ± 4
Moesin/Radixin/Ezrin overlap (MSN/RDX/EZR)		4.8 / 7	0.92	79 ± 8	124 ± 4	43 ± 5	52 ± 5
Protein-glutamine gamma-glutamyltransferase 2 (TGM2)		10.5 / 18	0.93	159 ± 8	156 ± 12	67 ± 4	49 ± 6
EH domain-containing protein 2 (EHD2)		3.2 / 7	0.69	74 ± 24	90 ± 10	34 ± 3	41 ± 3
Vimentin (VIM)	Cages lipid droplets (Franke, 1987)	21.8 / 29	0.93	1134 ± 58	1000 ± 52	361 ± 18	39 ± 3
Lamin A/C overlap (LMNA)		12.7 / 21	0.94	96 ± 26	202 ± 15	45 ± 3	26 ± 2

Median ion current <NT> Normalization

B

	Correlation in human tissue mRNA			Correlation in mouse tissue mRNA			mRNA changes with LMNA KD in MSCs				24 hr drug in MSCs
	Pearson Rank	R²	Gradient	Pearson Rank	R²	Gradient	M47A KD/NT	M47B KD/NT	Lonza KD/NT	SCR/NT	PDN/NT
LMNB2	220	0.590	0.333	14393	0.378	-0.546	113.0%	95.8%	101.7%	82.6%	208.6%
LMNB1	9685	0.019	-0.125	6578	0.015	0.189	100.5%	107.4%	114.8%	136.4%	180.7%
LMNA	1	1.000	1.000	1	1.000	1.000	37.9%	37.3%	32.2%	103.0%	85.5%
Adipogenic lineage markers (* = increased at protein level in MS analysis)											
LEP	2164	0.252	0.977	2238	0.208	0.481	88.4%	84.2%	23.8%	108.5%	274.6%
ACSL1*	961	0.384	1.203	5308	0.049	0.327	125.3%	131.9%	93.2%	103.6%	143.2%
PPARG	2479	0.227	0.729	98	0.632	0.690	107.0%	117.1%	112.5%	379.4%	125.9%
SOD2	895	0.368	0.698	6268	0.021	0.155	177.8%	109.0%	49.5%	130.4%	116.6%
FASN*	6871	0.013	0.224	5001	0.059	0.277	105.8%	98.6%	98.2%	138.4%	116.5%
FABP4	336	0.495	3.758	1836	0.242	1.202	106.6%	92.9%	110.5%	153.1%	101.4%
LPL	967	0.383	2.491	669	0.407	1.270	101.3%	94.6%	102.5%	100.1%	100.0%
PPARD	8562	0.003	-0.026	914	0.363	0.355	117.0%	114.0%	102.4%	85.6%	100.0%
FABP2	5253	0.059	0.068	5348	0.048	0.477	100.0%	98.5%	94.5%	98.0%	100.0%
PPARGC1A	4693	0.075	0.719	6471	0.017	0.312	111.0%	90.4%	116.1%	113.6%	100.0%
CANX*	6749	0.008	0.059	4956	0.061	0.130	91.3%	99.0%	109.4%	102.8%	100.0%
ACADVL*	606	0.441	1.007	1969	0.231	0.751	93.6%	94.5%	83.9%	88.1%	99.2%
GANAB*	5022	0.061	0.220	6112	0.026	0.105	110.0%	122.1%	103.5%	102.4%	91.2%
PPARGC1B	1642	0.294	0.314	6606	0.015	0.117	107.6%	96.1%	103.6%	106.9%	84.9%
PPARA	1950	0.275	0.750	5883	0.032	0.391	110.5%	135.0%	114.5%	136.9%	79.6%
VIM*	1985	0.234	0.842	488	0.450	0.643	107.3%	113.5%	103.7%	110.4%	60.6%
ATF3	278	0.563	0.765	108	0.626	0.765	85.2%	97.1%	89.7%	94.2%	52.8%

Expression in NT

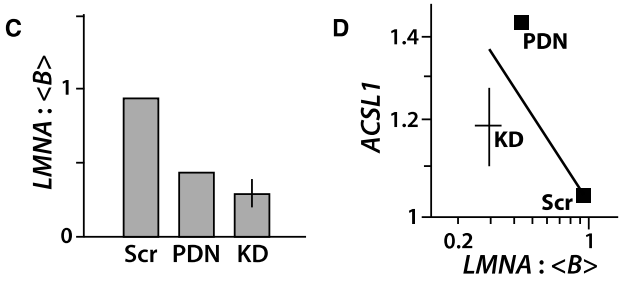

Fig. S11. Profiling of MSCs after lamin-A knockdown reveal markers of adipogenesis. (A) Proteomic comparison between untreated MSCs (NT) and those treated with an adipo-inducing cocktail (AI) or an adipo-inducing cocktail combined with either lamin knock-down (KD+AI) or scrambled mRNA (Scr+AI). Following cell lysis and tryptic digestion, peptides from proteins in the molecular weight range 55 - 160 kDa were identified and quantified using label-free liquid-chromatography

coupled tandem mass spectrometry (LC-MS/MS). Ion currents were normalized against signal from an experimentally determined set of housekeeping proteins (proteins contributing to the housekeeping set are highlighted in blue). Analysis was performed using a Peak Ratio Fingerprinting (PRF) algorithm that selected a subset of reliable peptides on which to base quantification i.e. a correlation between pair-wise ratios with R^2 greater than 0.90, except in cases where there are a limited number of good peptides, in which case the best peptides are selected with up to 50% of the original number discarded and a lower R^2 is accepted. Adipogenic marker ACSL1 (long-chain-fatty-acid-CoA ligase 1) is upregulated during LMNA knockdown. Vimentin has previously been reported to form cages around developing lipid droplets (*115*). (B) Profiling mRNA markers of osteo- and adipogenesis. Columns 2 through 7 show correlation in human and mouse tissues. In addition, microarray analysis of mRNA (shown as a heatmap in columns 8 through 14) was used to quantify changes in MS-identified proteins plus other adipogenic markers 24 hrs after treatment with an adipo-inducer (prednisolone, PDN (*116*)), , or LMNA knockdown (KD and KD2 with an alternative siRNA) in MSCs grown on plastic (Lonza plus donor cultures M47A and B). Broader examination of additional adipogenic factors and markers in MSCs are also suggestive of a general anti-correlation with *LMNA*, but ACSL1 is the most consistent in its response within cultured MSCs. Across multiple soft and stiff human and mouse tissues (but not fat), *LMNA* and *ACSL1* are neither anti-correlated nor correlated (R^2 = 0.05, 0.38) whereas adipogenic genes generally correlate positively with *LMNA* and are anti-correlated with *LMNB1*. (C) While suppressing LMNA does favor lipid droplets and adipogenesis, and while adipo-cocktail alone does not greatly change LMNA (Fig. 4E), the A:B ratio decreases because of significant increases in *LMNB1* and *LMNB2*. Indeed, higher-than-average B-type lamin levels are consistent with proteomic profiling of fat *versus* other tissues (Fig. 1E). (D) At the mRNA level, *ACSL1 anti-correlates* with A:B across a range of conditions.

LMNA knockdown decreases SRF target and total YAP1 protein but not RAR

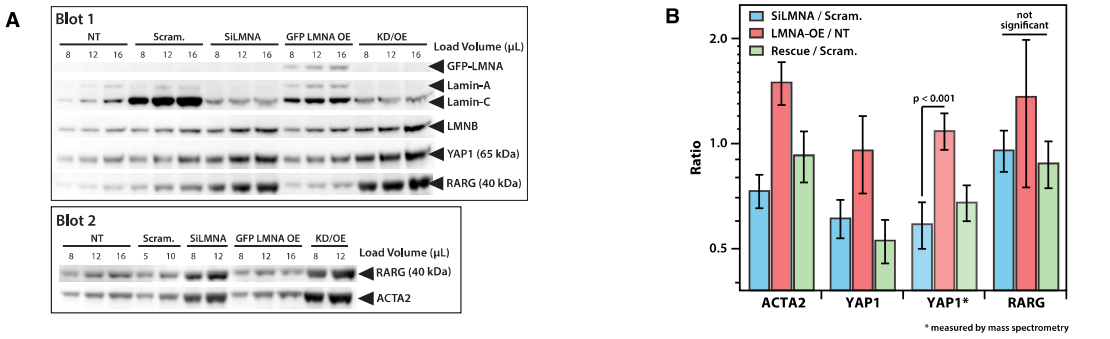

TFs regulated by lamin-A protein

C

gene	SREBF1	RAR, RXR	SRF	YAP1
ACSL1	719	139, 160		
FABP5	237			
LMNA	45	241, 1000		
CYP26A1		186, 1000		
RARB		888		
PTRF		400	192	
CALD1		165, 171, 276	237	
RUNX2	271	117, 177		
CRABP2		(89, 119)		
VCL	302	309	880	
ACTA2	41		(18)	
CTGF	30	459, 509	235	(11)
ANKRD1	27			(11)

YAP1 is mechanosensitive but non-monotonic *in vitro* and *in vivo*

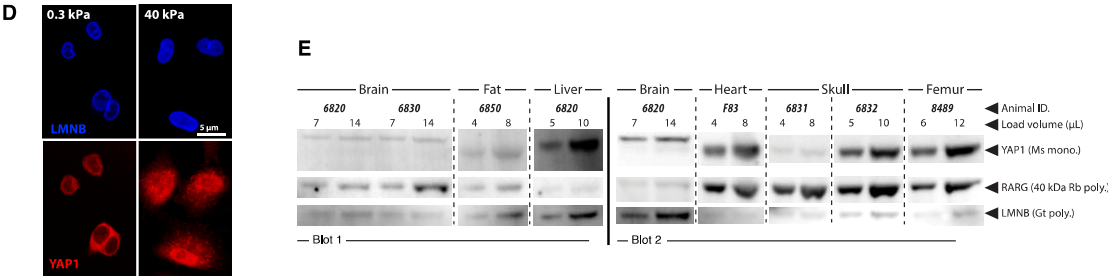

Fig. S12. Analyses of pathways involving lamin-A. (A) Immunoblots quantifying ACTA2 (SRF target), YAP1, RARG and other proteins during lamin-A over-expression ("GFP LAMIN OE"), knockdown ("SiLMNA") and a combined treatment rescue ("KD/OE"). (B) Bands in the blots were integrated and normalized to LMNB (quantified by mass spectrometry as described previously), which allowed comparison of proteins quantified by immunoblot alone (e.g. RARG) and those detected by both immunoblot and mass spectrometry (e.g. YAP1). While RARG shows no significant variation with KD or OE, consistent with transcript profiling, YAP1 protein changes with knockdown, suggesting more cytoplasmic protein that is prone to post translational modification by phosphorylation and degradation. ACTA2 also varies with lamin-A levels consistent with transcriptional profiling. (C) Summary of cluster scores from ENCODE database (*117*, *118*) indicating protein/gene interactions based on ChIP-seq experiments. Additional interactions of RARG in Su *et al.* and Durand *et al.* (*89*, *119*), SRF in Olson *et al.* (*18*), and YAP/TAZ in Dupont *et al.* (*11*). (D) High resolution confocal microscopy of YAP1 in A549 cells, cultured on substrates of increasing stiffness show increasing nuclear localization as reported by Dupont et al. (*11*). (E) Representative immunoblots of YAP1 and RARG in mouse tissue (quantified in Figs. 4K, 6A respectively).

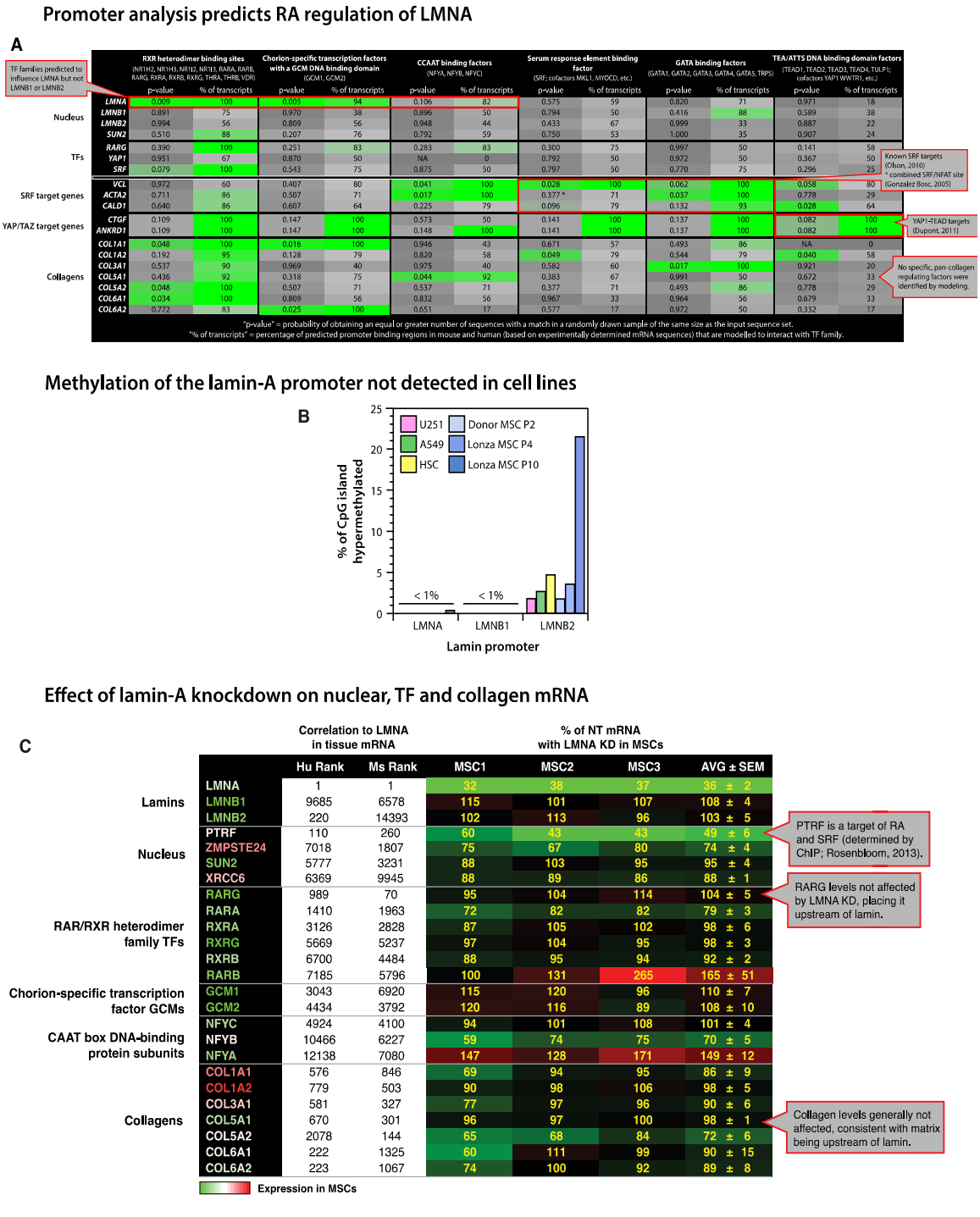

Fig. S13. Promoter analyses and pathways affected by lamin-A knockdown. (A) Analyses of transcription factor families modeled to bind the promoters of *LMNA* and other genes of interest. We catalogued these transcription factor (TF) families (groups that interact with homologous domains) together with transcription factors of possible mechanosensitive relevance (SRF, YAP1) and a few key target genes plus matrix genes (collagens). The list of potentially interesting TF families was optimized by selecting only those that bind the promoter of *LMNA*, which correlates with *E*, but not the promoters

of *LMNB1* or *LMNB2*, which do not correlate with *E*. In addition to RAR/RXR heterodimer TFs, the list included chorion-specific TFs, CCAAT binding factors. Previous investigations into the role of the RA in lamin regulation have shown it to suppress lamin expression in HL-60 human leukemic cells concomitantly with granulocytic differentiation (*55*), but to enhance expression in embryonic carcinoma cells through RA-responsive elements (RARE) (*54*). The promoter region of *RARB1* was found to be significantly methylated in familial partial lipodystrophy (FPLD) patients, a disorder caused by point mutations in lamin-A (*120*). Other pathways have previously been reported to be mechano-responsive but are not predicted to influence the lamins: the SRF pathway (*19*) drives a number of cytoskeletal targets (*18*) including VCL and CALD1 as well as α-smooth muscle actin (ACTA2) through a combined SRF/NFAT binding site (*121*). The YAP/TAZ pathway (*11*) is predicted to affect genes such as *ANKRD1* and *CTGF*. Modeling of TFs binding to collagen promoters does not suggest a single pan-collagen regulator, although the influence of retinoic acid factors cannot be fully discounted. The promoter analysis did not suggest factors from SRF or YAP/TAZ pathways as being key to either lamin-A or collagen regulation – indeed we found no strong candidate pathways for pan-collagen regulation. Evidence that MKL1/SRF regulates *COL1A2* (*122*) is undermined by the fact that the MKL1 knockout mouse is normal (*123*). (B) Methylation of CpG islands in the promoter regions of *LMNA* and *LMNB1* is negligible, but it is measurable for *LMNB2* and is highest in high passage MSCs (i.e. approaching senescence). A previous study of human *LMNA* promoter methylation using the bisulphite method of measurement found no statistical difference in methylation between healthy and laminopathic samples (*120*). The *LMNB2* promoter showed detectable levels of methylation but no correlation with what we might consider the source tissue stiffness. (C) Table of select transcripts after knockdown of *LMNA* in three different MSCs. Gene symbols are colored according to mRNA abundance in MSCs (green = low; red = high). Genes are ranked within each group based on Pearson correlations with *LMNA*/*Lmna* evaluated from microarray data from 11 soft tissues in human and 10 soft tissues in adult mouse (of 14985 gene annotations common to mouse and human).

LMNA promoter informatics

A

Top transcription factor matrix binding sites

	Family	Matrix	Query ID	S start	S end	Opt. threshold	Strand	Matrix sim.	Core sim.
RXR heterodimer binding sites (RXRA, RXRB, RXRG, NR1H2, NR1H3, NR1I2, NR1I3, RARA, RARB, RARG, THRA, THRB, VDR)	V$RXRF	V$VDR_RXR.01	GGCTGCAGGAGAAGGAGGACCTGCA	6142	6166	0.85	+	0.931	1
	V$RXRF	V$RAR_RXR.01	GACCTTCTGGGCTAGAGGGCAGAGC	5594	5570	0.78	-	0.84	0.808
	V$RXRF	V$VDR_RXR.05	GCCAGTGGTGGAAGAAGGGTGAGTC	5408	5432	0.79	+	0.831	0.762
	V$RXRF	V$VDR_RXR.04	CGGGAGTGGTGAGGAGGGGGAAGGA	5749	5725	0.79	-	0.823	0.786
	V$RXRF	V$RAR_RXR.01	CGGGGCTCGGGTCGAAGGACAGAGA	6008	5984	0.78	-	0.796	0.769
	V$RXRF	V$RAR_RXR.01	CTGCCCGCGGGGCAGGGGTCCCGGA	6040	6016	0.78	-	0.783	0.808
CCAAT binding factors (NFYA, NFYB, NFYC)	V$CAAT	V$ACAAT.01	ACCCCCAATGGATCT	5755	5769	0.83	+	0.865	1
	V$CAAT	V$NFY.02	GGTGCCCATCAGTGT	5447	5433	0.83	-	0.834	0.75
	V$CAAT	V$ACAAT.01	TCCACCACTGGCTCC	5419	5405	0.83	-	0.834	0.75
	V$CAAT	V$NFY.03	AGAGCCAAGGAGGGA	5574	5560	0.81	-	0.826	1
Chorion-specific transcription factors with a GCM DNA binding domain (GCM1, GCM2)	V$GCMF	V$GCM1.02	GCCCACCCGCATCAC	6125	6139	0.85	+	0.992	1
	V$GCMF	V$GCM1.02	CGCCACCCGCAGCGG	6083	6097	0.85	+	0.915	1
	V$GCMF	V$GCM1.01	GCTTGCCCCCATTGC	5613	5599	0.85	-	0.859	0.789
	V$GCMF	V$GCM1.03	CCCACCCCCAATGGA	5752	5766	0.83	+	0.849	1
	V$GCMF	V$GCM1.03	AGCTTCCCCTCTCTT	5680	5646	0.83	-	0.834	1

B

Modeled TF binding to LMNA promoter sequence

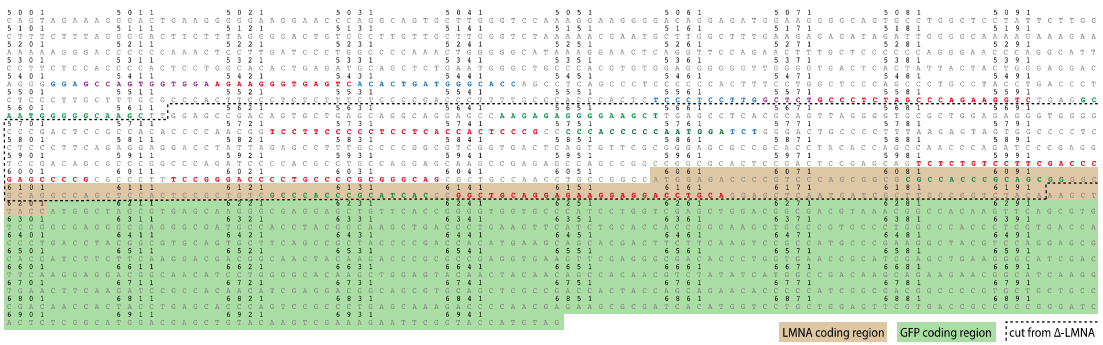

Fig. S14. Lamin-A promoter informatics and constructs. (A) Modeled binding positions of TFs that interact with the lamin-A promoter, but not with promoters of B-type lamins (using the Genomatix software suite, see Fig. S13A). (B) Lamin-A-GFP promoter-reporter construct, annotated with projected transcription factor binding sites and the region of deletion in the "Δ-*LMNA*" construct.

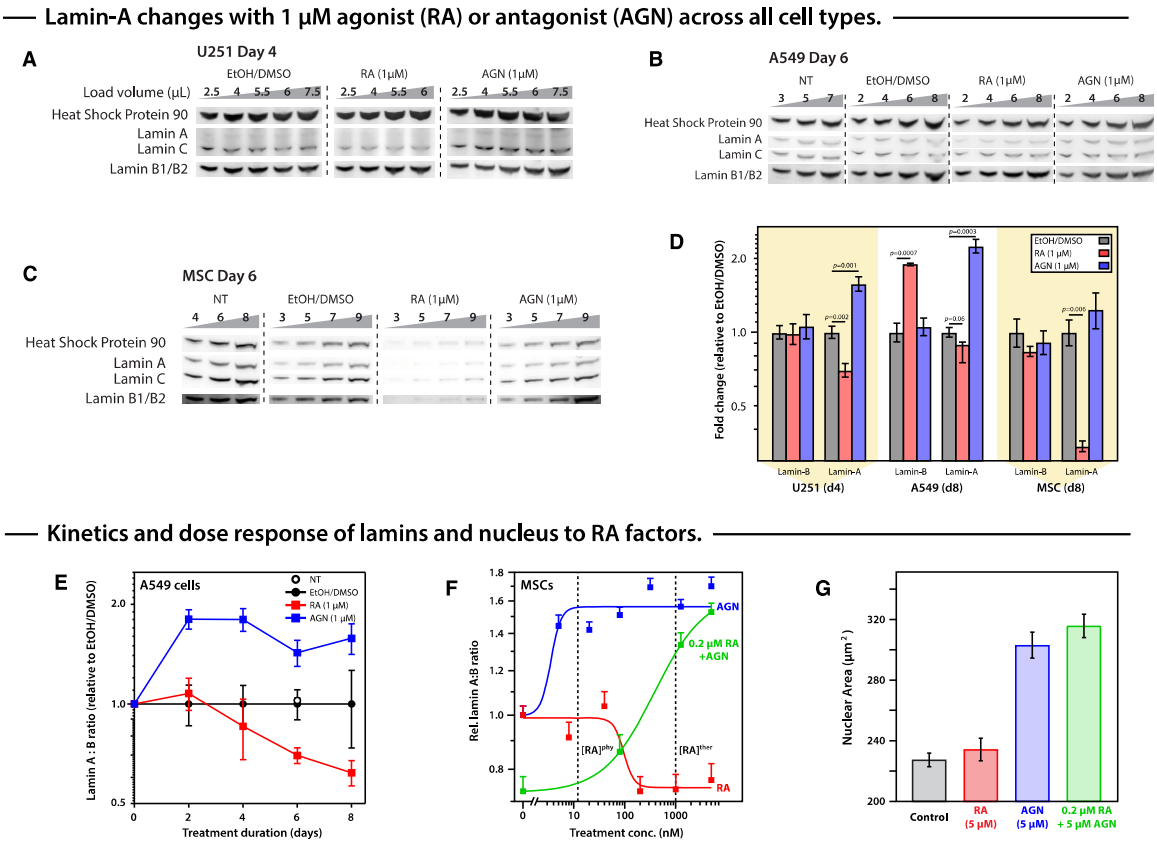

Fig. S15. Immunoblots quantify pharmacokinetics of RA and AGN on lamin levels in cultured cells. Immunoblots showing (A) U251s, (B) A549s and (C) MSCs. (D) Plot summarizing effects of RA and AGN observed in immunoblots (the latest time point in each cell line). In general, AGN treatment increases lamin-A level and RA decreases it. (E) Time resolved changes in lamin-A:B ratio during treatment of A549 cells with RA or AGN (from immunoblotting). (F) Dose response to RA and AGN, measured after 4 days in MSCs (from immunofluorescence, $N > 100$ cells). AGN treatment increases the lamin A:B ratio relative to endogenous levels (blue), while RA causes a decrease (red). Previous work confirms the K_d of AGN to be 2 - 3 nM, while that of RA is an order of magnitude higher (56). A rescue experiment recovered the suppressive effect of 200 nM RA through titration of AGN (green). $[RA]^{phys}$ and $[RA]^{ther}$ refer to physiological (~ 10 nM) and therapeutic (1 µM) levels of retinoic acid. (G) Changes in nuclear area in MSCs with the highest drug-treatment conditions. Nuclear area increases with the lamin-A:B ratio during AGN treatment.

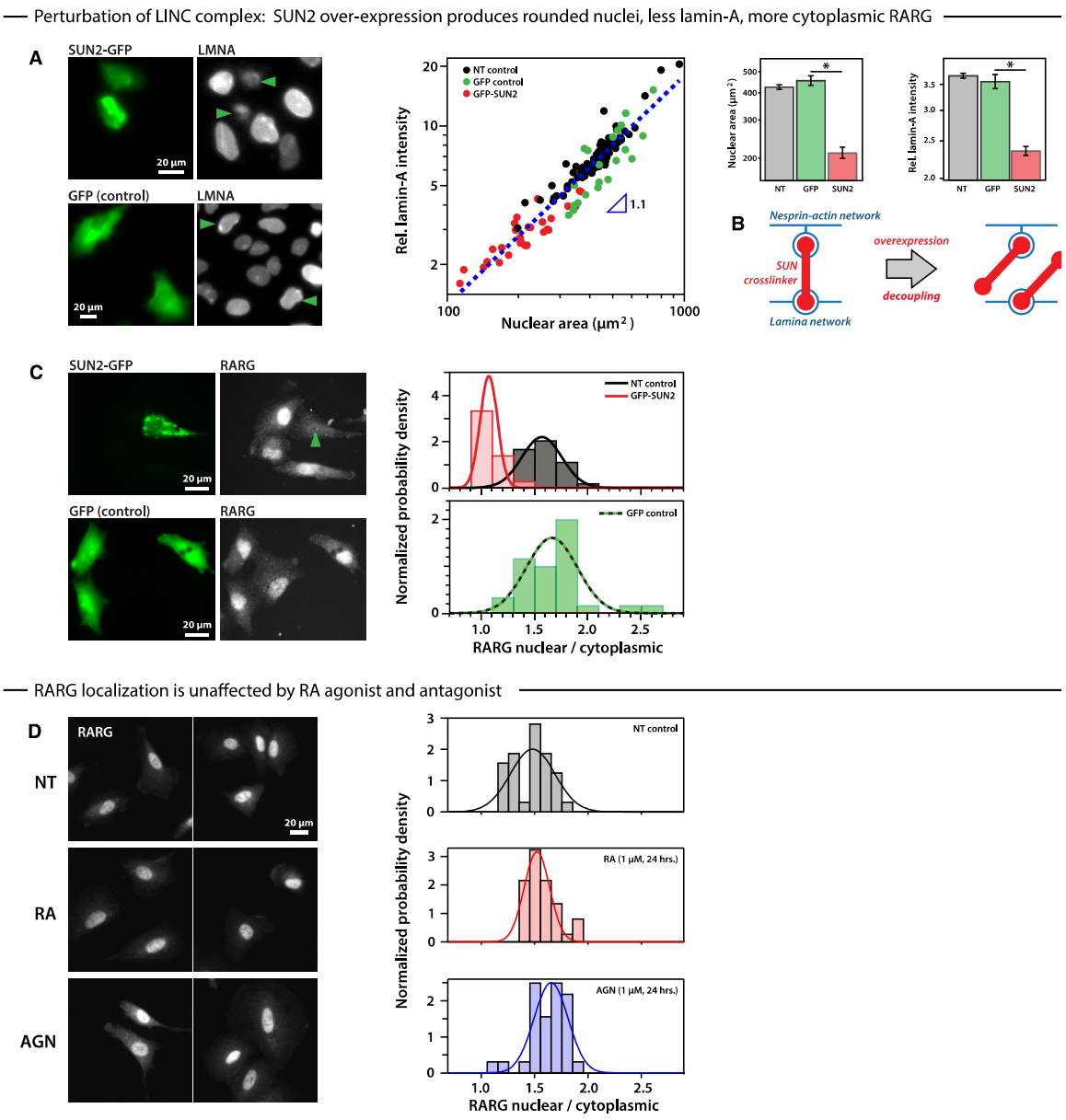

Fig. S16. SUN2 over-expression suppresses LMNA level and RARG location.

(A) Images of SUN2-GFP over-expression in A549 cells. Cells that are positive for SUN2-GFP have reduced lamin-A levels (green arrows). Image analysis shows that nuclear area and the amount of lamin-A are significantly reduced (* denotes $p << 0.001$). (B) Over-expression of SUN2-GFP is hypothesized to decouple the nucleus from the cytoskeleton by out-competing endogenous SUN2 for binding to KASH-domain containing proteins (i.e. nesprins). (C) Effect of over-expression of SUN2-GFP on RARG location. Cells positive for SUN2-GFP show reduced nuclear RARG (green arrow). Consistent with earlier observations, a reduction in lamin-A level decreases the amount of nuclear RARG (see Fig. 6C). (D) RARG location in A549 cells with SUN2-GFP over-expression. Staining for RARG shows that the TF is mostly nuclear, as expected for stiff substrate, and that the location is not affected by drug treatment.

Table S1. Tissue microelasticity values with references.

Tissue	Microelasticity, *E* (kPa)	References
Marrow	~ 0.2	Winer *et al.* 2009 (*101*)
Brain	0.4 (+ 0.6 / - 0.2)	Georges *et al.* 2006 (*9*)
Liver	1.35 ± 0.15	Georges *et al.* 2007 (*102*)
Kidney	2.6 ± 0.6	Wyss *et al.* 2011 (*103*)
Fat	3	Patel *et al.* 2005 (*104*)
Lung	6 ± 1.5	Lai-Fook and Hyatt 2000 (*105*)
Muscle	12	Engler, Sen *et al.* 2006 (*5*)
Heart	18 ± 2	Berry, Engler *et al.* 2006 (*106*)
Cartilage	24 ± 4	Guilak *et al.* 2005; Stolz *et al.* 2009 (*107, 108*)
Bone	35 ± 7	Engler, Sen *et al.* 2006 (*5*)

References

1. H. M. Frost, Bone “mass” and the “mechanostat”: A proposal. *Anat. Rec.* **219**, 1–9 (1987). doi:10.1002/ar.1092190104 Medline

2. V. Vogel, M. Sheetz, Local force and geometry sensing regulate cell functions. *Nat. Rev. Mol. Cell Biol.* **7**, 265–275 (2006). doi:10.1038/nrm1890 Medline

3. B. P. C. Chen, Y. S. Li, Y. Zhao, K. D. Chen, S. Li, J. Lao, S. Yuan, J. Y. Shyy, S. Chien, DNA microarray analysis of gene expression in endothelial cells in response to 24-h shear stress. *Physiol. Genomics* **7**, 55–63 (2001). Medline

4. D. E. Discher, P. Janmey, Y. L. Wang, Tissue cells feel and respond to the stiffness of their substrate. *Science* **310**, 1139–1143 (2005). doi:10.1126/science.1116995 Medline

5. A. J. Engler, S. Sen, H. L. Sweeney, D. E. Discher, Matrix elasticity directs stem cell lineage specification. *Cell* **126**, 677–689 (2006). doi:10.1016/j.cell.2006.06.044 Medline

6. R. J. Pelham, Jr., Y. Wang, Cell locomotion and focal adhesions are regulated by substrate flexibility. *Proc. Natl. Acad. Sci. U.S.A.* **94**, 13661–13665 (1997). doi:10.1073/pnas.94.25.13661 Medline

7. B. Trappmann, J. E. Gautrot, J. T. Connelly, D. G. Strange, Y. Li, M. L. Oyen, M. A. Cohen Stuart, H. Boehm, B. Li, V. Vogel, J. P. Spatz, F. M. Watt, W. T. Huck, Extracellular-matrix tethering regulates stem-cell fate. *Nat. Mater.* **11**, 642–649 (2012). doi:10.1038/nmat3339 Medline

8. S. Khetan, M. Guvendiren, W. R. Legant, D. M. Cohen, C. S. Chen, J. A. Burdick, Degradation-mediated cellular traction directs stem cell fate in covalently crosslinked three-dimensional hydrogels. *Nat. Mater.* **12**, 458–465 (2013). doi:10.1038/nmat3586 Medline

9. P. C. Georges, W. J. Miller, D. F. Meaney, E. S. Sawyer, P. A. Janmey, Matrices with compliance comparable to that of brain tissue select neuronal over glial growth in mixed cortical cultures. *Biophys. J.* **90**, 3012–3018 (2006). doi:10.1529/biophysj.105.073114 Medline

10. T. A. Ulrich, E. M. de Juan Pardo, S. Kumar, The mechanical rigidity of the extracellular matrix regulates the structure, motility, and proliferation of glioma cells. *Cancer Res.* **69**, 4167–4174 (2009). doi:10.1158/0008-5472.CAN-08-4859 Medline

11. S. Dupont, L. Morsut, M. Aragona, E. Enzo, S. Giulitti, M. Cordenonsi, F. Zanconato, J. Le Digabel, M. Forcato, S. Bicciato, N. Elvassore, S. Piccolo, Role of YAP/TAZ in mechanotransduction. *Nature* **474**, 179–183 (2011). doi:10.1038/nature10137 Medline

12. A. J. Engler, M. A. Griffin, S. Sen, C. G. Bönnemann, H. L. Sweeney, D. E. Discher, Myotubes differentiate optimally on substrates with tissue-like stiffness: Pathological implications for soft or stiff microenvironments. *J. Cell Biol.* **166**, 877–887 (2004). doi:10.1083/jcb.200405004 Medline

13. A. J. Engler, C. Carag-Krieger, C. P. Johnson, M. Raab, H. Y. Tang, D. W. Speicher, J. W. Sanger, J. M. Sanger, D. E. Discher, Embryonic cardiomyocytes beat best on a matrix

with heart-like elasticity: Scar-like rigidity inhibits beating. *J. Cell Sci.* **121**, 3794–3802 (2008). doi:10.1242/jcs.029678 Medline

14. P. M. Gilbert, K. L. Havenstrite, K. E. Magnusson, A. Sacco, N. A. Leonardi, P. Kraft, N. K. Nguyen, S. Thrun, M. P. Lutolf, H. M. Blau, Substrate elasticity regulates skeletal muscle stem cell self-renewal in culture. *Science* **329**, 1078–1081 (2010). doi:10.1126/science.1191035 Medline

15. H. J. Kong, T. R. Polte, E. Alsberg, D. J. Mooney, FRET measurements of cell-traction forces and nano-scale clustering of adhesion ligands varied by substrate stiffness. *Proc. Natl. Acad. Sci. U.S.A.* **102**, 4300–4305 (2005). doi:10.1073/pnas.0405873102 Medline

16. N. Huebsch, P. R. Arany, A. S. Mao, D. Shvartsman, O. A. Ali, S. A. Bencherif, J. Rivera-Feliciano, D. J. Mooney, Harnessing traction-mediated manipulation of the cell/matrix interface to control stem-cell fate. *Nat. Mater.* **9**, 518–526 (2010). doi:10.1038/nmat2732 Medline

17. B. Zhao, K. Tumaneng, K. L. Guan, The Hippo pathway in organ size control, tissue regeneration and stem cell self-renewal. *Nat. Cell Biol.* **13**, 877–883 (2011). doi:10.1038/ncb2303 Medline

18. E. N. Olson, A. Nordheim, Linking actin dynamics and gene transcription to drive cellular motile functions. *Nat. Rev. Mol. Cell Biol.* **11**, 353–365 (2010). doi:10.1038/nrm2890 Medline

19. J. T. Connelly, J. E. Gautrot, B. Trappmann, D. W. Tan, G. Donati, W. T. Huck, F. M. Watt, Actin and serum response factor transduce physical cues from the microenvironment to regulate epidermal stem cell fate decisions. *Nat. Cell Biol.* **12**, 711–718 (2010). doi:10.1038/ncb2074 Medline

20. J. D. Pajerowski, K. N. Dahl, F. L. Zhong, P. J. Sammak, D. E. Discher, Physical plasticity of the nucleus in stem cell differentiation. *Proc. Natl. Acad. Sci. U.S.A.* **104**, 15619–15624 (2007). doi:10.1073/pnas.0702576104 Medline

21. J. Lammerding, L. G. Fong, J. Y. Ji, K. Reue, C. L. Stewart, S. G. Young, R. T. Lee, Lamins A and C but not lamin B1 regulate nuclear mechanics. *J. Biol. Chem.* **281**, 25768–25780 (2006). doi:10.1074/jbc.M513511200 Medline

22. W. H. De Vos, F. Houben, M. Kamps, A. Malhas, F. Verheyen, J. Cox, E. M. Manders, V. L. Verstraeten, M. A. van Steensel, C. L. Marcelis, A. van den Wijngaard, D. J. Vaux, F. C. Ramaekers, J. L. Broers, Repetitive disruptions of the nuclear envelope invoke temporary loss of cellular compartmentalization in laminopathies. *Hum. Mol. Genet.* **20**, 4175–4186 (2011). doi:10.1093/hmg/ddr344 Medline

23. H. Herrmann, S. V. Strelkov, P. Burkhard, U. Aebi, Intermediate filaments: Primary determinants of cell architecture and plasticity. *J. Clin. Invest.* **119**, 1772–1783 (2009). doi:10.1172/JCI38214 Medline

24. T. Shimi, K. Pfleghaar, S. Kojima, C. G. Pack, I. Solovei, A. E. Goldman, S. A. Adam, D. K. Shumaker, M. Kinjo, T. Cremer, R. D. Goldman, The A- and B-type nuclear lamin networks: Microdomains involved in chromatin organization and transcription. *Genes Dev.* **22**, 3409–3421 (2008). doi:10.1101/gad.1735208 Medline

25. N. Wang, J. D. Tytell, D. E. Ingber, Mechanotransduction at a distance: Mechanically coupling the extracellular matrix with the nucleus. *Nat. Rev. Mol. Cell Biol.* **10**, 75–82 (2009). doi:10.1038/nrm2594 Medline

26. G. V. Shivashankar, Mechanosignaling to the cell nucleus and gene regulation. *Annu. Rev. Biophys.* **40**, 361–378 (2011). doi:10.1146/annurev-biophys-042910-155319 Medline

27. J. L. V. Broers, B. M. Machiels, H. J. Kuijpers, F. Smedts, R. van den Kieboom, Y. Raymond, F. C. Ramaekers, A- and B-type lamins are differentially expressed in normal human tissues. *Histochem. Cell Biol.* **107**, 505–517 (1997). doi:10.1007/s004180050138 Medline

28. C. Storm, J. J. Pastore, F. C. MacKintosh, T. C. Lubensky, P. A. Janmey, Nonlinear elasticity in biological gels. *Nature* **435**, 191–194 (2005). doi:10.1038/nature03521 Medline

29. M. L. Gardel, J. H. Shin, F. C. MacKintosh, L. Mahadevan, P. Matsudaira, D. A. Weitz, Elastic behavior of cross-linked and bundled actin networks. *Science* **304**, 1301–1305 (2004). doi:10.1126/science.1095087 Medline

30. T. Kim, W. Hwang, H. Lee, R. D. Kamm, Computational analysis of viscoelastic properties of crosslinked actin networks. *PLOS Comput. Biol.* **5**, e1000439 (2009). doi:10.1371/journal.pcbi.1000439 Medline

31. G. Strobl, *The Physics of Polymers: Concepts for Understanding their Structure and Behavior* (Springer, New York, 2007).

32. H. J. Worman, Nuclear lamins and laminopathies. *J. Pathol.* **226**, 316–325 (2012). doi:10.1002/path.2999 Medline

33. D. Tunnah, C. A. Sewry, D. Vaux, E. C. Schirmer, G. E. Morris, The apparent absence of lamin B1 and emerin in many tissue nuclei is due to epitope masking. *J. Mol. Histol.* **36**, 337–344 (2005). doi:10.1007/s10735-005-9004-7 Medline

34. Y. Kim, A. A. Sharov, K. McDole, M. Cheng, H. Hao, C. M. Fan, N. Gaiano, M. S. Ko, Y. Zheng, Mouse B-type lamins are required for proper organogenesis but not by embryonic stem cells. *Science* **334**, 1706–1710 (2011). doi:10.1126/science.1211222 Medline

35. Y. L. Yang, L. M. Leone, L. J. Kaufman, Elastic moduli of collagen gels can be predicted from two-dimensional confocal microscopy. *Biophys. J.* **97**, 2051–2060 (2009). doi:10.1016/j.bpj.2009.07.035 Medline

36. C. P. Johnson, H. Y. Tang, C. Carag, D. W. Speicher, D. E. Discher, Forced unfolding of proteins within cells. *Science* **317**, 663–666 (2007). doi:10.1126/science.1139857 Medline

37. I. Krimm, C. Ostlund, B. Gilquin, J. Couprie, P. Hossenlopp, J. P. Mornon, G. Bonne, J. C. Courvalin, H. J. Worman, S. Zinn-Justin, The Ig-like structure of the C-terminal domain of lamin A/C, mutated in muscular dystrophies, cardiomyopathy, and partial lipodystrophy. *Structure* **10**, 811–823 (2002). doi:10.1016/S0969-2126(02)00777-3 Medline

38. R. D. Goldman, Y. Gruenbaum, R. D. Moir, D. K. Shumaker, T. P. Spann, Nuclear lamins: Building blocks of nuclear architecture. *Genes Dev.* **16**, 533–547 (2002). doi:10.1101/gad.960502 Medline

39. J. Bertacchini, F. Beretti, V. Cenni, M. Guida, F. Gibellini, L. Mediani, O. Marin, N. M. Maraldi, A. de Pol, G. Lattanzi, L. Cocco, S. Marmiroli, The protein kinase Akt/PKB regulates both prelamin A degradation and Lmna gene expression. *FASEB J.* **27**, 2145–2155 (2013). doi:10.1096/fj.12-218214 Medline

40. K. A. Moore, I. R. Lemischka, Stem cells and their niches. *Science* **311**, 1880–1885 (2006). doi:10.1126/science.1110542 Medline

41. R. Akter, D. Rivas, G. Geneau, H. Drissi, G. Duque, Effect of lamin A/C knockdown on osteoblast differentiation and function. *J. Bone Miner. Res.* **24**, 283–293 (2009). doi:10.1359/jbmr.081010 Medline

42. P. Scaffidi, T. Misteli, Lamin A-dependent misregulation of adult stem cells associated with accelerated ageing. *Nat. Cell Biol.* **10**, 452–459 (2008). doi:10.1038/ncb1708 Medline

43. M. Raab, J. Swift, P. C. Dingal, P. Shah, J. W. Shin, D. E. Discher, Crawling from soft to stiff matrix polarizes the cytoskeleton and phosphoregulates myosin-II heavy chain. *J. Cell Biol.* **199**, 669–683 (2012). doi:10.1083/jcb.201205056 Medline

44. P. P. Y. Lu, N. Ramanan, Serum response factor is required for cortical axon growth but is dispensable for neurogenesis and neocortical lamination. *J. Neurosci.* **31**, 16651–16664 (2011). doi:10.1523/JNEUROSCI.3015-11.2011 Medline

45. J. Chen, K. Yuan, X. Mao, J. M. Miano, H. Wu, Y. Chen, Serum response factor regulates bone formation via IGF-1 and Runx2 signals. *J. Bone Miner. Res.* **27**, 1659–1668 (2012). doi:10.1002/jbmr.1607 Medline

46. C. Baarlink, H. Wang, R. Grosse, Nuclear actin network assembly by formins regulates the SRF coactivator MAL. *Science* **340**, 864–867 (2013). doi:10.1126/science.1235038 Medline

47. D. N. Simon, M. S. Zastrow, K. L. Wilson, Direct actin binding to A- and B-type lamin tails and actin filament bundling by the lamin A tail. *Nucleus* **1**, 264–272 (2010). doi:10.4161/nucl.1.3.11799 Medline

48. D. N. Simon, K. L. Wilson, The nucleoskeleton as a genome-associated dynamic ‘network of networks’. *Nat. Rev. Mol. Cell Biol.* **12**, 695–708 (2011). doi:10.1038/nrm3207 Medline

49. C. Y. Ho, D. E. Jaalouk, M. K. Vartiainen, J. Lammerding, Lamin A/C and emerin regulate MKL1-SRF activity by modulating actin dynamics. *Nature* **497**, 507–511 (2013). doi:10.1038/nature12105 Medline

50. D. J. Lloyd, R. C. Trembath, S. Shackleton, A novel interaction between lamin A and SREBP1: Implications for partial lipodystrophy and other laminopathies. *Hum. Mol. Genet.* **11**, 769–777 (2002). doi:10.1093/hmg/11.7.769 Medline

51. J.-T. Ayala-Sumuano, C. Velez-Delvalle, A. Beltrán-Langarica, M. Marsch-Moreno, J. Cerbón-Solorzano, W. Kuri-Harcuch, Srebf1a is a key regulator of transcriptional control for adipogenesis. *Sci. Rep.* **1**, 178 (2011). doi:10.1038/srep00178 Medline

52. X. Ma, X. Ren, P. Han, S. Hu, J. Wang, J. Yin, SiRNA against Fabp5 induces 3T3-L1 cells apoptosis during adipocytic induction. *Mol. Biol. Rep.* **37**, 4003–4011 (2010). doi:10.1007/s11033-010-0059-5 Medline

53. B. Zhao, X. Ye, J. Yu, L. Li, W. Li, S. Li, J. Yu, J. D. Lin, C. Y. Wang, A. M. Chinnaiyan, Z. C. Lai, K. L. Guan, TEAD mediates YAP-dependent gene induction and growth control. *Genes Dev.* **22**, 1962–1971 (2008). doi:10.1101/gad.1664408 Medline

54. K. Okumura, Y. Hosoe, N. Nakajima, c-Jun and Sp1 family are critical for retinoic acid induction of the lamin A/C retinoic acid-responsive element. *Biochem. Biophys. Res. Commun.* **320**, 487–492 (2004). doi:10.1016/j.bbrc.2004.05.191 Medline

55. A. L. Olins, H. Herrmann, P. Lichter, M. Kratzmeier, D. Doenecke, D. E. Olins, Nuclear envelope and chromatin compositional differences comparing undifferentiated and retinoic acid- and phorbol ester-treated HL-60 cells. *Exp. Cell Res.* **268**, 115–127 (2001). doi:10.1006/excr.2001.5269 Medline

56. C. Agarwal, R. A. S. Chandraratna, A. T. Johnson, E. A. Rorke, R. L. Eckert, AGN193109 is a highly effective antagonist of retinoid action in human ectocervical epithelial cells. *J. Biol. Chem.* **271**, 12209–12212 (1996). doi:10.1074/jbc.271.21.12209 Medline

57. K. Shimono, W. E. Tung, C. Macolino, A. H. Chi, J. H. Didizian, C. Mundy, R. A. Chandraratna, Y. Mishina, M. Enomoto-Iwamoto, M. Pacifici, M. Iwamoto, Potent inhibition of heterotopic ossification by nuclear retinoic acid receptor-γ agonists. *Nat. Med.* **17**, 454–460 (2011). doi:10.1038/nm.2334 Medline

58. W. Zhang, Q. Yan, Y. S. Zeng, X. B. Zhang, Y. Xiong, J. M. Wang, S. J. Chen, Y. Li, I. C. Bruce, W. Wu, Implantation of adult bone marrow-derived mesenchymal stem cells transfected with the neurotrophin-3 gene and pretreated with retinoic acid in completely transected spinal cord. *Brain Res.* **1359**, 256–271 (2010). doi:10.1016/j.brainres.2010.08.072 Medline

59. T. Sullivan, D. Escalante-Alcalde, H. Bhatt, M. Anver, N. Bhat, K. Nagashima, C. L. Stewart, B. Burke, Loss of A-type lamin expression compromises nuclear envelope integrity leading to muscular dystrophy. *J. Cell Biol.* **147**, 913–920 (1999). doi:10.1083/jcb.147.5.913 Medline

60. D. Jahn, S. Schramm, M. Schnölzer, C. J. Heilmann, C. G. de Koster, W. Schütz, R. Benavente, M. Alsheimer, A truncated lamin A in the *Lmna*$^{-/-}$ mouse line: Implications for the understanding of laminopathies. *Nucleus* **3**, 463–474 (2012). doi:10.4161/nucl.21676 Medline

61. N. Kubben, J. W. Voncken, G. Konings, M. van Weeghel, M. M. van den Hoogenhof, M. Gijbels, A. van Erk, K. Schoonderwoerd, B. van den Bosch, V. Dahlmans, C. Calis, S. M. Houten, T. Misteli, Y. M. Pinto, Post-natal myogenic and adipogenic developmental: Defects and metabolic impairment upon loss of A-type lamins. *Nucleus* **2**, 195–207 (2011). doi:10.4161/nucl.2.3.15731 Medline

62. F. Haque, D. Mazzeo, J. T. Patel, D. T. Smallwood, J. A. Ellis, C. M. Shanahan, S. Shackleton, Mammalian SUN protein interaction networks at the inner nuclear membrane and their role in laminopathy disease processes. *J. Biol. Chem.* **285**, 3487–3498 (2010). doi:10.1074/jbc.M109.071910 Medline

63. M. Murakami, M. Nakagawa, E. N. Olson, O. Nakagawa, A WW domain protein TAZ is a critical coactivator for TBX5, a transcription factor implicated in Holt-Oram syndrome.

Proc. Natl. Acad. Sci. U.S.A. **102**, 18034–18039 (2005). doi:10.1073/pnas.0509109102 Medline

64. B. Zhao, X. Wei, W. Li, R. S. Udan, Q. Yang, J. Kim, J. Xie, T. Ikenoue, J. Yu, L. Li, P. Zheng, K. Ye, A. Chinnaiyan, G. Halder, Z. C. Lai, K. L. Guan, Inactivation of YAP oncoprotein by the Hippo pathway is involved in cell contact inhibition and tissue growth control. *Genes Dev.* **21**, 2747–2761 (2007). doi:10.1101/gad.1602907 Medline

65. C. Franz, R. Walczak, S. Yavuz, R. Santarella, M. Gentzel, P. Askjaer, V. Galy, M. Hetzer, I. W. Mattaj, W. Antonin, MEL-28/ELYS is required for the recruitment of nucleoporins to chromatin and postmitotic nuclear pore complex assembly. *EMBO Rep.* **8**, 165–172 (2007). doi:10.1038/sj.embor.7400889 Medline

66. J. M. Zullo, I. A. Demarco, R. Piqué-Regi, D. J. Gaffney, C. B. Epstein, C. J. Spooner, T. R. Luperchio, B. E. Bernstein, J. K. Pritchard, K. L. Reddy, H. Singh, DNA sequence-dependent compartmentalization and silencing of chromatin at the nuclear lamina. *Cell* **149**, 1474–1487 (2012). doi:10.1016/j.cell.2012.04.035 Medline

67. W. Meuleman, D. Peric-Hupkes, J. Kind, J. B. Beaudry, L. Pagie, M. Kellis, M. Reinders, L. Wessels, B. van Steensel, Constitutive nuclear lamina-genome interactions are highly conserved and associated with A/T-rich sequence. *Genome Res.* **23**, 270–280 (2013). doi:10.1101/gr.141028.112 Medline

68. T. Dechat, K. Pfleghaar, K. Sengupta, T. Shimi, D. K. Shumaker, L. Solimando, R. D. Goldman, Nuclear lamins: Major factors in the structural organization and function of the nucleus and chromatin. *Genes Dev.* **22**, 832–853 (2008). doi:10.1101/gad.1652708 Medline

69. B. L. Mahaney, K. Meek, S. P. Lees-Miller, Repair of ionizing radiation-induced DNA double-strand breaks by non-homologous end-joining. *Biochem. J.* **417**, 639–650 (2009). doi:10.1042/BJ20080413 Medline

70. N. Kubben, J. W. Voncken, J. Demmers, C. Calis, G. van Almen, Y. Pinto, T. Misteli, Identification of differential protein interactors of lamin A and progerin. *Nucleus* **1**, 513–525 (2010). Medline

71. R. D. A. M. Alves, J. A. Demmers, K. Bezstarosti, B. C. van der Eerden, J. A. Verhaar, M. Eijken, J. P. van Leeuwen, Unraveling the human bone microenvironment beyond the classical extracellular matrix proteins: A human bone protein library. *J. Proteome Res.* **10**, 4725–4733 (2011). doi:10.1021/pr200522n Medline

72. S. K. Zaidi, A. J. Sullivan, R. Medina, Y. Ito, A. J. van Wijnen, J. L. Stein, J. B. Lian, G. S. Stein, Tyrosine phosphorylation controls Runx2-mediated subnuclear targeting of YAP to repress transcription. *EMBO J.* **23**, 790–799 (2004). doi:10.1038/sj.emboj.7600073 Medline

73. J. H. Hong, E. S. Hwang, M. T. McManus, A. Amsterdam, Y. Tian, R. Kalmukova, E. Mueller, T. Benjamin, B. M. Spiegelman, P. A. Sharp, N. Hopkins, M. B. Yaffe, TAZ, a transcriptional modulator of mesenchymal stem cell differentiation. *Science* **309**, 1074–1078 (2005). doi:10.1126/science.1110955 Medline

74. Y. K. Hayashi, C. Matsuda, M. Ogawa, K. Goto, K. Tominaga, S. Mitsuhashi, Y. E. Park, I. Nonaka, N. Hino-Fukuyo, K. Haginoya, H. Sugano, I. Nishino, Human PTRF mutations

cause secondary deficiency of caveolins resulting in muscular dystrophy with generalized lipodystrophy. *J. Clin. Invest.* **119**, 2623–2633 (2009). doi:10.1172/JCI38660 Medline

75. J.-W. Shin, J. Swift, I. Ivanovska, K. R. Spinler, A. Buxboim, D. E. Discher, Mechanobiology of bone marrow stem cells: From myosin-II forces to compliance of matrix and nucleus in cell forms and fates. *Differentiation* **2013**, 10.1016/j.diff.2013.05.001 (2013). doi:10.1016/j.diff.2013.05.001 Medline

76. J. S. Chamberlain, J. Metzger, M. Reyes, D. W. Townsend, J. A. Faulkner, Dystrophin-deficient mdx mice display a reduced life span and are susceptible to spontaneous rhabdomyosarcoma. *FASEB J.* **21**, 2195–2204 (2007). doi:10.1096/fj.06-7353com Medline

77. H. Zhang, F. Burrows, Targeting multiple signal transduction pathways through inhibition of Hsp90. *J. Mol. Med.* **82**, 488–499 (2004). doi:10.1007/s00109-004-0549-9 Medline

78. B. R. Eisenberg, A. M. Kuda, Stereological analysis of mammalian skeletal muscle. II. White vastus muscle of the adult guinea pig. *J. Ultrastruct. Res.* **51**, 176–187 (1975). doi:10.1016/S0022-5320(75)80146-8 Medline

79. J. Hope, Stereological analysis of the ultrastructure of liver parenchymal cells during pregnancy and lactation. *J. Ultrastruct. Res.* **33**, 292–305 (1970). doi:10.1016/S0022-5320(70)90023-7 Medline

80. A. Mattout, A. Biran, E. Meshorer, Global epigenetic changes during somatic cell reprogramming to iPS cells. *J. Mol. Cell Biol.* **3**, 341–350 (2011). doi:10.1093/jmcb/mjr028 Medline

81. W. Wang, J. Yang, H. Liu, D. Lu, X. Chen, Z. Zenonos, L. S. Campos, R. Rad, G. Guo, S. Zhang, A. Bradley, P. Liu, Rapid and efficient reprogramming of somatic cells to induced pluripotent stem cells by retinoic acid receptor gamma and liver receptor homolog 1. *Proc. Natl. Acad. Sci. U.S.A.* **108**, 18283–18288 (2011). doi:10.1073/pnas.1100893108 Medline

82. K. Beck, B. Brodsky, Supercoiled protein motifs: The collagen triple-helix and the alpha-helical coiled coil. *J. Struct. Biol.* **122**, 17–29 (1998). doi:10.1006/jsbi.1998.3965 Medline

83. B. P. Flynn, A. P. Bhole, N. Saeidi, M. Liles, C. A. Dimarzio, J. W. Ruberti, Mechanical strain stabilizes reconstituted collagen fibrils against enzymatic degradation by mammalian collagenase matrix metalloproteinase 8 (MMP-8). *PLoS ONE* **5**, e12337 (2010). doi:10.1371/journal.pone.0012337 Medline

84. D. K. Shumaker, R. I. Lopez-Soler, S. A. Adam, H. Herrmann, R. D. Moir, T. P. Spann, R. D. Goldman, Functions and dysfunctions of the nuclear lamin Ig-fold domain in nuclear assembly, growth, and Emery-Dreifuss muscular dystrophy. *Proc. Natl. Acad. Sci. U.S.A.* **102**, 15494–15499 (2005). doi:10.1073/pnas.0507612102 Medline

85. R. Heald, F. McKeon, Mutations of phosphorylation sites in lamin A that prevent nuclear lamina disassembly in mitosis. *Cell* **61**, 579–589 (1990). doi:10.1016/0092-8674(90)90470-Y Medline

86. Y. Sawada, M. Tamada, B. J. Dubin-Thaler, O. Cherniavskaya, R. Sakai, S. Tanaka, M. P. Sheetz, Force sensing by mechanical extension of the Src family kinase substrate p130Cas. *Cell* **127**, 1015–1026 (2006). doi:10.1016/j.cell.2006.09.044 Medline

87. A. I. Lamond, Nucleolar isolation protocol (LamondLab.com, Dundee, Scotland, 2009) http://www.lamondlab.com/f7nucleolarprotocol.htm

88. J. W. Shin, J. Swift, K. R. Spinler, D. E. Discher, Myosin-II inhibition and soft 2D matrix maximize multinucleation and cellular projections typical of platelet-producing megakaryocytes. *Proc. Natl. Acad. Sci. U.S.A.* **108**, 11458–11463 (2011). doi:10.1073/pnas.1017474108 Medline

89. D. Su, L. J. Gudas, Gene expression profiling elucidates a specific role for RARgamma in the retinoic acid-induced differentiation of F9 teratocarcinoma stem cells. *Biochem. Pharmacol.* **75**, 1129–1160 (2008). doi:10.1016/j.bcp.2007.11.006 Medline

90. I. D. Welch, M. F. Cowan, F. Beier, T. M. Underhill, The retinoic acid binding protein CRABP2 is increased in murine models of degenerative joint disease. *Arthritis Res. Ther.* **11**, R14 (2009). doi:10.1186/ar2604 Medline

91. S. L. Yu, L. Levi, R. Siegel, N. Noy, Retinoic acid induces neurogenesis by activating both retinoic acid receptors (RARs) and peroxisome proliferator-activated receptor β/δ (PPARβ/δ). *J. Biol. Chem.* **287**, 42195–42205 (2012). doi:10.1074/jbc.M112.410381 Medline

92. H. A. Barnes, *Handbook of Elementary Rheology* (University of Wales, Institute of Non-Newtonian Fluid Mechanics, Cardiff, 2000).

93. M. Rubinstein, R. Colby, *Polymer Physics* (Oxford University Press, Oxford, 2003).

94. Y. Heo, R. G. Larson, The scaling of zero-shear viscosities of semidilute polymer solutions with concentration. *J. Rheol.* **49**, 1117 (2005). doi:10.1122/1.1993595

95. S. M. Elbashir *et al*., Duplexes of 21-nucleotide RNAs mediate RNA interference in cultured mammalian cells. *Nature* **411**, 494 (2001). doi:10.1038/35078107 Medline

96. B. C. Baumann *et al*., Enhancing the efficacy of drug-loaded nanocarriers against brain tumors by targeted radiation therapy. *Oncotarget* **4**, 64 (2013). Medline

97. P. L. Rodriguez *et al*., Minimal “Self” peptides that inhibit phagocytic clearance and enhance delivery of nanoparticles. *Science* **339**, 971 (2013). doi:10.1126/science.1229568 Medline

98. K. N. Dahl, A. J. Engler, J. D. Pajerowski, D. E. Discher, Power-law rheology of isolated nuclei with deformation mapping of nuclear substructures. *Biophys. J.* **89**, 2855 (2005). doi:10.1529/biophysj.105.062554 Medline

99. A. Buxboim, K. Rajagopal, A. E. X. Brown, D. E. Discher, How deeply cells feel: Methods for thin gels. *J. Phys. Condens. Matter* **22**, 194116 (2010). doi:10.1088/0953-8984/22/19/194116 Medline

100. K. Cartharius *et al*., MatInspector and beyond: Promoter analysis based on transcription factor binding sites. *Bioinformatics* **21**, 2933 (2005). doi:10.1093/bioinformatics/bti473 Medline

101. J. P. Winer, P. A. Janmey, M. E. McCormick, M. Funaki, Bone marrow-derived human mesenchymal stem cells become quiescent on soft substrates but remain responsive to chemical or mechanical stimuli. *Tissue Eng. Part A* **15**, 147 (2009). doi:10.1089/ten.tea.2007.0388 Medline

102. P. C. Georges *et al*., Increased stiffness of the rat liver precedes matrix deposition: implications for fibrosis. *Am. J. Physiol. Gastrointest. Liver Physiol.* **293**, G1147 (2007). doi:10.1152/ajpgi.00032.2007 Medline

103. H. M. Wyss *et al*., Biophysical properties of normal and diseased renal glomeruli. *Am. J. Physiol. Cell Physiol.* **300**, C397 (2011). doi:10.1152/ajpcell.00438.2010 Medline

104. P. N. Patel, A. S. Gobin, J. L. West, C. W. Patrick, Jr., Poly(ethylene glycol) hydrogel system supports preadipocyte viability, adhesion, and proliferation. *Tissue Eng.* **11**, 1498 (2005). doi:10.1089/ten.2005.11.1498 Medline

105. S. J. Lai-Fook, R. E. Hyatt, Effects of age on elastic moduli of human lungs. *J. Appl. Physiol.* **89**, 163 (2000). Medline

106. M. F. Berry *et al*., Mesenchymal stem cell injection after myocardial infarction improves myocardial compliance. *Am. J. Physiol. Heart Circ. Physiol.* **290**, H2196 (2006). doi:10.1152/ajpheart.01017.2005 Medline

107. F. Guilak, L. G. Alexopoulos, M. A. Haider, H. P. Ting-Beall, L. A. Setton, Zonal uniformity in mechanical properties of the chondrocyte pericellular matrix: micropipette aspiration of canine chondrons isolated by cartilage homogenization. *Ann. Biomed. Eng.* **33**, 1312 (2005). doi:10.1007/s10439-005-4479-7 Medline

108. M. Stolz *et al*., Early detection of aging cartilage and osteoarthritis in mice and patient samples using atomic force microscopy. *Nat. Nanotechnol.* **4**, 186 (2009). doi:10.1038/nnano.2008.410 Medline

109. H. J. Jung, C. Coffinier, Y. Choe, A. P. Beigneux, B. S. Davies, S. H. Yang, R. H. Barnes, 2nd, J. Hong, T. Sun, S. J. Pleasure, S. G. Young, L. G. Fong, Regulation of prelamin A but not lamin C by miR-9, a brain-specific microRNA. *Proc. Natl. Acad. Sci. U.S.A.* **109**, E423–E431 (2012). doi:10.1073/pnas.1111780109 Medline

110. J. W. Lee, H. K. Kim, Y. M. Han, J. H. Kim, Pyruvate kinase isozyme type M2 (PKM2) interacts and cooperates with Oct-4 in regulating transcription. *Int. J. Biochem. Cell Biol.* **40**, 1043–1054 (2008). doi:10.1016/j.biocel.2007.11.009 Medline

111. S. Dhe-Paganon, E. D. Werner, Y. I. Chi, S. E. Shoelson, Structure of the globular tail of nuclear lamin. *J. Biol. Chem.* **277**, 17381–17384 (2002). doi:10.1074/jbc.C200038200 Medline

112. V. Cenni, J. Bertacchini, F. Beretti, G. Lattanzi, A. Bavelloni, M. Riccio, M. Ruzzene, O. Marin, G. Arrigoni, V. Parnaik, M. Wehnert, N. M. Maraldi, A. de Pol, L. Cocco, S. Marmiroli, Lamin A Ser404 is a nuclear target of Akt phosphorylation in C2C12 cells. *J. Proteome Res.* **7**, 4727–4735 (2008). doi:10.1021/pr800262g Medline

113. P. Anversa, J. Kajstura, A. Leri, R. Bolli, Life and death of cardiac stem cells: a paradigm shift in cardiac biology. *Circulation* **113**, 1451–1463 (2006). doi:10.1161/CIRCULATIONAHA.105.595181 Medline

114. M. Biebl, C. M. Cooper, J. Winkler, H. G. Kuhn, Analysis of neurogenesis and programmed cell death reveals a self-renewing capacity in the adult rat brain. *Neurosci. Lett.* **291**, 17–20 (2000). doi:10.1016/S0304-3940(00)01368-9 Medline

115. W. W. Franke, M. Hergt, C. Grund, Rearrangement of the vimentin cytoskeleton during adipose conversion: formation of an intermediate filament cage around lipid globules. *Cell* **49**, 131–141 (1987). doi:10.1016/0092-8674(87)90763-X Medline

116. W. Yao, Z. Cheng, C. Busse, A. Pham, M. C. Nakamura, N. E. Lane, Glucocorticoid excess in mice results in early activation of osteoclastogenesis and adipogenesis and prolonged suppression of osteogenesis: a longitudinal study of gene expression in bone tissue from glucocorticoid-treated mice. *Arthritis Rheum.* **58**, 1674–1686 (2008). doi:10.1002/art.23454 Medline

117. K. R. Rosenbloom, C. A. Sloan, V. S. Malladi, T. R. Dreszer, K. Learned, V. M. Kirkup, M. C. Wong, M. Maddren, R. Fang, S. G. Heitner, B. T. Lee, G. P. Barber, R. A. Harte, M. Diekhans, J. C. Long, S. P. Wilder, A. S. Zweig, D. Karolchik, R. M. Kuhn, D. Haussler, W. J. Kent, ENCODE data in the UCSC Genome Browser: year 5 update. *Nucleic Acids Res.* **41**, (D1), D56–D63 (2013). doi:10.1093/nar/gks1172 Medline

118. ENCODE database (2013) http://genome.ucsc.edu/ENCODE/

119. B. Durand, M. Saunders, P. Leroy, M. Leid, P. Chambon, All-trans and 9-cis retinoic acid induction of CRABPII transcription is mediated by RAR-RXR heterodimers bound to DR1 and DR2 repeated motifs. *Cell* **71**, 73–85 (1992). doi:10.1016/0092-8674(92)90267-G Medline

120. R. Cortese, F. Eckhardt, M. Volleth, M. Wehnert, U. Koelsch, P. Wieacker, T. Brune, The retinol acid receptor B gene is hypermethylated in patients with familial partial lipodystrophy. *J. Mol. Endocrinol.* **38**, 663–671 (2007). doi:10.1677/JME-07-0035 Medline

121. L. V. Gonzalez Bosc, J. J. Layne, M. T. Nelson, D. C. Hill-Eubanks, Nuclear factor of activated T cells and serum response factor cooperatively regulate the activity of an alpha-actin intronic enhancer. *J. Biol. Chem.* **280**, 26113–26120 (2005). doi:10.1074/jbc.M411972200 Medline

122. L. L. Luchsinger, C. A. Patenaude, B. D. Smith, M. D. Layne, Myocardin-related transcription factor-A complexes activate type I collagen expression in lung fibroblasts. *J. Biol. Chem.* **286**, 44116–44125 (2011). doi:10.1074/jbc.M111.276931 Medline

123. S. J. Li, S. R. Chang, X. X. Qi, J. A. Richardson, E. N. Olson, Requirement of a myocardin-related transcription factor for development of mammary myoepithelial cells. *Mol. Cell. Biol.* **26**, 5797–5808 (2006). doi:10.1128/MCB.00211-06 Medline